1-1-2011

Lattice Kinetic Monte Carlo Simulations of Platelet Aggregation and Deposition

Matthew H. Flamm
University of Pennsylvania, matthewhflamm@gmail.com

Recommended Citation

Flamm, Matthew H., "Lattice Kinetic Monte Carlo Simulations of Platelet Aggregation and Deposition" (2011). *Publicly Accessible Penn Dissertations*. 509.
http://repository.upenn.edu/edissertations/509

Lattice Kinetic Monte Carlo Simulations of Platelet Aggregation and Deposition

Abstract

Platelet aggregation is an essential process in forming a stable clot to prevent blood loss. The response of platelets to a complex signal of pro-clotting agonists determines the stability and size of the resulting clot. An underdeveloped clot represents a bleeding risk, while an overdeveloped clot can cause vessel occlusion, which can lead to heart attack or stroke. A multiscale model was developed to study the integration of platelet signaling within the complex phenomena driven by flow. The model is built upon a lattice kinetic Monte Carlo algorithm (LKMC) to track platelet motion and binding. First, a new method for including flow-driven particle motion in LKMC was derived from a timescale analysis of particle motion. Simple methods for simulating flow-driven motion were found to exhibit concentration dependent velocities violating the assumptions in the model. The nature of the error was analyzed mathematically and resolved by considering the chain length distribution on the lattice. The accuracy of the method was found to scale linearly with the lattice spacing. Second, the LKMC method was extended to study particle aggregation in complex flows. The LKMC results for simple flows were compared directly to a continuum population balance equation (PBE) approach. A contact time model was introduced to capture nonideal collisions in the LKMC model and a connection to the continuum collision efficiency was derived. The particle size distribution for a baffled geometry with regions of standing vortices and squeezing flows was determined using the LKMC method for varying baffle heights. Finally, the LKMC method was incorporated within a multiscale model to simulate platelet aggregation including platelet signaling (neural network model), blood flow (lattice Boltzmann method), and the release of soluble platelet agonists (finite element method). The neural network model for platelet signaling was trained on patient-specific, experimental measurements of intracellular calcium enabling patient-specific predictions of platelet function in flow. The model accurately predicted the order of potency for three antiplatelet therapies, donor-specific aggregate size, and donor-specific response to antiplatelet therapy as compared to microfluidic experiments of platelet aggregation.

Degree Type
Dissertation

Degree Name
Doctor of Philosophy (PhD)

Graduate Group
Chemical and Biomolecular Engineering

First Advisor
Scott L. Diamond

Second Advisor
Talid Sinno

Subject Categories
Chemical Engineering

LATTICE KINETIC MONTE CARLO SIMULATIONS OF PLATELET AGGREGATION AND DEPOSITION

Matthew H. Flamm

A DISSERTATION

in

Chemical and Biomolecular Engineering

Presented to the Faculties of the University of Pennsylvania

in Partial Fulfillment of the Requirements for the Degree of

Doctor of Philosophy

2011

Supervisor of Dissertation	Co-Supervisor of Dissertation
Scott L. Diamond, Professor	Talid Sinno, Associate Professor
Chemical and Biomolecular Engineering	Chemical and Biomolecular Engineering

Graduate Group Chair

Raymond J. Gorte, Professor

Chemical and Biomolecular Engineering

Dissertation Committee

John C. Crocker, Associate Professor, Chemical and Biomolecular Engineering

Ravi Radhakrishnan, Associate Professor, Bioengineering

Lattice Kinetic Monte Carlo Simulations of Platelet Aggregation and Deposition

Acknowledgements

The work in this thesis would have been impossible without the help of many people. My advisors, Scott Diamond and Talid Sinno, first piqued my interest in working on platelet aggregation and provided me with support, scientific guidance, and direction to follow through on the original goal of the project. Although challenging at times, answering to two, sometimes diametrically opposed opinions strengthened my own intuition of the important questions.

I would like to thank John Crocker and Ravi Radhakrishnan who have been supportive yet critical of my work as part of my thesis committee. They are quick to ask the pertinent questions and approach me with ideas and encouragement.

A special thanks goes to Manash Chatterjee and Tom Colace who collaborated on the last part of this thesis. It was truly a group effort to design and implement such an ambitious project. My own part would not have been possible without their invaluable contributions and suggestions. Also, thanks to Sean Maloney for many experiments that never came to full fruition in the model.

To all those on the fifth floor Vagelos over the years including Fred, Raynaldo, Alex, Jeremy, Dan, Andrew, Roman, Yung-Chi, Ian, Jesse, Bob, and Ben for all the productive procrastinating over the years. I would like to particularly highlight my 54.9 % winning

percentage against Manash in lunch chess even if it wasn't statistically significant, $p = 0.056$.

Finally, I would like to thank my friends and family for their support throughout this process. My parents, Bruce and Kathy, have always supported me and have defined the ability to persevere when faced with a tough challenge. My wife, Ewelina, has been a constant source of inspiration, joy, and encouragement and cannot be thanked enough.

ABSTRACT

LATTICE KINETIC MONTE CARLO SIMULATIONS OF PLATELET AGGREGATION AND DEPOSITION

Matthew H. Flamm

Advisors: Scott L. Diamond and Talid Sinno

Platelet aggregation is an essential process in forming a stable clot to prevent blood loss. The response of platelets to a complex signal of pro-clotting agonists determines the stability and size of the resulting clot. An underdeveloped clot represents a bleeding risk, while an overdeveloped clot can cause vessel occlusion, which can lead to heart attack or stroke. A multiscale model was developed to study the integration of platelet signaling within the complex phenomena driven by flow. The model is built upon a lattice kinetic Monte Carlo algorithm (LKMC) to track platelet motion and binding. First, a new method for including flow-driven particle motion in LKMC was derived from a timescale analysis of particle motion. Simple methods for simulating flow-driven motion were found to exhibit concentration dependent velocities violating the assumptions in the model. The nature of the error was analyzed mathematically and resolved by considering the chain length distribution on the lattice. The accuracy of the method was found to scale linearly with the lattice spacing. Second, the LKMC method was extended to study particle aggregation in complex flows. The LKMC results for simple flows were compared directly to a continuum population balance equation (PBE) approach. A contact time model was introduced to capture nonideal collisions in the LKMC model and a connection to the continuum collision efficiency was derived. The particle size distribution for a baffled geometry with regions of standing vortices and squeezing flows was determined using the LKMC method for varying baffle heights. Finally, the LKMC method was incorporated within a multiscale model to simulate platelet aggregation including platelet signaling (neural network model), blood flow (lattice Boltzmann method), and the release of soluble platelet agonists (finite element method). The neural network model for platelet signaling was trained on patient-specific, experimental measurements of intracellular calcium enabling patient-specific predictions of platelet function in flow. The model accurately predicted the order of potency for three antiplatelet therapies, donor-specific aggregate size, and donor-specific response to antiplatelet therapy as compared to microfluidic experiments of platelet aggregation.

Contents

List of Tables

List of Figures

Chapter 1

Introduction

A major goal of systems biology is to integrate the complexity of signaling on the single cell level to predict the emergent phenomena on the tissue to organ scale. From an engineering perspective, the term *systems* represents the integration of the detailed knowledge of the individual components. In multicellular biology, this approach spans how cellular components combine to generate cellular phenotypes, how cells interact to yield tissue and organ function, and how tissues and organs communicate to create a unified organism. This analysis could even be extended to how organisms interact within and outside of their species. A famous example of a model on the societal scale is the Lotka-Volterra model (predator-prey equations). Even for single-celled organisms, the interaction of individual cells is important to the function, survival, and proliferation of the species and cannot be ignored. More specifically, systems biology models aim to gain insight into disease mechanism to predict avenues of pharmacological development or, even better, directly and quantitatively predict the efficacy of drug treatment. Computational studies may provide a complementary route for drug discovery and development, which is estimated to cost 800 million dollars per approved drug [1]. Computational models also enable the creation of patient-based therapies that tune, for example, drug dosage based on a patient's individual phenotype to improve drug efficacy and lower the incidence of undesirable side-effects.

Often multiple time and length scales are important for biological function including quantum effects [2], genetic encoding in DNA, protein interactions, organization of intracellular compartments, intracellular signaling, and tissue and organ function. Ideally, we can build models at the smallest length scales that reproduce the macroscopic behaviors, e.g. a full-scale molecular dynamics (MD) simulation of tissue function. State of the art MD simulations are only able to reach microsecond to millisecond timescales for a single protein in an explicit water solvent [3]. Therefore, higher level descriptions, e.g. ordinary differential equation (ODE) models of signaling, are required to reach the time and length scales of interest. Higher level models often require information from shorter time and length scales, so a multiscale approach becomes the most efficient method [4].

On the molecular scale, all atom simulations by MD are used to investigate the affinity of protein-ligand interactions [5] and the mechanism of protein folding [6]. Cellular signaling, which is the result of the molecular interactions, is usually described using a set of coupled ODEs. Each equation in the set of ODEs represents the rate of change in the concentration of one component in the cell, for example the divalent calcium ion, Ca^{2+}, and is derived from the mechanistic reactions in the cellular network. ODEs constructed using this approach conserve mass and predict the dynamic and steady state responses of the network. For systems biology, there are several standardized methods for describing models and performing numerical simulations including the Systems Biology Markup Language (SBML) [7] and CellML [8]. ODEs can be solved deterministically or stochastically depending on the scale of interest [9]. Another approach is to consider just the stoichiometric equations to predict the flux of mass within the cellular network [10]. Signaling models describe cellular response to extracellular stimuli [11] or the changes in intracellular metabolism when pathways are created or destroyed [12, 13].

Cellular function is not determined solely from internal mechanisms but also extracellular phenomena including biochemical signals. Physical interactions such as fluid shear [14, 15], extracellular matrix stiffness [16, 17], and strain [18] also affect cellular phenotype. Cellular signaling can be coupled to produce more robust signaling within each cell [19] and produce complex, emergent phenomena throughout the cellular network [20]. Biochemical signals are transported in tissue by diffusion and in the blood vessel by convection and can be modeled by solution of the convection-diffusion-reaction equation, a partial differential equation [21, 22].

Modeling biological systems becomes increasingly complicated as more mechanisms and scales of interactions are included, and computational power quickly limits the scale of problems that can be studied. Thus, one must limit models to the essential components that give rise to biological function. A detailed knowledge and intuition of the biology is crucial for choosing which mechanisms are important, and this knowledge comes largely from experiment. However, models are useful beyond prediction of experimental results; they provide a theoretical means to generate hypotheses to test experimentally. These experiments may lead to new insights by validating or contradicting the model. Validation confirms the mechanisms contained in the model, while contradiction leads to the search for new hypotheses. In either case, scientific knowledge is furthered.

The goal of this work is to build a multiscale model of platelet aggregation in flowing blood. Platelet aggregation is a key component of the body's hemostatic response to a blood vessel injury, while malfunction of this process can lead to vessel occlusion (overactivity) or excessive bleeding (underactivity). Platelets integrate several pro- and anti-clotting stimuli to form a stable clot to prevent blood loss from a vessel. The platelet agonists are transported by the fluid flow from the site of the injury, forming a boundary layer around the clot surface. The fluid itself is perturbed as the platelet aggregate grows into the lumen of the vessel. The model of platelet aggregation in this work includes the interactions between the fluid, the soluble agonists, platelet signaling, and platelet bonding.

In the process of building the multiscale model, new algorithms were developed and mathematically analyzed to enable platelet motion and aggregation in fluid flow. Specifically, a method based on lattice kinetic Monte Carlo (LKMC) was developed for following particle motion in a flowing fluid [23], enabling the transport of platelets to the injured surface (Chapter 3). In Chapter 4, the convective-LKMC algorithm is extended to particle aggregation in bulk flows including platelet aggregation [24]. In Chapter 5, the multiscale model, which is built upon the convective-LKMC algorithm, is developed to predict patient-specific platelet function under flow. Chapter 2 provides a general overview of the numerical methods that are used in the following chapters.

1.1 Models of convective particle motion

Flow driven particle motion is an important transport mechanism in many systems and often leads to particle aggregation or particle deposition. Biological examples include particle motion in the lung airways [25] and delivery of drugs in the blood stream [26]. Flow can also drive particle aggregation in the bulk fluid. Examples include aerosol aggregation in the atmosphere [27], aggregation of particles in ocean currents [28], cluster growth of paramagnetic particles in microchannels [29], and cell aggregation in blood flow

[30, 31, 32].

Particle motion in a flowing fluid depends on the hydrodynamic interactions between the particles. Strong coupling of particle motion can occur in systems such as sedimentation [33]. Models that incorporate hydrodynamic interactions include dissipative particle dynamics (DPD) [34], lattice Boltzmann (LB) [35], and direct solution of the coupled fluid momentum and particle motion equations such as the arbitrary Eulerian-Langrangian method [36]. DPD lumps packets of fluid into discrete particles that are subjected to random and viscous forces. DPD effectively solves the Navier-Stokes equation [37]. Similarly, LB considers packets of fluid that are streamed and collided on a lattice and effectively solves the Navier-Stokes equation [38]. The arbitrary Eulerian-Langrangian method can also be extended to include Brownian fluctuations [39]. These methods are well-suited for simulating particle motion in a fluid since they capture the fluid-particle coupling. However, the scale of systems that can be studied is computationally limited by the two-way coupling of the fluid momentum and particle motion.

Another class of methods only considers one-way coupling of fluid momentum and particle motion, i.e. particle motion is affected by the background flow field, but the fluid flow is unperturbed by particle motion. Examples include integrating the equations of motion for each particle [40], including a linear slip force in Brownian dynamics [41], and the cellular Potts model [42]. Although these methods do not include hydrodynamic interactions, they are computationally efficient compared to the fully coupled methods.

1.2 Models of particle aggregation

Much work has focused on mean-field approaches, i.e. the solution of the population balance (or Smoluchowski) equations [43]. Instead of following the trajectory of individual particles in the fluid, the classical population balance equation (PBE) approach considers the concentration of each particle size in the system, which yields continuum-scale differential equations. The specifics of particle motion and interactions are lumped into aggregation and fragmentation kernels that are usually derived from a combination of kinetic theory, hydrodynamics, and problem-specific chemical, biological, or other physical interactions. However, mean-field representations of particle aggregation driven by convection are limited to relatively simple cases. While the influences of hydrodynamic and particle-particle interactions have been studied extensively for constant shear rate [44, 45], PBE approaches do not address many common and realistic flows. In fact, a mean-field approach has been shown to break down even for pressure driven tube flow [46]. A direct simulation method is needed for modeling processes with complex flow fields.

Monte Carlo models have been used to study particle aggregation driven by Brownian motion [47] and have confirmed the Smoluchowski analysis at long times. Direct simulations of particle aggregation also present the possibility of explicitly considering size dependent particle diffusivities [48] and reaction control [49]. The emphasis of this thesis is to develop a Monte Carlo algorithm for studying particle aggregation driven by convection.

1.3 Platelet function in flow

1.3.1 Background

Platelet function is critical to maintaining hemostatis within the body. Overactivity of platelet function can lead to stroke or heart attack. Underactivity of the platelet response to a vessel injury increases bleeding risk. Platelets act as the central agent in a clotting episode, recognizing the exposed subendothelial matrix, releasing autocrine/paracrine platelet agonists, and serving as a scaffold for the production of the enzyme thrombin. Thombin itself is a potent platelet agonist that also creates a fibrous mesh within and around the growing clot. Platelets respond to a combination of stimuli including collagen, adenosine diphosphate (ADP), thromboxane (TXA_2), thrombin, epinephrine, and serotonin as well as endothelial cell derived inhibitors such as nitric oxide and prostacyclin.

Excessive clotting in response to cardiovascular disease, for example atherosclerotic plaque rupture, causes over 1 million heart attacks and strokes in the US each year. The risk of a vessel occlusion following plaque rupture can be linked to hyperactive platelet function [50]. Consequently, anti-platelet therapies, including aspirin to inhibit platelet COX-1 and clopidogrel to inhibit $P2Y_{12}$, are widely used by patients with cardiovascular risks. Although these therapies are successful at reducing the risk of clotting on the population level, a segment of the population has a so-called resistance to aspirin [51] and clopidogrel [52], which correlates with relatively worse clinical outcomes [53, 54].

Platelet function in vivo is dictated not only by receptor-ligand binding, calcium mobilization, and inside-out signaling but also the flow of blood over the injured surface. Blood flow dictates the rate of arrival of platelets and clotting factors while also acting to remove platelet agonists and coagulation enzymes. Flow can also directly affect platelet reactivity through an increased affinity to von Willebrand Factor at higher shear rates ($> 2000\,\mathrm{s}^{-1}$) [55] and direct activation of platelets at very high shear rates ($> 10\,000\,\mathrm{s}^{-1}$) [56].

The coagulation cascade is also an essential component of the body's response to a blood vessel injury. The coagulation cascade consists of a series of enzymatic steps that cleave a zymogen to an active enzyme. Tissue factor exposure at the site of injury starts the cascade to produce thrombin. Thrombin is a potent platelet activator and also cleaves fibrinogen into fibrin, which polymerizes into a fibrous network throughout the clot. Activated-platelet membrane serves as a scaffold for many of the steps in the coagulation cascade serving to speed up the reactions by orders of magnitude. Although thrombin generation is not considered in this work, avenues for including the coagulation cascade are discussed in Section 6.1.

1.3.2 Experimental models of thrombosis in flow

The in vivo validation of computational models is difficult. Many inputs for the model including vessel geometry, injury size and severity, and blood flow cannot be obtained from the in vivo experiment with precision. Although special cases such as large human carotid arteries can be directly imaged for vessel geometry and blood flow [57], large data sets are needed to train models and confirm results over a wide range of conditions. The simplest devices use a parallel plate flow chamber [58] or cone and plate viscometer to flow platelets over a surface patterned with collagen or other proteins of interest [59]. These experiments neglect the focal nature of a blood vessel injury in situations such as atherosclerotic plaque rupture.

Recently, microfluidic devices have been developed to create a focal injury [60, 61]. Strips of collagen are laid perpendicular to the microfluidic channels to create a well-defined collagen patch. Direct imaging of platelet deposition can be done in the microfluidic channels with fluorescence microscopy, and cluster sizes can be obtained using image analysis [62]. Microfluidic devices are also ideal for creating large data sets on platelet function in flow. Many channels can be imaged on a single plate [63], and many plates can be run from a single donor's blood draw allowing for the collection of a large range of conditions or a large number of repeats within a single experiment. Tissue factor can also be patterned on the surface to test coagulation function [64]

1.3.3 Computational models of thrombosis

Platelet signaling

Two types of models have been proposed for describing platelet signaling: a mechanistic and a data-driven approach. Purvis et al. developed a mechanistic, ordinary differential equation (ODE) model of platelet activation in response to ADP stimulation of $P2Y_1$. They found that both steady-state and dynamical information are important for describing platelet calcium signaling [65, 66]. Chatterjee et al. used high-throughput, combinatorial experiments to train a neural network for prediction of intracellular calcium in response to multiple agonists. [67].

Coagulation cascade

Hockin et al. developed a well-mixed ODE model of the coagulation cascade with a tissue factor stimulus capturing all phases of thrombin production [68]. Lo et al. simulated a version of the Hockin model using a stochastic method [69]. Kuharsky and Fogelson separated the reaction zone in a blood vessel from the blood flow to simulate the effect of flow on thrombin generation [70]. Chatterjee et al. extended the Hockin model to include platelet activation state and validated it against a combinatorial, high-throughput experiment [71].

Soluble agonist release

A prescribed platelet flux to an idealized geometry was used to enable solution of the concentration profiles of the soluble agonists ADP, TXA_2, and thrombin in the flowing fluid by Hubbell and McIntire [21]. Later, Folie and McIntire solved for the concentration profiles for several clot geometries using a similar method [72]. Sorensen et al. coupled ADP, TXA_2, and thrombin production to platelet deposition in a continuum model at the surface [73, 74].

Hydrodynamic effects and red blood cell motion

Mody and King solved for the hydrodynamic interactions of flowing platelets near a wall [75, 76]. Pivkin et al. used dissipative particle dynamics that captured hydrodynamic effects to simulate platelets adhering to a wall with a simple activation distance function [77]. Although hydrodynamics are important for the collisions between particles and between a particle and the wall, the trajectories in blood flow are largely determined by the motion of red blood cells in the fluid. Whole blood is comprised of approximately 40 % RBCs by volume. Several models of RBC motion have been proposed to describe viscosity relationships [78] and platelet margination [79, 80]. These calculations are computationally costly and would be difficult to directly integrate into a model for platelet deposition that occurs over minutes.

Hemodynamics

Blood flow is non-Newtonian at low shear rates. In general, the viscosity of blood is well characterized by the Casson equation, which relates the shear stress to the shear rate. For a Newtonian fluid, $\tau = \mu\gamma$, where τ is the shear stress, μ is the viscosity, and γ is the shear rate. The Casson equation is

$$\sqrt{\tau} = \sqrt{\mu\gamma} + \sqrt{\tau_y}, \tag{1.1}$$

where τ_y is the yield stress. Above shear rates of approximately $100\,\mathrm{s}^{-1}$, blood is Newtonian with an effectively viscosity of approximately 0.003 Pa s (3 times the viscosity of water, 0.001 Pa s) [81]. For large arteries, a Newtonian approximation is accurate [82] although for vessels with low shear, e.g. venous flow, the non-Newtonian behavior of blood may become more important. Three dimensional models of blood flow are beginning to predict large scale flow measurements in vessel geometries obtained from patient imaging [83, 57].

Fully coupled models

More recent models have coupled platelet deposition to the flowing fluid, ADP release, and thrombin production. Leiderman and Fogelson used a continuum method based on Kuharsky and Fogelson that explicitly solves for the spatial and temporal variations [84]. Xu et al. used a cellular Potts model for platelet motion coupled to flow and a model for thrombin generation based on Kuharsky and Fogelson [85]. Both models include coupling between platelet deposition, blood flow, ADP release, and thrombin generation. The major difference between the Leiderman and Fogelson model (hereafter referred to as the LF model) and the Xu et al. model (hereafter referred to as the Xu model) is the description of the platelet. The LF model treats platelets as a continuum species and introduces additional equations to give platelets a tunable cohesion based on activation state and a physical size. The Xu model treats platelets as discrete entities that can bind together and move in the fluid using a cellular Potts model, where platelets occupy several lattice nodes on a grid.

The cellular Potts model describes the dynamics of a system on a lattice, where each node is numbered according to which cell is occupying that lattice space. All the lattice sites occupied by cell i are numbered i. All fluid nodes have a special number, e.g. 0, to distinguish from nodes occupied by cells. The main input into a cellular Potts model is the Hamiltonian for any given system state. The Hamiltonian for a system of cells in a fluid generally consists of a volume and an area conserving term for each cell to establish particle size. Cellular bonding, cell motion, and other cellular processes also contribute to the Hamiltonian. Once the Hamiltonian is specified, identity flips are attempted where the identity of a single node is switched to the identity of another node. The usual Metropolis Monte Carlo criterion is used to accept or reject the attempted move according to the change in the Hamiltonian. Therefore, the key in any cellular Potts model is to define the appropriate Hamiltonian and system temperature.

One advantage of the discrete method in the Xu model is that platelet size is very straightforward to implement—the size of each platelet is determined by how many lattice nodes it occupies. Events in the model that depend on platelet activation state, e.g. ADP release and cellular bonding, can be directly obtained from the local activation states of platelets on the lattice. Furthermore, morphology and porosity are direct outputs of the simulations. Discrete models are also amenable to introducing simulation variables that have distributions, e.g. platelet size or platelet activation thresholds. However, the cellular Potts model does not inherently have a system clock. This prevents direct comparison to dynamic quantities such as velocity and reaction rate. Directed motion may be implemented by introducing a force in the direction of flow. However, the resulting velocity of the particle will generally depend on the choice of the volume and area constraints as a move in the direction of flow generally changes both the volume and area of a particle. A fitting parameter is needed to obtain the correct time scaling (the relationship between a Monte Carlo step and time). Although the energies of cellular bonding in the Hamiltonian may be compared to the energy of making receptor-ligand bonds between cells, platelet deposition may not be close to equilibrium, and the kinetics of cellular bonding may be important.

The continuum method in the LF model directly captures the motion of platelets and the kinetics of cellular bonding. In a continuum framework without discrete particles, each component of the system is treated as a chemical species being transported through the fluid. To give platelets some physical size, the LF model introduces a new species, η, that is constantly emitted from all bound platelets and diffuses away with some decay rate. The choices of diffusivity, release rate, and decay rate of η determine the effective size of the platelet. All quantities that depend on the location of bound platelets, e.g. binding rate of unbound platelets to bound platelets, are determined through the local concentration of η. Platelets in this model are fuzzy in the sense that the edges are not well defined and platelets can overlap. Although this approach gives some coarse sense of size to a platelet, morphology and fluid pore size cannot be captured directly captured in this model.

Chapter 2

Numerical methods

This chapter includes a general description of the numerical methods used in this work. More specific implementations are discussed within the following chapters. The kinetic Monte Carlo (KMC) method is introduced in Section 2.1 and used in Chapters 3–5. The finite element method is introduced in Section 2.2 and used in Chapter 5 . Finally, the lattice Boltzmann method is presented in Section 2.3 and used in Chapter 5. Neural networks are not presented in this section since the implementation was problem specific. A description of the neural network model is given in Section 5.3.3.

2.1 Kinetic Monte Carlo methods

The main input into the KMC simulation is a rate database for all possible events in the system. The rates may be precomputed before the simulation [86] or computed on-the-fly [87] according to the current system state. For a single event i out of N possible events, let the rate of that event be Γ_i, where the rate depends on the current system state. Given the set of rates $(\Gamma_1, \Gamma_2 \ldots \Gamma_i \ldots \Gamma_{N-1}, \Gamma_N)$ at a particular system state, the KMC algorithm chooses which event occurs next and at what time. In general, the state of the system changes after every event requiring the rate database to be updated accordingly. Thus, a KMC simulation has three major components:

- Choosing the next event that occurs
- Calculating the time at which that event fires
- Updating the rate database following event execution

At a system time t, the joint probability distribution of the next event being of type μ and occurring at time $t + \tau$ is $P(\mu, \tau)$. $P(\mu, \tau)$ is constructed to satisfy the assumption that all events are independent Poisson processes, and the KMC algorithm samples trajectories from this distribution. The probability that an event i will occur in the time interval $(t, t + \delta t)$ for a Poisson process is $P_i = \Gamma_i \delta t$. The probability that none of the N events occurs in the time interval $(t, t + \tau)$ is exponentially distributed, $P_0(\tau) = \exp(-\Gamma_{\text{tot}} \tau)$, where $\Gamma_{\text{tot}} = \sum_{i=1}^{N} \Gamma_i$. The probability that the *next* event is of type μ and occurs in the time interval $(t + \tau, t + \tau + \delta t)$ is

$$P(\mu, \tau)\, \delta t = P_0(\tau)\, \Gamma_\mu \delta t = \exp(-\Gamma_{\text{tot}} \tau)\, \Gamma_\mu \delta t. \tag{2.1}$$

In general, the waiting time at which the next event occurs according to the probability distribution in Equation 2.1 with N independent Poisson processes is

$$\tau = -\frac{\ln(u)}{\Gamma_{\text{tot}}}, \tag{2.2}$$

where u is a uniform random number in the interval $(0, 1]$, regardless of which event is executed at that step. The average time step chosen is

$$\langle \tau \rangle = \frac{1}{\Gamma_{\text{tot}}} \tag{2.3}$$

An event i is chosen to be the next event with probability

$$P_i = \frac{\Gamma_i}{\Gamma_{\text{tot}}}. \tag{2.4}$$

Several algorithms have been proposed to generate events and event times that obey the probability distribution in Equation 2.1 [88, 89, 90, 91, 92]. Here, discussion is limited to three common algorithms and the algorithmic complexity of each. Gillespie proposed two methods: the direct method and the first reaction method [88]. Later, Gibson and Bruck proposed the next reaction method [89].

2.1.1 Direct method

The direct method involves choosing a time for an event to occur in the system and then choosing an event that fires at that time. The time step of the next event is calculated as in Equation 2.2, and a specific event μ is chosen with the probability given in Equation

2.4 with the following procedure

$$\sum_{i=1}^{\mu-1} \Gamma_i < u * \Gamma_{\text{tot}} \leq \sum_{i=1}^{\mu} \Gamma_i, \tag{2.5}$$

where u is a uniform random number in the interval $[0, 1]$. The time step calculation requires a sum over N rates, and event selection requires a sum over $O(N)$ rates. From these summations, the direct method is also known as the n-fold way [93]. Speedup is obtained if the partial sums are kept from the time update for use in the event selection, although the overall complexity of the algorithm is still $O(N)$.

2.1.2 First reaction method

In the first reaction method, a 'test' waiting time is generated for each event before each step as

$$\tau_i = -\frac{\ln(u)}{\Gamma_i}, \tag{2.6}$$

which requires N random numbers per step. The event with the smallest waiting time is executed, and the system time is updated with the waiting time of that event. Since the events are independent Poisson processes with no memory, new event waiting times can be generated for the next step in the algorithm using Equation 2.6 according to the new rate database. The overall complexity of the first reaction method is $O(N)$ and requires $O(N)$ random numbers per step.

2.1.3 Next reaction method

Gibson and Bruck modified the first reaction method by retaining the old waiting times of events not affected by the previous step, taking advantage of the independent Poisson process assumption [89]. Here, the absolute time at which an event occurs is tracked instead of the waiting time, i.e.

$$t_i = t + \tau_i, \tag{2.7}$$

where t_i is the putative time at which event i will occur and will be referred to as the event time. The event times are always sorted from lowest to highest, which allows for an $O(1)$ choice of event. The largest portion of computational overhead is now sorting the event times after each step. Instead of sorting the list from scratch after each step, the event times that change during a step, the ones whose rate is affected by the executed step, are removed from the list, again leaving a sorted list. New event times are generated for events whose rates change, and the corresponding event times are added back to the queue.

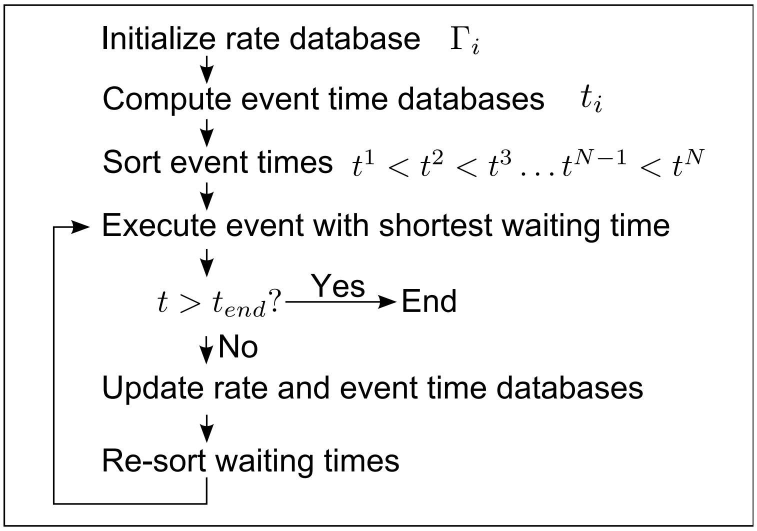

Figure 2.1: Schematic of next reaction method

In this work, a skip list [94] is used to sort the event times, which has $O(\ln(N))$ insertion, deletion, and query complexity. To further speed up this method, the event time can be updated without the use of another random number as follows

$$t_i = t + \left(\frac{\Gamma_{\text{old}}}{\Gamma_{\text{new}}}\right)(t_i^\star - t)\,, \tag{2.8}$$

where $t_i^\star$ is the old event time. Equation 2.8 is not valid for events that do not have event times, i.e. the events had zero rate at the previous step, and in this case, Equations 2.6 and 2.7 can be used to generate an event time. A summary of the next reaction method is shown in Figure 2.1.

2.1.4 Comparison of KMC methods

A summary of the algorithm complexity is given in Table 2.1. Sorting time represents the complexity in sorting a list with $O\left(1\right)$ events updated at each step. Although the direct method and the first reaction method do not require the extra sorting step, they have overall $O(N)$ complexity. The next reaction method has overall $O(\ln(N))$ complexity. For problems with long-range interactions that require $O(N)$ rate updates at each step, the direct method or first reaction method may prove to be more efficient. The systems considered in this work consist of many particles having relatively short-range potentials, so the next reaction method is the most efficient algorithm.

	Event selection	Time update	Sorting
Direct Method	$O(N)$	$O(N)$	—
First Reaction Method	$O(N)$	$O(1)$	—
Next Reaction Method	$O(1)$	$O(1)$	$O(\ln(N))$

Table 2.1: Comparison of KMC event and time selection methods. Sorting step complexity assumes $O(1)$ rate updates.

Beyond optimization of the basic, exact KMC algorithm, many acceleration techniques have been developed to achieve larger length and time scales. The τ-leaping method fires multiple events in a single time step [95], and more accurate methods based on τ-leaping have been devised [96]. In lattice KMC, the single lattice site occupancy can be coarse-grained into coarse cell occupancies [97]. Although these techniques are not utilized in this work, in principle, some of the acceleration ideas could be adapted to this specific implementation.

2.2 Finite element methods

The following information is adapted from Comini, Del Giudice, and Nonino [98], and Reddy and Gartling [99]. The concentration field, C, of a soluble species within a moving fluid is given by the convection-diffusion-reaction equation, which is a type of partial differential equation (PDE),

$$\frac{\partial C}{\partial t} + \mathbf{v} \cdot \nabla C = D \nabla^2 C + R, \tag{2.9}$$

where $\mathbf{v}$ is the velocity field of the fluid, D is the diffusion coefficient of the solute, and R is a general bulk source/sink term resulting from generation or consumption of solute.

The finite element method solves for a solution of a PDE by approximating the dependent variables with piecewise nodal approximations. The spatial domain is discretized into well-defined and non-overlapping shapes, which are known as elements. Within each element, e, local approximations are defined as linear combinations of interpolation functions, ϕ_i, and nodal values, C_i that are approximations to the dependent variable C at nodes. There are m elements and n total nodes. Over the entire domain, the approximate representation of C is

$$C \approx \hat{C} = \sum_{i=1}^{n} \phi_i C_i. \tag{2.10}$$

The interpolation functions are constructed such that they are nonzero only in the elements adjacent to the corresponding nodal value, i.e.

$$\phi_i = \begin{cases} \phi_i^e & \text{if node } i \text{ is adjacent to element } e \\ 0 & \text{if node } i \text{ is not adjacent to element } e. \end{cases} . \tag{2.11}$$

The interpolation functions themselves are piecewise across neighboring elements, so the superscript refers to the form of the interpolation function within the element e. Linear basis functions within rectangular elements are used in this work.

To solve the original PDE, a weighted-residual approach is employed where the equations are solved such that the integral residual error over the domain Ω is zero, i.e.

$$\begin{aligned}\int_\Omega W_i \frac{\partial C}{\partial t}\,\mathrm{d}\Omega + \int_\Omega W_i \mathbf{v}\cdot\nabla C\,\mathrm{d}\Omega \\ = \int_\Omega W_i D\nabla^2 C\,\mathrm{d}\Omega + \int_\Omega W_i R\,\mathrm{d}\Omega\end{aligned} \tag{2.12}$$

with $i = 1, n$, which results in n equations for the n nodal values. In the Galerkin method, the weighting functions, W_i, are chosen as the piecewise interpolation functions, ϕ_i. It is convenient to reduce the order of the PDE by using Green's theorem, which gives

$$\begin{aligned}\int_\Omega \phi_i \frac{\partial C}{\partial t}\,\mathrm{d}\Omega + \int_\Omega \phi_i \mathbf{v}\cdot\nabla C\,\mathrm{d}\Omega \\ = -\int_\Omega D\nabla\phi_i\cdot\nabla C\,\mathrm{d}\Omega - \int_S \phi_i q\,\mathrm{d}S + \int_\Omega \phi_i R\,\mathrm{d}\Omega,\end{aligned} \tag{2.13}$$

where S is the boundary and q is the flux of mass normal to the boundary ($-D\nabla C\cdot\mathbf{n} = q$). C is approximated by Equation 2.10, which results in

$$\begin{aligned}\int_\Omega \phi_i \sum_{j=1}^{n} \frac{\partial \phi_j C_j}{\partial t}\,\mathrm{d}\Omega + \int_\Omega \phi_i \mathbf{v}\cdot\nabla\sum_{j=1}^{n}\phi_j C_j\,\mathrm{d}\Omega \\ = -\int_\Omega D\nabla\phi_i\cdot\nabla\sum_{j=1}^{n}\phi_j C_j\,\mathrm{d}\Omega - \int_S \phi_i q\,\mathrm{d}S + \int_\Omega \phi_i R\,\mathrm{d}\Omega.\end{aligned} \tag{2.14}$$

The interpolation functions ϕ_i are spatially varying and time invariant while the nodal values C_i are specified at nodes and vary with time. Thus, Eq. 2.14 can be written

$$\begin{aligned}\sum_{j=1}^{n}\frac{\partial C_j}{\partial t}\int_\Omega \phi_i\phi_j\,\mathrm{d}\Omega + \sum_{j=1}^{n} C_j\int_\Omega \phi_i\mathbf{v}\cdot\nabla\phi_j\,\mathrm{d}\Omega \\ = -\sum_{j=1}^{n} C_j\int_\Omega D\nabla\phi_i\cdot\nabla\phi_j\,\mathrm{d}\Omega - \int_S \phi_i q\,\mathrm{d}S + \int_\Omega \phi_i R\,\mathrm{d}\Omega,\end{aligned} \tag{2.15}$$

where i is represents the ith weighting (interpolation) function. To simplify Eq. 2.15, we define the following vector and matrix quantities

$$\mathbf{C} = (C_1, C_2 \ldots C_i \ldots C_{N-1}, C_N) \tag{2.16}$$

$$\dot{\mathbf{C}} = \left(\frac{\partial C_1}{\partial t}, \frac{\partial C_2}{\partial t} \cdots \frac{\partial C_i}{\partial t} \cdots \frac{\partial C_{N-1}}{\partial t}, \frac{\partial C_N}{\partial t}\right) \tag{2.17}$$

$$M_{ij} = \int_\Omega \phi_i\phi_j\,\mathrm{d}\Omega = \sum_{e=1}^{m}\int_{\Omega^e}\phi_i^e\phi_j^e\,\mathrm{d}\Omega^e \tag{2.18}$$

$$K_{ij} = \int_\Omega D\nabla\phi_i\cdot\nabla\phi_j\,\mathrm{d}\Omega = \sum_{e=1}^{m}\int_{\Omega^e} D\nabla\phi_i^e\cdot\nabla\phi_j^e\,\mathrm{d}\Omega^e \tag{2.19}$$

$$G_{ij} = \int_\Omega \phi_i\mathbf{v}\cdot\nabla\phi_j\,\mathrm{d}\Omega = \sum_{e=1}^{m}\int_{\Omega^e}\phi_i^e\mathbf{v}\cdot\nabla\phi_j^e\,\mathrm{d}\Omega^e \tag{2.20}$$

$$p_i = \int_S \phi_i q\,\mathrm{d}S = -\sum_{e=1}^{m}\int_{S^e}\phi_i^e q\,\mathrm{d}S^e \tag{2.21}$$

$$r_i = \int_\Omega \phi_i R\,\mathrm{d}\Omega = \sum_{e=1}^{m}\int_{\Omega^e}\phi_i^e R\,\mathrm{d}\Omega^e \tag{2.22}$$

The elemental nature of the basis functions have been applied in Equations 2.16–2.22, and Ω^e is the domain of element e. The integrals are numerically evaluated by Gaussian quadrature. In matrix form the final system of equations is

$$\mathbf{M}\dot{\mathbf{C}} + \mathbf{A}\mathbf{C} = \mathbf{b}, \tag{2.23}$$

where the following definitions are introduced

$$\mathbf{A} = \mathbf{K} + \mathbf{G} \tag{2.24}$$

$$\mathbf{b} = \mathbf{p} + \mathbf{r}. \tag{2.25}$$

The generalized Crank-Nicolson method uses a finite difference approximation for the time derivative,

$$\frac{\partial \mathbf{C}}{\partial t} \approx \frac{\mathbf{C}^{n+1} - \mathbf{C}^{n}}{\Delta t}, \tag{2.26}$$

using the known solution at time t^n and the unknown solution at time t^{n+1}, $\Delta t = t^{n+1} - t^n$. The contributions to $\mathbf{A}$ and $\mathbf{b}$ from time points $n+1$ and n are weighted with a parameter α as

$$\bar{\mathbf{A}} = (1-\alpha)\,\mathbf{A}^n + \alpha \mathbf{A}^{n+1} \tag{2.27}$$

$$\bar{\mathbf{b}} = (1-\alpha)\,\mathbf{b}^n + \alpha \mathbf{b}^{n+1}. \tag{2.28}$$

Eq. 2.23 becomes

$$\mathbf{H} C^{n+1} = \mathbf{f}, \tag{2.29}$$

where $\mathbf{H}$ and $\mathbf{f}$ are defined as

$$\mathbf{H} = \frac{1}{\Delta t}\mathbf{M} + \alpha \mathbf{A}^{n+1} \tag{2.30}$$

$$\mathbf{f} = \left(\frac{1}{\Delta t}\mathbf{M} - (1-\alpha)\,\mathbf{A}^n\right)\mathbf{C}^n + (1-\alpha)\,\mathbf{b}^n + \alpha \mathbf{b}^{n+1} \tag{2.31}$$

The choice of α leads to a variety of methods. For $\alpha = 0$, the explicit Euler method is obtained. For $\alpha = 1$, the implicit Euler method is obtained. The explicit method is conditionally stable but very efficient to implement. The implicit method is unconditionally stable but in general requires an iterative solution method. The Crank-Nicolson method is obtained for a choice of $\alpha = \frac{1}{2}$, which is second order accurate over a time interval compared to the first order Euler methods. The Crank-Nicolson method is unconditionally stable although it does exhibit oscillations for large time steps.

2.3 Lattice Boltzmann

The Navier-Stokes (NS) and the continuity equations describe the flow of fluid, measured by the velocity $\mathbf{v}$, in response to a pressure gradient, ∇P. The incompressible NS equation is given by

$$\rho\left(\frac{\partial \mathbf{v}}{\partial t}+\mathbf{v}\cdot\nabla\mathbf{v}\right)=-\nabla P+\mu\nabla^2\mathbf{v}, \tag{2.32}$$

where ρ is the density and μ is the dynamic viscosity of the fluid. The incompressible continuity equation is given by

$$\nabla\cdot\mathbf{v}=0. \tag{2.33}$$

Lattice Boltzmann (LB) does not solve for Equations 2.32 and 2.33 directly. In LB, packets of fluid stream from lattice nodes to neighboring nodes, where they undergo a collision event. The process of streaming and collision results in the solution of the NS and continuity equations [100].

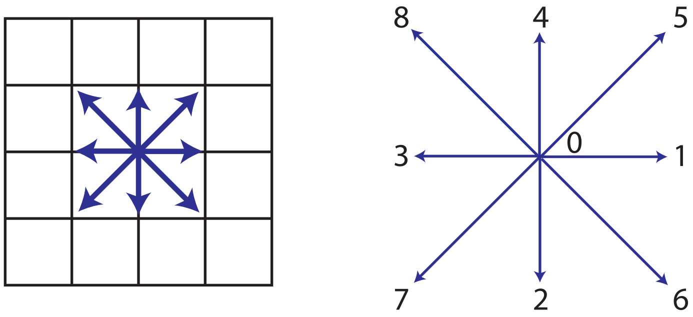

Figure 2.2: Lattice velocities. On left, the velocities on the lattice Boltzmann grid. On right, the numbering of the velocities including the stationary velocity.

A square lattice with spacing δ_x is used where each node is connected to its eight nearest neighbors (Figure 2.2). Fluid particles reside at the nodes and are streamed to nearest neighbor nodes in one time step, δ_t. There are three speeds of particles in this system: particles at rest ($i = 0$), particles moving in the lattice directions ($i = 1 \ldots 4$), and particles moving along the diagonals ($i = 5 \ldots 8$). It is common in the lattice Boltzmann literature to rescale variables so that the particles moving in the lattice directions ($i = 1 \ldots 4$) have unit velocity magnitudes defined as

$$\begin{aligned}
&\mathbf{e}_0 = \begin{bmatrix} 0 \\ 0 \end{bmatrix} \\
&\mathbf{e}_1 = \begin{bmatrix} 1 \\ 0 \end{bmatrix} \mathbf{e}_2 = \begin{bmatrix} 0 \\ -1 \end{bmatrix} \mathbf{e}_3 = \begin{bmatrix} -1 \\ 0 \end{bmatrix} \mathbf{e}_4 = \begin{bmatrix} 0 \\ 1 \end{bmatrix} \\
&\mathbf{e}_5 = \begin{bmatrix} 1 \\ 1 \end{bmatrix} \mathbf{e}_6 = \begin{bmatrix} 1 \\ -1 \end{bmatrix} \mathbf{e}_7 = \begin{bmatrix} -1 \\ -1 \end{bmatrix} \mathbf{e}_8 = \begin{bmatrix} -1 \\ 1 \end{bmatrix}.
\end{aligned} \tag{2.34}$$

The time step and the lattice spacing have been rescaled to lattice units ($\delta_x = 1$ lattice space, $\delta_t = 1$ time step). The velocities have units of lattice space/time step. This particular lattice is known as D2Q9 (2 dimensions, 9 velocities) [101].

The probability of finding a particle at a node with position $\mathbf{x}$ at time t with velocity $\mathbf{e}_i$ is given by $f_i(\mathbf{x}, t)$. The density at a particular node is the zeroth moment of the particle distribution function,

$$\rho = \sum_i f_i, \tag{2.35}$$

and the velocity at a particular node is the first moment of the particle distribution function,

$$\rho \mathbf{v} = \sum_i \mathbf{e}_i f_i, \tag{2.36}$$

where the summation limits are assumed to be from i=0. . . 8. The second moment,

$$\mathbf{\Pi} = \sum_i \mathbf{e}_i \mathbf{e}_i f_i, \tag{2.37}$$

is related to the stress tensor, but is generally not needed to run a lattice Boltzmann simulation.

The evolution of the distribution function at each node satisfies the lattice Boltzmann equation,

$$f_i\left(\mathbf{x} + \mathbf{e}_i, t+1\right) - f_i\left(\mathbf{x}, t\right) = \Omega_i, \tag{2.38}$$

where Ω_i is the operator representing the rate of change of the particle distribution function due to particle collisions. The simplest approach is to assume that the particle distribution function relaxes to some equilibrium state $f_i^{\mathrm{eq}}\left(\rho, \mathbf{v}\right)$ with a single relaxation time τ. This is known as the Bhatnagar, Gross and Krook (BGK) operator and the resulting equation,

$$f_i\left(\mathbf{x} + \mathbf{e}_i, t+1\right) - f_i\left(\mathbf{x}, t\right) = -\frac{1}{\tau}\big(f_i\left(\mathbf{x}, t\right) - f_i^{\mathrm{eq}}\left(\mathbf{x}, t\right)\big), \tag{2.39}$$

is known as the lattice Boltzmann BGK (LBGK) equation. The equilibrium distribution is

$$f_i^{\mathrm{eq}} = t_i \rho \left(1 + 3\left(\mathbf{e}_i \cdot \mathbf{v}\right) + \frac{9}{2}\left(\mathbf{e}_i \cdot \mathbf{v}\right)^2 - \frac{3}{2}\left|\mathbf{v}\right|^2\right), \tag{2.40}$$

where the weights t_i are

$$\begin{aligned} t_0 &= \frac{4}{9} \\ t_1 = t_2 = t_3 = t_4 &= \frac{1}{9} \\ t_5 = t_6 = t_7 = t_8 &= \frac{1}{36}. \end{aligned} \tag{2.41}$$

τ is related to the kinematic lattice viscosity as

$$\nu = \frac{2\tau - 1}{6} \tag{2.42}$$

The LBGK algorithm (Equation 2.39) is conceptually executed by two steps: propagation and collision. During propagation, particle distributions are translated to nearest neighbor nodes according to the equation

$$f_i^* \left(\mathbf{x} + \mathbf{e}_i, t\right) = f_i \left(\mathbf{x}, t\right), \tag{2.43}$$

where the superscript $*$ denotes the post-propagation/pre-collision state. Before collision, the values of ρ and $\mathbf{v}$ are calculated according to Equations 2.35 and 2.36, and then the equilibrium distribution is calculated according to Equation 2.40. During collision, the BGK operator is performed as

$$f_i \left(\mathbf{x}, t+1\right) = \left(1 - \frac{1}{\tau}\right) f_i^* \left(\mathbf{x}, t\right) + \frac{1}{\tau} f_i^{\mathrm{eq}*} \left(\mathbf{x}, t\right), \tag{2.44}$$

where $f_i^{\mathrm{eq}*}$ is determined during the post-propagation/pre-collision state.

2.3.1 Boundary conditions

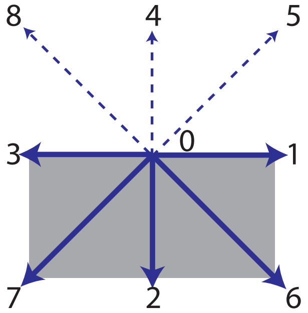

Figure 2.3: Bottom boundary node. Solid lines are known distributions after propagation. Dotted lines are unknown distributions after propagation.

The boundary conditions can be handled in multiple ways. The Zou-He boundary condition [102] is applicable for specifying velocity boundary conditions (including no slip) and pressure (density) boundary conditions and is also one of the easiest to implement. Consider the bottom boundary node shown in Figure 2.3. After propagation, $f_0, f_1, f_2, f_3, f_6, f_7$ are specified. Suppose that we want to set the boundary condition

$$\mathbf{v} = \begin{pmatrix} v_x \\ v_y \end{pmatrix} \tag{2.45}$$

on this node. Note that no-slip $\left(v_x = v_y = 0\right)$ is included in this boundary condition. The zeroth (Equation 2.35) and first moment (Equation 2.36) of the particle distributions can be used to determine the missing distributions, f_4, f_5, f_8, with the form

$$f_4 + f_5 + f_8 = \rho - (f_0 + f_1 + f_2 + f_3 + f_6 + f_7) \tag{2.46}$$

$$f_5 - f_8 = \rho v_x - (f_1 + f_6 - f_3 - f_7) \tag{2.47}$$

$$f_4 + f_5 + f_8 = \rho v_y + (f_2 + f_6 + f_7)\,. \tag{2.48}$$

There are four unknowns (ρ,f_4,f_5, and f_8) and three equations, but Equations 2.46 and 2.48 give

$$\rho = \frac{1}{1 - v_y}\left[f_0 + f_1 + f_3 + 2\left(f_2 + f_6 + f_7\right)\right], \tag{2.49}$$

which leaves three unknowns and two equations. To obtain one more constraint, the *non-equilibrium part* of the particle distribution in the normal direction is *bounced-back* and can be written (in this case)

$$f_2 - f_2^{eq} = f_4 - f_4^{eq}. \tag{2.50}$$

This is the Zou-He boundary condition. Since Equation 2.49 and the boundary condition in Equation 2.45 fully determine the equilibrium state for f_2 and f_4, all unknown distributions can be found, thus

$$\begin{aligned}
f_4 &= f_2 + \frac{2}{3}v_y \\
f_5 &= f_7 - \frac{1}{2}\left(f_1 - f_3\right) + \frac{1}{2}\rho v_x + \frac{1}{6}\rho v_y \\
f_8 &= f_6 + \frac{1}{2}\left(f_1 - f_3\right) - \frac{1}{2}\rho v_x + \frac{1}{6}\rho v_y.
\end{aligned} \tag{2.51}$$

The collision step is still performed on the boundary node after the unknown distribution functions are set.

The pressure (density) boundary condition is formulated in the same manner. The boundary condition is

$$\begin{aligned}
\rho &= \rho^* \\
v_x &= 0,
\end{aligned} \tag{2.52}$$

where ρ^* is the desired pressure to be set on the boundary. With the same node in Figure 2.3, the incoming velocity normal to the boundary is determined similar to Equation 2.49,

$$v_y = 1 - \frac{\left[f_0 + f_1 + f_3 + 2\left(f_2 + f_6 + f_7\right)\right]}{\rho^*}. \tag{2.53}$$

Again, the bounceback rule is used, and the remaining distributions are set as

$$\begin{aligned} f_4 &= f_2 + \frac{2}{3}\rho^* v_y \\ f_5 &= f_7 - \frac{1}{2}\left(f_1 - f_3\right) + \frac{1}{6}\rho^* v_y \\ f_8 &= f_6 + \frac{1}{2}\left(f_1 - f_3\right) + \frac{1}{6}\rho^* v_y. \end{aligned} \tag{2.54}$$

Chapter 3

Including convection in lattice kinetic Monte Carlo

The kinetic Monte Carlo (KMC) method has been applied to an extensive range of nonequilibrium, stochastic systems in materials science, biology, and physics. Applications include dynamics of λ-phage infection of E. coli [103], multicomponent aggregation and fragmentation [104, 105], defect diffusion in metals and semiconductors [106], and crystal growth [107]. A common theme in these applications is that the system dynamics are driven by stochastic events, e.g. molecular reaction or diffusion, that occur on time scales much larger than the microscopic dynamics of individual atoms or molecules.

Although the KMC approach is well established for purely diffusive or reactive systems [88, 108], it has generally not been applicable to systems in which drift (from convective fluid flow or another globally applied field) drives particle motion. Even for a single particle, Gauthier and Slater have shown that to include drift in a Monte Carlo simulation, the rates of motion (or probabilities) must be correctly specified [109, 110]. The inclusion of convective-diffusive transport in KMC offers the possibility of studying the stochastic behavior of particle aggregation in complex transport conditions.

Methods such as lattice Boltzmann [35] and dissipative particle dynamics [34] are well-suited for simulating particle motion in a fluid since they capture fluid-particle coupling. Another example is the direct numerical simulation of the momentum equations in which multiple rigid or elastically deformable particles are present [36]. However, the scale of systems that can be studied is computationally limited by the calculation of fluid-particle coupling.

A lattice kinetic Monte Carlo (LKMC) algorithm is developed to follow the trajectories of tracer particles in the fluid where the fluid flow is not affected by the motion of the particles. Rates of motion by diffusion and convection are derived using a timescale analysis, but an unphysical evolution is observed using a simple convection bias. The bias is corrected by analyzing particle blocking on the lattice. This algorithm enables the simulation of convection-diffusion of particles by the LKMC method.

3.1 Taylor-Aris dispersion

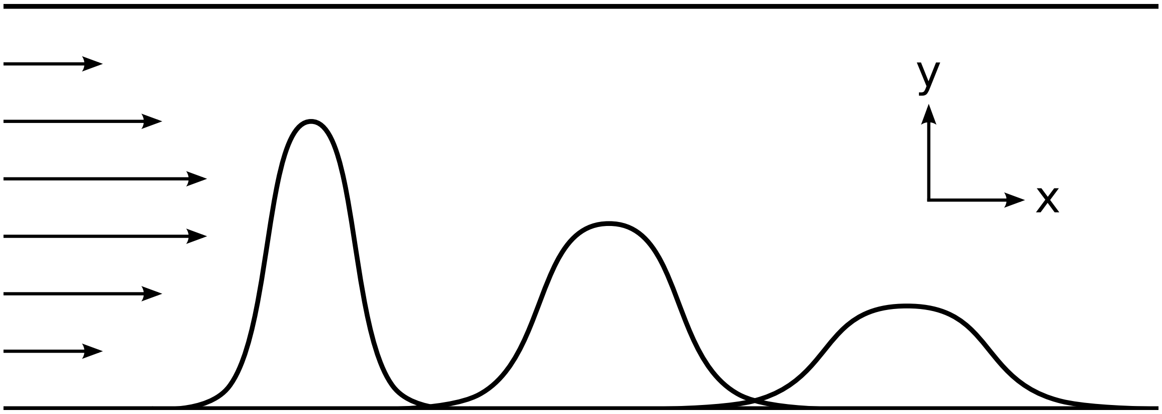

Figure 3.1: Taylor Aris dispersion. Solute within a parallel plate channel with parabolic flow profile spreads diffusively as it is convected downstream.

The well-known phenomenon of Taylor-Aris dispersion (Figure 3.1) is used to develop the convective KMC algorithm. In this classical problem, a collection of particles or a solute is entrained in a fluid within a tube or channel. In this work, we focus on flow between two parallel plates in two dimensions (2D). When applying a pressure gradient along the x direction, the fully-developed, steady-state velocity profile is given by

$$v_x\left(y\right) = \frac{3}{2} v_{\text{avg}} \left(1 - \frac{y^2}{H^2}\right), \tag{3.1}$$

where v_{avg} is the average fluid velocity and $2H$ is the parallel plate separation distance. The dimensionless parameter that governs the relative importance of diffusive and convective transport is the Peclet number (Pe), which is defined as

$$Pe = \frac{v_{\text{avg}} H}{D}. \tag{3.2}$$

A pulse of solute is introduced in the channel with the particle distribution given by a one-dimensional Gaussian distribution in the x-direction, with a height of $C_{\max}$ and standard deviation of σ. The continuum equation describing the evolution of the particle distribution is generally given by

$$\frac{\partial C}{\partial t} + \nabla \cdot \left(\mathbf{v} C\right) = D \nabla^2 C \tag{3.3}$$

where $C\left(x, y\right)$ is the solute concentration and D is the solute diffusivity. The Aris analysis shows that at long times the particle distribution is diffusive when averaged across the channel width, i.e. $\bar{C} = \frac{1}{H}\int_0^H C dy$, and the x-coordinate is rescaled as $\bar{x} = x - v_{\text{avg}} t$

[111]. The effective transport equation is given by

$$\frac{\partial \bar{C}}{\partial t} = K \frac{\partial^2 \bar{C}}{\partial \bar{x}^2}, \tag{3.4}$$

where the dispersion coefficient for this geometry is given by

$$K = D\left(1 + \frac{2}{105} Pe^2\right). \tag{3.5}$$

3.2 LKMC simulations of diffusion

As stated in Section 2.1, the main input into a KMC simulation is the rate database for all possible events. Considering a particle moving by Brownian motion, there are an infinite number of step directions and step lengths that need to be considered. To constrain the number of possible events, the space is discretized with lattice spacings h_x and h_y in the x- and y-directions respectively, so that a particle only moves to nearest neighbor lattice sites in one step. In this section, each particle occupies a single lattice site. Particles are considered to be tracers in the fluid and therefore follow the fluid velocity. The particles only interact through site exclusion which prevents particles from occupying the same lattice site.

When there is no pressure gradient applied to the channel $\left(v_{\mathrm{avg}} = 0\right)$, particles move solely by diffusive motion. The timescale for a diffusive hop from one lattice site to an adjacent lattice site is

$$\tau_d = \frac{h^2}{D}. \tag{3.6}$$

The rate for an event is inversely proportional to the timescale, so the rate of a diffusive move on the lattice is

$$\Gamma_d = \frac{D}{h^2}. \tag{3.7}$$

The cross-sectional averages of the solute pulse diffusion profile from LKMC ($v_{\text{avg}} = 0$, $D = 1$) are compared to the solution of Equation 3.3 by COMSOL, a commercial finite element software, with $v_{\text{avg}} = 0$ at several times. Excellent agreement is observed at timescales that are long with respect to individual hops on the lattice. This result is not surprising since kinetic Monte Carlo has been used to study diffusive processes in many systems [112, 113, 114].

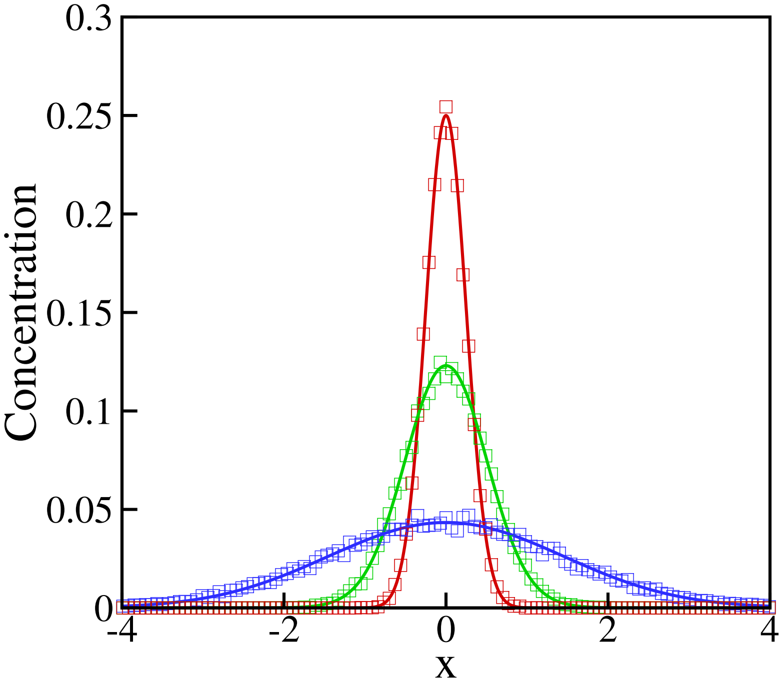

Figure 3.2: Diffusion in KMC. Evolution of a 1D Gaussian pulse at $t = 0$ (red) with maximum concentration of $C_{\max} = 0.25$ and standard deviation of $\sigma = 0.25$ with zero convection ($v_{\text{avg}} = 0$, $D = 1$) computed with COMSOL [Equation 3.3] (solid lines) and LKMC (symbols). Red, $t = 0$; green, $t = 1$; blue, $t = 10$.

3.3 Simplest Biasing Algorithm

Consider a single particle at a position (x, y) with a fluid velocity $\mathbf{v}(x, y) = \begin{pmatrix} v_x \\ v_y \end{pmatrix}$. For the Taylor-Aris dispersion problem, the velocity field is unidirectional in the x-direction ($v_y = 0$), which is aligned with the lattice. The timescale for this particle to move one lattice space in the direction of flow solely due to convection is given by

$$\tau_c = \frac{h}{v_x}. \tag{3.8}$$

The rate of a convective move on the lattice is given by

$$\Gamma_c = \frac{v_x}{h}. \tag{3.9}$$

The simplest method to combine diffusive and convective motion is to add the rate of convection to the rate of diffusion in the direction of flow, i.e

$$\Gamma_{x+} = \Gamma_c + \Gamma_d, \tag{3.10}$$

where the direction of flow is in the positive x-direction. In all other directions, the rates of motion are unchanged. This method will be termed the simplest biasing algorithm, or SBA-LKMC.

The evolution of the Gaussian solute pulse with the SBA-LKMC method for $Pe = 100$ ($v_{\text{avg}} = 1000$, $H = 0.1$, $D = 1$) and a uniform LKMC grid ($h_x = 0.01$, $h_y = 0.002$) is shown in Figure 3.3 (symbols). The particle evolution is clearly nondiffusive, whereby the trailing edge of the particle distribution becomes steeper while the leading edge

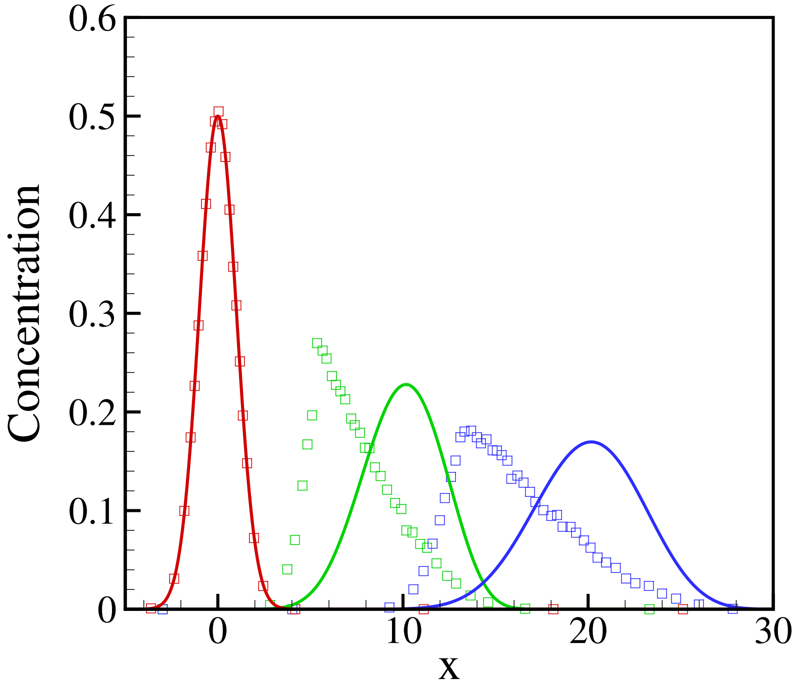

Figure 3.3: Particle blocking on the lattice causes a concentration dependent drift. Evolution of a Gaussian pulse at t=0 (red) with maximum concentration of $C_{\max} = 0.5$ and standard deviation of $\sigma = 1$ ($v_{\text{avg}} = 1000$, $D = 1$, $H = 0.1$) computed with COMSOL [Equation 3.3] (solid lines) and SBA-LKMC method (symbols) ($h_x = 0.01$, $h_y = 0.002$). Red, $t = 0$; green, $t = 0.01$; blue, $t = 0.02$.

exhibits a long tail. Also shown in Figure 3.3 is the numerical solution of Equation 3.3 with the velocity profile in Equation 3.1, computed using COMSOL (solid line), which demonstrates the expected diffusive spreading of the solute pulse. In the context of Taylor-Aris dispersion, the Aris analysis gives a constant value of $K = 191$ at long times, which is in excellent agreement with the numerically extracted value of $K = 191$ at $t = 0.02$ from the COMSOL solution of Equation 3.3. Not only is the SBA-LKMC prediction of the pulse shape evolution incorrect, but it also underpredicts the average velocity of the solute particles. With more dilute solute pulses, these discrepancies become smaller, but the SBA-LKMC method does not provide satisfactory results until the solute particle concentration approaches zero everywhere.

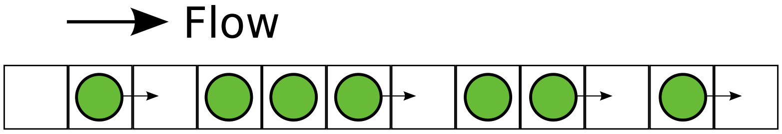

Figure 3.4: Particle blocking on the lattice. Particles that are blocked on the lattice in the direction of flow have zero convective rate.

The errors in the SBA-LKMC results arise from the combination of single-particle moves inherent in the LKMC method and particle-particle blocking due to the site exclusion interaction. Note that site exclusion is required if morphological information (e.g. aggregate shape) is to be preserved. Particles that have nearest neighbors in the direction of the flow are blocked and are subject to zero convective and diffusive hopping rates (Figure 3.4). As a result of convective blocking, the sum of the rates in the system at any given time is underestimated. Moreover, the fact that the probability of such an occurrence increases with the solute concentration leads to a concentration-dependent rate of convection.

3.4 Analysis of the Simplest Biasing Algorithm

Consider an isolated, diffusionless ($D = 0$) particle on a 1D lattice at position x. The particle is entrained in a fluid with unidirectional fluid velocity v. The convective rate in the positive direction is $\Gamma_c = \frac{v}{h}$. The effective velocity of a particle, v_{particle}, is the distance the particle travels by the time required to move that distance, or

$$v_{\text{particle}} = \frac{P_{\text{particle}} h}{t}, \tag{3.11}$$

where $t = \frac{1}{\Gamma_{\text{tot}}}$ is the average time step for a single move and P_{particle} is the probability that a particle is chosen to move. In this case, there is only one event possible at any time so $P_{\text{particle}} = 1$ and the total rate of the system is $\Gamma_{\text{tot}} = \frac{v}{h}$. The effective particle velocity is then

$$v_{\text{particle}} = \Gamma_c h = v. \tag{3.12}$$

Therefore, this algorithm leads to the correct effective velocity for a single particle on the lattice.

Now consider a collection of N diffusionless particles in a 1D system with the particle number density given by $C(x)$. Due to site exclusion, a particle at position x_k is unable to move in the direction of flow if another particle exists at position $x_k + h$. This occurs with probability $C(x_k + h)$. When a particle is unable to move, its convective rate is 0. The average convective rate of a particle is therefore the probability the particle is *available* to move, $1 - C\left(x_k + h\right)$, times the convective rate, Γ_c, which gives

$$\Gamma_c^{\text{eff}}\left(x_k\right) = \big(1 - C\left(x_k + h\right)\big)\Gamma_c. \tag{3.13}$$

The probability that a particle k at position x_k is chosen to move during a step out of the N particles is

$$P_{\text{particle}}\left(x_k\right) = \frac{\Gamma_c^{\text{eff}}\left(x_k\right)}{\Gamma_{\text{tot}}}, \tag{3.14}$$

where $\Gamma_{\text{tot}} = \sum_{i=1}^{N} \Gamma_c^{\text{eff}}\left(x_k\right)$. Using Eq. 3.11, the effective velocity of a particle is

$$v_{\text{particle}}\left(x_k\right) = \big(1 - C\left(x_k + h\right)\big)v. \tag{3.15}$$

The effective velocity of a particle on the lattice is now a function of the local concentration of particles. If the change in particle concentration is small over one lattice spacing, $C\left(x_k\right) \approx C\left(x_k + h\right)$, then Eq. 3.15 becomes

$$v_{\text{particle}}\left(x_k\right) = \big(1 - C\left(x_k\right)\big)v. \tag{3.16}$$

Using Equation 3.16 in the one-dimensional form of Equation 3.3, the corresponding continuum equation that represents particle transport in the SBA-LKMC method is

$$\frac{\partial C}{\partial t} + \nabla \cdot \big(v(1 - C)C\big) = D\nabla^2 C \tag{3.17}$$

The comparison between the COMSOL solution of Equation 3.17 and the SBA-LKMC method is shown in Figure 3.5. The nonlinear spreading of the concentration profile is captured with the concentration-dependent drift with the form, $(1 - C)v$. From this analysis, it is clear that particle blocking on the lattice causes a concentration-dependent decrease in the rate of convective motion.

It is interesting to note that the one-dimensional version of Equation 3.17 is directly related to the Burgers equation [115],

$$\frac{\partial C}{\partial t} + vC\frac{\partial C}{\partial x} = D\frac{\partial^2 C}{\partial x^2}. \tag{3.18}$$

The Burgers equation was originally proposed to study fluid turbulence and has been applied to traffic flow [116], surface growth [117], sedimentation [33], and other traveling shock phenomena. Although the Burgers equation describes particle motion in some

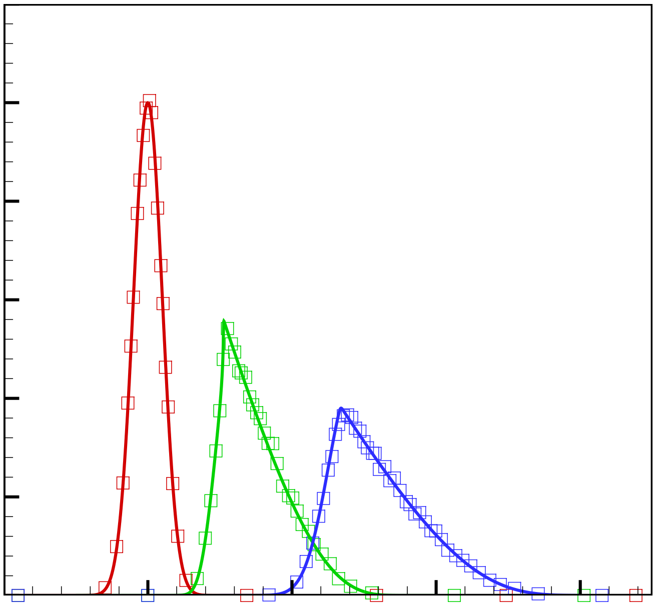

Figure 3.5: Continuum transport equation with concentration-dependent drift matches SBA-LKMC results. Evolution of a Gaussian pulse at t=0 (red) with maximum concentration of $C_{\max} = 0.5$ and standard deviation of $\sigma = 1$ ($v_{\text{avg}} = 1000$, $D = 1$, $H = 0.1$) computed with COMSOL [Equation 3.3 with concentration dependent velocity from Equation 3.16] (solid lines) and SBA-LKMC method (symbols) ($h_x = 0.01$, $h_y = 0.002$). Red, $t = 0$; green, $t = 0.01$; blue, $t = 0.02$.

specific situations such as sedimentation, the nonlinearity is caused by particle-fluid-particle coupling, which is not considered in this system.

3.5 Pass Forward Algorithm

From Eq. 3.13, it can be seen that particle blocking causes a reduction in the effective convective rate in the system. To correct for the reduction, the lost convective rate in the system must be reintroduced in a physically consistent manner. The goal is to restore the effective rate to be the same as an isolated particle on the lattice, $\Gamma_c^{\text{eff}} = \frac{v}{h}$. Since a particle cannot move when blocked, the particle's convective rate can only be augmented when it is not blocked. The magnitude of this effect must depend on the local concentration of particles to eliminate the concentration dependent drift.

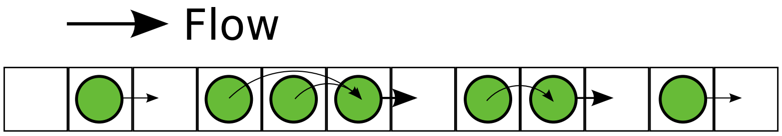

Figure 3.6: Pass forward algorithm. Particles that are blocked on the lattice in the direction of flow have zero convective rate; the convective rates of these particles are passed forward (in the direction of flow) to the first non-blocked particle.

A pass forward algorithm (PFA-LKMC), which satisfies the conditions above, is used to correct for particle blocking. Particles that are blocked from moving in the direction of flow pass convective rate forward in a linearly connected chain to the first particle that is available to move. For a linearly connected chain of s particles on the lattice, $s-1$ particles are blocked from moving in the direction of flow, and one particle, which receives the convective rates of all s particles, is available to move. An example is shown in Figure 3.6, where only 4 particles are available to move but the particles in front of chains of particles have a higher convective rate. Isolated particles on the lattice are unaffected by this algorithm. For the case where a uniform, uniaxial flow of magnitude v is applied, the rate of convective motion of a particle at the front of a chain of s particles is

$$\Gamma_c\left(s\right) = s\frac{v}{h}. \tag{3.19}$$

The PFA-LKMC method preserves the total convective rate of the system, i.e.

$$\Gamma_{\text{tot}} = \Gamma'_{\text{tot}} + \Gamma_{\text{blocked}}, \tag{3.20}$$

where Γ'_{tot} is the total rate of the system in the SBA-LKMC method (from particles that are not blocked) and Γ_{blocked} is the total rate of all blocked particles. The theoretical basis for the PFA-LKMC method is presented in section 3.6

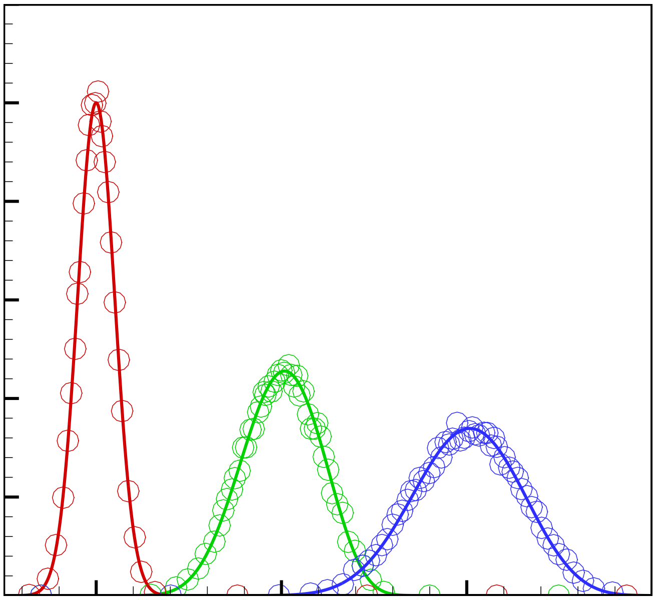

Figure 3.7: Pass forward algorithm corrects for particle blocking on the lattice. Evolution of a Gaussian pulse at t=0 (red) with maximum concentration of $C_{\max} = 0.5$ and standard deviation of $\sigma = 1$ ($v_{\text{avg}} = 1000$, $D = 1$, $H = 0.1$) computed with COMSOL [Equation 3.3] (solid lines) and PFA-LKMC method (symbols) ($h_x = 0.01$, $h_y = 0.002$). Red, $t = 0$; green, $t = 0.01$; blue, $t = 0.02$.

The temporal evolution of the Gaussian solute pulse with the PFA-LKMC method for $Pe = 100$ ($v_{\text{avg}} = 1000$, $H = 0.1$, $D = 1$) and a uniform LKMC grid ($h_x = 0.01$, $h_y = 0.002$) is shown in Figure 3.7 (symbols). The cross-sectional averaged concentration profile matches the expected evolution with the correct average velocity and diffusive spreading. The measured dispersion coefficient averaged between $t = 0.019$ and $t = 0.02$

is $K = 202.0 \pm 2.8$, which is in agreement with the analytic and computed continuum values. There is some additional dispersion that results from discretization ($\approx 6\,\%$), and this effect is clearly shown in Figure 3.8. As the lattice spacing that is aligned with the flow is decreased, the measured dispersion from the PFA-LKMC method approaches the analytic result from Equation 3.5. Further, the PFA-LKMC method is accurate for a wide range of Peclet numbers with the most relative error in the region of $1 \leq Pe \leq 100$. The origin of the additional dispersion is analyzed in detail in Section 3.8.

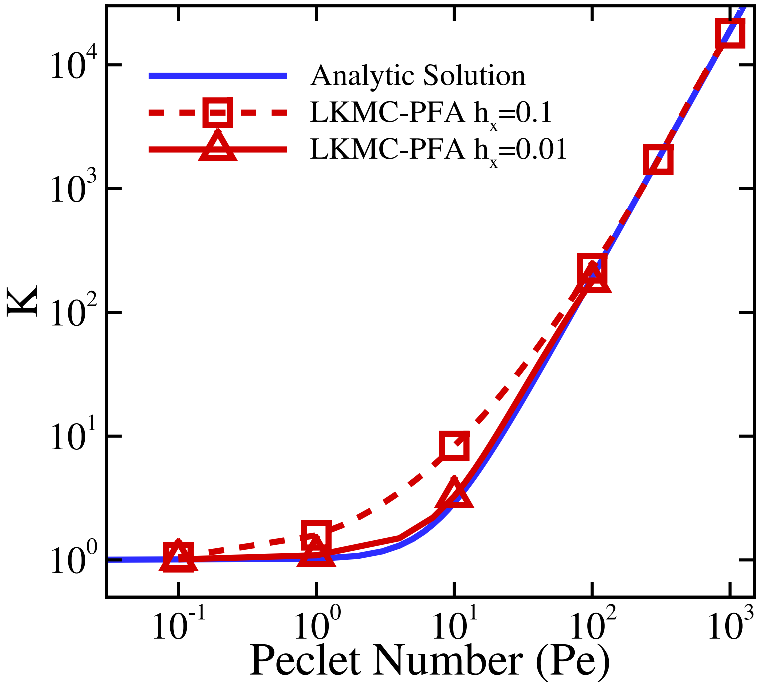

Figure 3.8: The PFA-LKMC method is valid over a wide range of Peclet number. The dispersion coefficient, K, was averaged between $t = 0.019$ and $t = 0.02$ for a range of Peclet numbers by varying v_{avg}, while holding $H = 0.1$ and $D = 1$ constant. The lattice spacing in the direction of flow was varied over an order of magnitude, $0.01 \leq h_x \leq 0.1$, while the lattice spacing against the direction of flow was held constant ($h_y = 0.002$)

3.6 Analysis of Pass Forward Algorithm

The rate of convective motion for a particle k now depends on whether that particle is part of chain of particles and where in the chain that particle is located. The probability of a particle being a part of a chain of particles can be estimated using one dimensional percolation theory [118]. Again considering a 1D system with velocity in the positive direction with magnitude v, the probability of the particle k being the rightmost particle in a linearly connected chain of s particles is the probability that there is an unoccupied lattice space in the forward direction, $1 - C(x_k)$, times the probability of $s - 1$ lattice sites being occupied by particles in the reverse direction, $C(x_k)^{s-1}$, times the probability of an unoccupied lattice space at the reverse end of the chain, $1 - C(x_k)$, which gives

$$\eta(x_k, s) = \left(1 - C(x_k)\right)^2 C(x_k)^{s-1}. \tag{3.21}$$

$\eta(x_k, s)$ is the probability that a particle k is at the front of a chain of s particles. In Equation 3.21, it is assumed that the average chain length is much smaller than the distance over which the concentration changes, i.e. $C(x_k) \approx C(x_k - sh)$. Using the rate of a particle at the front of a linearly connected chain of s particles from Equation 3.19, the average rate of a particle k is given by the weighted average,

$$\Gamma_c^{\text{eff}}(x_k) = \sum_{s=1}^{\infty} \Gamma_c(s) \eta(x_k, s) = \frac{v}{h}\left(1 - C(x_k)\right)^2 \sum_{s=1}^{\infty} sC(x_k)^{s-1}. \tag{3.22}$$

With the identity

$$\sum_{i=1}^{\infty} i a^{i-1} = \frac{1}{(1-a)^2} \tag{3.23}$$

for $a < 1$ [118], Equation 3.22 can be simplified as

$$\Gamma_c^{\text{eff}}\left(x_k\right) = \frac{v}{h}. \tag{3.24}$$

Thus, the average velocity of a particle in the PFA-LKMC method is (from Equation 3.11) v at any position and particle concentration.

The blocked convective rates are reintroduced to the system ina way that conserves the local particle velocity. A particle on the lattice is blocked more often in areas of higher concentration but has a higher rate of convection when it is available to move. On average, each particle obtains the correct average convective rate and average particle velocity over many moves. This mathematical analysis will generally break down when the chain lengths in the system have the same length scale as the distance over which the concentration changes. These length scales can become comparable when there are sharp gradients in the concentration profile or when the chain lengths are long ($C \to 1$).

3.7 Extension to two-dimensional flows

The PFA-LKMC method can be extended readily to situations with multidimensional flows that are not necessarily aligned with the grid by simply decomposing the local velocity vector into its components along the LKMC grid (Figure 3.9). Generally, a velocity vector is given by $\mathbf{v} = v_x\mathbf{e}_x + v_y\mathbf{e}_y$, where $\mathbf{e}_i$ is the unit vector in the ith direction. The convective rates for the ith lattice direction is given by

$$\Gamma_c\left(i\right) = \frac{\max\left(0, \mathbf{v}\cdot\mathbf{e}_i\right)}{h}, \tag{3.25}$$

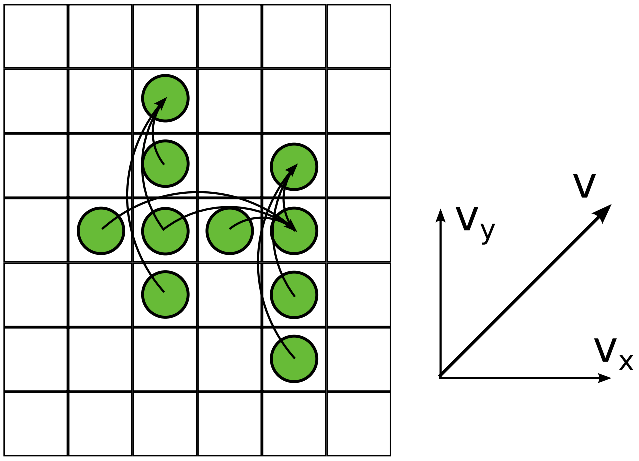

Figure 3.9: Extension of the PFA-LKMC method to two (or three) dimensional flows. The generalized velocity for each particle is decomposed into velocity vectors along the lattice directions. Then each velocity component is passed independently in the direction of flow.

where convective rates are only non-zero in the direction of flow. In order to apply the PFA-LKMC method to this two-dimensional velocity field, the convective rates for each component are passed in the direction of flow independently in both the x- and y-directions. For three-dimensional flows, the velocity is decomposed into the three lattice components, and the convective rates are passed independently.

The two-dimensional version of the PFA-LKMC algorithm is tested using a parallel plate, 3:1 expansion-flow geometry, which leads to the formation of vortices in the region immediately following the expansion (Figure 3.10). The evolution of an initial Gaussian solute pulse (in the flow-direction) as a function of time, computed by numerical solution of Equation 3.3 and with the PFA-LKMC method, is shown in Figure 3.10. The velocity field was determined by COMSOL in both cases. The vortices serve as reservoirs for the solute and continue to leach solute out of the cell long after the primary pulse has been convected out of the domain. Figure 3.11 shows the fraction of solute remaining in the expansion-flow domain. There is a lag time before the primary pulse exits the domain, then a rapid loss of solute, and finally the solute leaches out of the vortices at long times. For comparison, the remaining solute fraction as a function of time for a straight channel is also shown in Figure 3.11. The straight channel geometry still exhibits a lag time, but does not have the long-time leaching of solute. Virtually all solute has been removed by a dimensionless time of 3. Excellent agreement is demonstrated in Figure 3.11 between the continuum and the PFA-LKMC predictions for the fraction of solute remaining for both expansion-flow and straight channel geometries.

3.8 Analysis of discretization error

While the PFA-LKMC algorithm effectively corrects for particle blocking on the lattice, the algorithm does exhibit some discretization error (Figure 3.8). We analyze this effect using a one-dimensional system of N diffusionless ($D = 0$) particles subject to a uniform velocity of magnitude, v, on a uniform lattice (lattice spacing h). The particles move according to PFA-LKMC method. The particle positions at time t are given by a distribution $X(t) = \big(x_1(t) \ldots x_N(t)\big)$, which evolves from an initial Gaussian distribution, X_0 with mean of μ_0 and variance of σ_0^2. The distribution of particle positions given that exactly m LKMC steps have occurred has mean $\mu_{x|m} + \mu_0$ and variance $\sigma_{x|m}^2 + \sigma_o^2$, where $\mu_{x|m}$ and $\sigma_{x|m}^2$ are the change in the mean and variance, respectively. Given that a time t has passed, the step number m is itself a random Poisson variable with equal mean and variance,

$$\mu_m = \sigma_m^2 = t\Gamma_{\text{tot}}, \tag{3.26}$$

where $\Gamma_{\text{tot}} = N\frac{v}{h}$ for the diffusionless system under consideration. For $t\Gamma_{\text{tot}} > 10$, m can be approximated by a normal distribution with the same mean and variance.

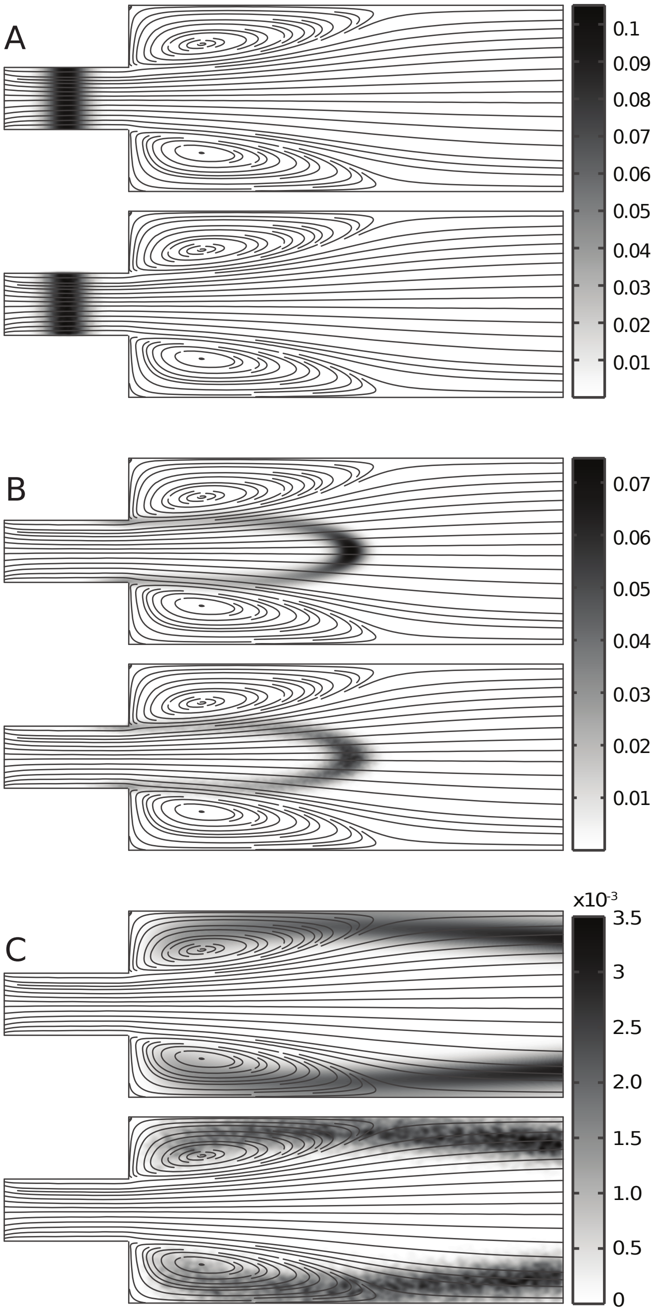

Figure 3.10: Solute pulse evolution as a function of time in a two-dimensional laminar expansion flow. The narrow channel width is 1 dimensionless unit and the wide channel width is 3 units. The lengths of the narrow and wide channels are 2 and 7 units, respectively. Each panel shows a comparison between numerical solution of Equation 3.3 (upper) and LKMC-PFA (lower) with the color bar representing particle number density for both the numerical solution and LKMC-PFA. The velocity profile, denoted by streamlines, was computed with COMSOL with $Pe = 413$ ($v_{\text{avg}} = 41.3$, $D = 0.1$) and $Re = 41.3$ ($\rho = 1$, $\mu = 1$) at the inlet. (a) $t = 0$, (b) $t = 0.1$, and (c) $t = 0.6$.

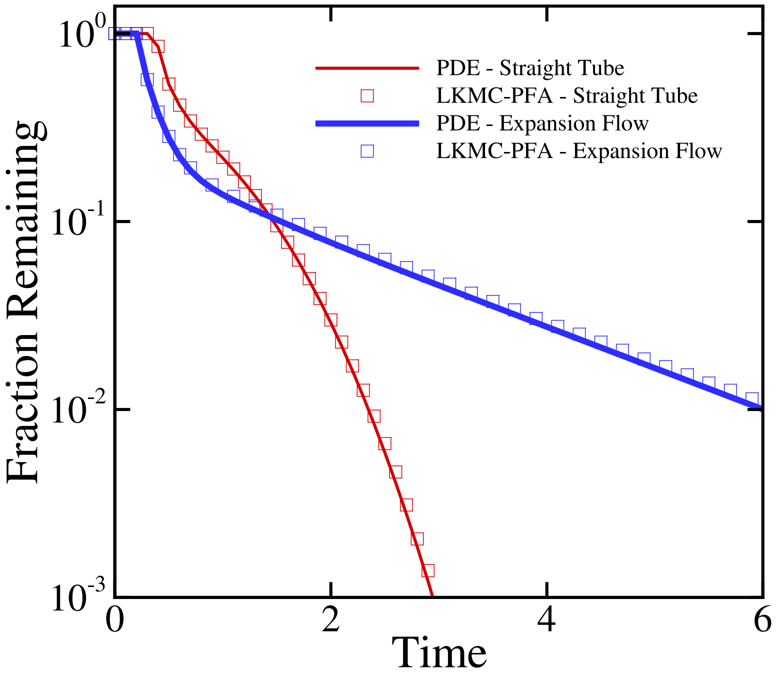

Figure 3.11: The PFA-LKMC method accurately captures two dimensional drift. Fraction of solute remaining within the simulation domain from Figure 3.10 as a function of dimensionless time. Lines: numerical solution of Equation 3.3 with COMSOL. Blue line and symbols represent expansion flow geometry and red line and symbols represent straight-channel geometry. Symbols: PFA-LKMC. The straight-channel geometry has the same overall length of the expansion-flow domain shown in Figure 3.10 and the same height as the wide region. The flow parameters are the same at the outlet of each channel.

The true mean of $X(t)$, $\mu_x + \mu_0$, is given by the conditional expectation formula [119]

$$\mu_x = \langle \mu_{x|m} \rangle = \mu_m \Delta x = t\Gamma_{\text{tot}} \frac{h}{N} = vt, \tag{3.27}$$

where $\Delta x = \frac{h}{N}$ is the change in $\mu_{x|m}$ due to one move and the expressions for μ_m and Γ_{tot} were applied. μ_x is the mean of the particle positions at some time t, which accounts for the distribution in m. The true variance of $X(t)$, $\sigma_x^2 + \sigma_0^2$, is derived in a similar fashion based on the conditional variance formula [119]

$$\sigma_x^2 = \left\langle \sigma_{x|m}^2 \right\rangle + \mathrm{var}\left(\mu_{x|m}\right). \tag{3.28}$$

The first term is the change in the variance if exactly m steps have occurred, and the second term is the variance caused by the distribution of m steps at time t (see Figure 3.12). The variance of $\mu_{x|m}$ is

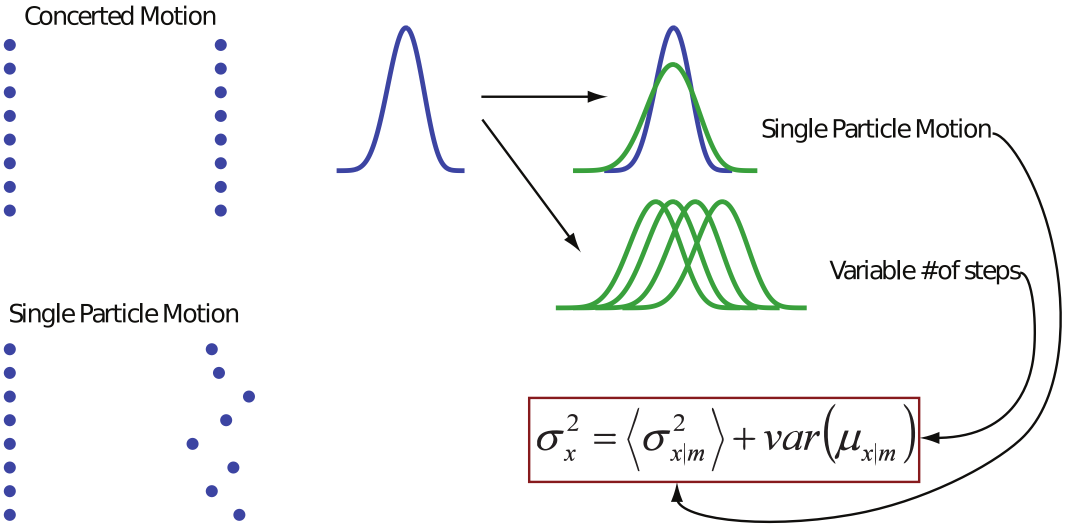

Figure 3.12: Origins of discretization error in the PFA-LKMC method. The distribution widens due to single particle motion on the lattice. This can be measured by the average change in the variance after exactly m steps, $\left\langle \sigma_{x|m}^2 \right\rangle$. The distribution also widens due to the distribution in m, which can be measured by the variance in the mean position, $\mathrm{var}\left(\mu_{x|m}\right)$.

$$\mathrm{var}\left(\mu_{x|m}\right) = \sigma_m^2 \left(\Delta x\right)^2 = tvh/N \tag{3.29}$$

To determine $\sigma_{x|m}^2$, consider the change in the variance of the particle position distribution due to a single move at position x_k. The change in the variance of $X(t)$ for a single move is given by

$$\sigma^2_{x|1} = \left(\left\langle x^2\right\rangle_f - \left\langle x^2\right\rangle_i\right) - \left(\langle x\rangle_f^2 - \langle x\rangle_i^2\right), \tag{3.30}$$

where the indices f and i refer to the final and initial states, respectively. The change in the squared first moment of the particle distribution (the second term in Equation 3.30) is given by

$$\langle x\rangle_f^2 - \langle x\rangle_i^2 = \left(\langle x\rangle_i + \frac{h}{N}\right)^2 - \langle x\rangle_i^2 = \frac{h}{N}\left(2\langle x\rangle_i + \frac{h}{N}\right). \tag{3.31}$$

The contribution to the change in the second moment of the particle distribution (the first term in Equation 3.30), which is only due to the particle at position x_k, is given by

$$\left\langle x^2\right\rangle_f - \left\langle x^2\right\rangle_i = \frac{x_k^2|_f - x_k^2|_i}{N} = \frac{(x_k + h)^2 - x_k^2}{N} = \frac{h}{N}\left(2x_k + h\right). \tag{3.32}$$

Equations 3.31 and 3.32 directly lead an expression for the change in the variance of $X(t)$ due to a particle at position x_k moving,

$$\sigma^2_{x|1}\left(x_k\right) = \frac{2h}{N}\left(x_k - \langle x\rangle_i\right) + \frac{h^2\left(N-1\right)}{N^2}. \tag{3.33}$$

Without particle blocking, the average of x_k in a Gaussian distribution is the same as $\langle x\rangle_i$. However, at finite concentration, particle blocking in the flow direction leads to a systematic bias in the selection process—only particles at the leading edge of a chains can be selected. For a single chain of length s, the front particle is $\frac{1}{2}\left(s-1\right)$ lattice units away from the mean of that chain. Averaged over all possible chain lengths, the resulting local systematic bias is given by

$$\left\langle x_k - \langle x\rangle\right\rangle = \frac{h}{2}\left(\left\langle s\left(x_k\right)\right\rangle - 1\right), \tag{3.34}$$

where $\langle s \rangle$ is the mean chain length at the local concentration, $C\left(x_k\right)$, which is given by

$$\left\langle s\left(x_k\right)\right\rangle = \frac{\sum_s s^2 \eta\left(x_k, s\right)}{\sum_s s \eta\left(x_k, s\right)} = \frac{1 + C\left(x_k\right)}{1 - C\left(x_k\right)}, \tag{3.35}$$

where the definition of the chain length probability, $\eta\left(x_k, s\right)$, from Equation 3.21 has been applied [118]. Equation 3.33 can be expressed as

$$\sigma^2_{x|m}\left(x_k\right) = m\left(\frac{h^2}{N}\frac{1 + C\left(x_k\right)}{1 - C\left(x_k\right)} - \frac{h^2}{N^2}\right), \tag{3.36}$$

where the contributions of m steps are considered. Finally the probability that a site at position x_k is chosen at any given time is $C\left(x_k\right)/N$, which leads to

$$\begin{aligned} \left\langle \sigma^2_{x|m} \right\rangle &= \langle m \rangle \left(\frac{h^2}{N} f\left(C\right) - \frac{h^2}{N^2}\right), \text{where} \\ f(C) &= \int_{-\infty}^{\infty} \frac{C\left(x\right)}{N} \frac{1 + C\left(x\right)}{1 - C\left(x\right)} \, \mathrm{d}x. \end{aligned} \tag{3.37}$$

Note that $N = \int_{-\infty}^{\infty} C\left(x\right) \mathrm{d}x$. Substituting Equations 3.29 and 3.37 into Equation 3.28 gives

$$\sigma^2_x = tvhf(C). \tag{3.38}$$

Because $C(x)$ is approximately constant in time over a small number of steps, $f(C)$ is also constant, so Equation 3.38 is linear in time and therefore may be represented by a numerical dispersion coefficient of the form

$$K_{\text{err}} = \frac{\sigma^2_x}{2t} = \frac{vh}{2} f(C). \tag{3.39}$$

For any Gaussian concentration profile, the effective dispersion error that is incurred by the PFA-LKMC algorithm scales linearly with the velocity and the lattice spacing and is an integral function of the concentration profile. This analysis was tested by comparing the apparent dispersion coefficient obtained from a PFA-LKMC simulation of a Gaussian solute pulse in straight-channel plug-flow with the result in Equation 3.39. The apparent dispersion coefficient in the LKMC simulations was obtained by computing the difference between the initial and final variance of the solute pulse concentration over a short time interval. Two types of runs were performed. In the first, particles were assumed to be nondiffusive, $D = 0$, and any measured dispersion therefore can be attributed to algorithm discretization error. In the second case, particles with finite diffusivity, $D > 0$, were simulated and the dispersive error was defined by the difference between the apparent dispersivity and particle diffusivity,

$$K_{\mathrm{err}} = \frac{\sigma_x^2}{2t} - D. \tag{3.40}$$

Equation 3.40 is valid for both $D = 0$ and $D > 0$. As shown in Figure 3.13, the simulated (Equation 3.40) and calculated (Equation 3.39) diffusive errors are in excellent quantitative agreement for variations in concentration, velocity, grid spacing, and grid Peclet number, vh/D. The error scales linearly with h, so it may be understood as a discretization error that is amplified by the presence of connected chains of particles. The fact that the calculated error in Equation 3.39 accounts for all excess algorithm dispersion indicates that this is the dominant error in the algorithm.

3.9 Conclusions

A new approach for incorporating convective transport of particles into LKMC was developed and validated. The method is applicable to systems of tracer solute particles that do not affect the fluid flow and do not interact hydrodynamically. The only particle interaction is excluded volume (site exclusion). It was shown that a straightforward addition of local convective rates to the diffusive rates of particles leads to shock-like propagation behavior, along with an artificial reduction in the average particle transport rate. Particle blocking on the lattice was found to cause a concentration-dependent drift velocity. The concentration-dependent drift was corrected by passing convective rates of blocked particles to the particles at the edge of the local chain of particles. The validity of this approach was established mathematically for one dimensional systems. The PFA-LKMC method was also shown to be accurate for two (or three) dimensional flows using an expansion flow geometry.

Although the rates of motion in this work do not satisfy the probabilities of the first passage problem [109, 120], the dispersion error analysis clearly demonstrates that the dominant error in the system considered here arises from particle blocking on the lattice. There also exists an inherent discretization error that scales as $vh/2$. No additional error was observable that could be attributed to violating the first passage problem over a single lattice move. The LKMC rates also do not satisfy detailed balance as the Peclet number increases; however, satisfying detailed balance is generally not critical for the highly nonequilibrium situations in flow-driven particle motion.

The PFA-LKMC method enables simulation of systems in which both convective and diffusive transport modes are operational. In the following chapters, PFA-LKMC will be utilized to study generalized bulk aggregation of particles in flow and as part of a multi-scale model of platelet deposition to a collagen surface. Beyond these specific applications, this approach enables stochastic simulation of diverse problems in systems biology, microfluidics, and nanomaterials processing, which span molecular to macroscopic length scales and are driven by fluid flow.

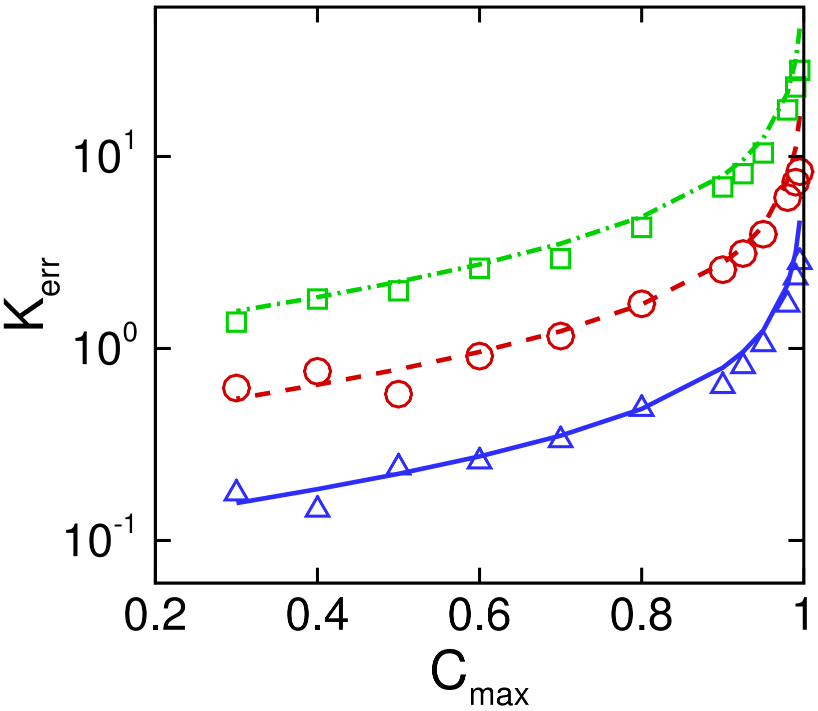

Figure 3.13: Dispersion error is proportional to the lattice spacing and velocity. Measured with an initial Gaussian pulse ($\sigma = 1$) in a one dimensional plug flow velocity profile as a function of the peak concentration, $C_{\max}$. The lines represent numerical evaluations of Equation 3.39 and the corresponding symbols are the results from the PFA-LKMC method over a short time interval, $\Delta t = 10^{-4}$. The blue triangles/line are with $h = 0.002$, $v = 100$, and $D = 0$ ($vh/2 = 0.1$,$Pe = \infty$). The red circles/line are with $h = 0.007$, $v = 100$, and $D = 0$ ($vh/2 = 0.35$, $Pe = \infty$). The green squares/line are with $h = 0.002$, $v = 1000$, and $D = 0.4$ ($vh/2 = 1$, $Pe = 5$). The Peclet number is defined with respect to the lattice spacing, $Pe = vh/D$.

Chapter 4

Aggregation in bulk particulate flows

In the previous chapter, a convective LKMC algorithm was developed to track particle motion in flow. In this chapter, the LKMC approach is extended to study particle aggregation in a bulk fluid. Typically, a population balance equation (PBE) approach is used to determined the dynamics of particle aggregation and fragmentation. However, a more direct method for simulating particle aggregation is needed for situations with complex flow. Simple cases that can be solved by the PBE are used to validate the LKMC method for perfect (ideal) and imperfect (nonideal) collision. A collision model for nonideal collisions is proposed, and a connection the mean-field PBE is derived. The LKMC method is then used to study open systems with simple flows including constant shear rate, parabolic velocity profile, and plug flow. The particle size distribution is determined for a complex flow with baffles, sudden expansions, and sudden contractions.

4.1 Population balance equation

Consider a two dimensional representation of a cone and plate geometry (constant shear rate) into which circular particles of uniform radius R_0 are initially placed with number concentration C_0. The initial volume fraction is given by $\phi = C_0 \pi R_0^2$. The computational domain that will be studied is represented by a rectangular box of size $L_x \times L_y$. A uniform shear rate, G, is applied in the the y dimension so that the velocity profile within the domain is

$$v_x\left(y\right) = Gy. \tag{4.1}$$

Periodic boundaries are applied in the direction of flow and no flux boundaries are imposed perpendicular to the direction of flow. The particles in the fluid are assumed to move along rectilinear paths until collision, i.e. no hydrodynamic or other long range particle interactions are explicitly modeled here.

The population balance equation for aggregates of size i is found by considering collisions that create and destroy particles of size i:

$$\frac{\mathrm{d}C_i}{\mathrm{d}t} = \frac{1}{2}\sum_{j=1}^{i-1} \epsilon k_{j,i-j} C_j C_{i-j} - \sum_{j=1}^{\infty} \epsilon k_{i,j} C_i C_j, \tag{4.2}$$

where $\epsilon k_{i,j} C_i C_j$ is the rate of aggregation between clusters of size i (an 'i-mer') and clusters of size j to form a clusters of size $i+j$. C_i and C_j are the number concentrations of i-mers and j-mers, respectively, and $k_{i,j}$ is the collision kernel that depends on the fluid flow. The first term, $\epsilon k_{j,i-j} C_j C_{i-j}$, is the rate of collisions that create particles of size i. The second term, $\epsilon k_{i,j} C_i C_j$, is the rate of collisions that destroy particles of size i. The collision efficiency, ϵ, is the probability that a collision event results in an aggregation event and can include hydrodynamic interactions and other interparticle interactions

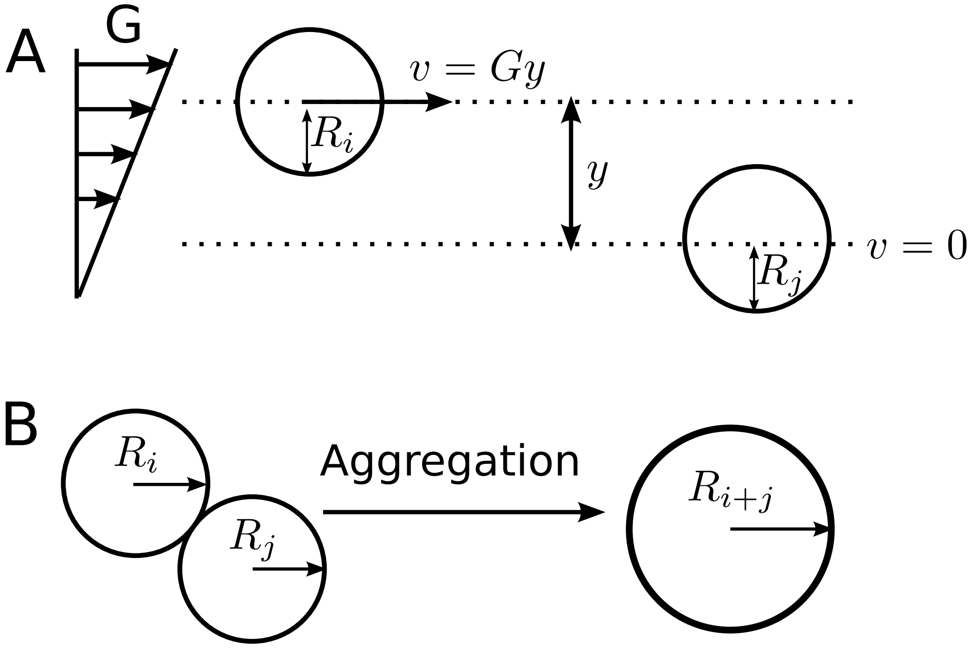

Figure 4.1: Particle collisions in constant shear flow. The flux of a particle j to a particle i is determined by the relative velocity of the particles, which depends on the separation distance perpendicular to the flow. The dotted lines represent the trajectories of the particles (A). If a particle with radius R_i aggregates with a particle of radius R_j, the resulting particle is immediately relaxed to a circular shape with radius $R_{i+j} = \sqrt{R_i^2 + R_j^2}$ (B).

such as receptor capture efficiency between individual cells [44, 45, 121, 122]. Particles that aggregate are assumed to immediate relax to circular particles, i.e. aggregation of particles of radius R_i and R_j result in a new particle of radius $\sqrt{R_i^2 + R_j^2}$. The collision kernel can be derived from the flux of particles of size j to particles of size i, $J_{i,j}$, with the following relation,

$$J_{i,j} = k_{i,j} C_i C_j. \tag{4.3}$$

Note that the total rate of aggregation is the flux, $J_{i,j}$, times the probability of a collision event, ϵ. The flux of particles of size j to particles of size i whose trajectories are separated by a distance y (see Figure 4.1) is given by

$$j_{i,j} = C_i C_j v(y) dy = C_i C_j G y \, \mathrm{d}y, \tag{4.4}$$

where $v(y)$ is the relative velocity of the particles. The total flux over all possible trajectories that lead to collision is given by

$$J_{i,j} = 2 \int_0^{R_i+R_j} C_i C_j G y \, \mathrm{d}y = C_i C_j G \left(R_i + R_j\right)^2 . \tag{4.5}$$

Using Equation 4.3, the collision kernel for constant shear flow is given by

$$k_{i,j} = G \left(R_i + R_j\right)^2 . \tag{4.6}$$

For comparison, the collision kernel for spheres in a constant shear flow is given by

$$k_{i,j} = \frac{4}{3} G \left(R_i + R_j\right)^3 \tag{4.7}$$

For the constant shear kernel, the PBE has no known analytic solution. Analytic solutions are only known for idealized kernels, e.g. the constant kernel, $k_{i,j} = c$. Several methods exist for solving a PBE numerically [123, 124]; a stochastic numerical solution approach [105] based on the Gillespie method for chemical kinetics [88, 108] is employed here. This approach is essentially a mean-field representation of the LKMC algorithm.

4.2 Lattice kinetic Monte Carlo algorithm

The lattice kinetic Monte Carlo (LKMC) algorithm in this chapter is based on the one in Chapter 3. However, particles are no longer restricted to occupying a single lattice site. As particles aggregate on the lattice, it is essential to resolve the different particle sizes to capture the size effects in the collision kernel (Equation 4.6). α is defined as the radial resolution of a particle on the lattice:

$$\alpha = \frac{R}{h}, \tag{4.8}$$

where R is the radius of the particle and h is the lattice spacing. As shown in Figure 4.2, a particle is centered on a lattice site and contains all lattice sites whose center is within the area of the particle.

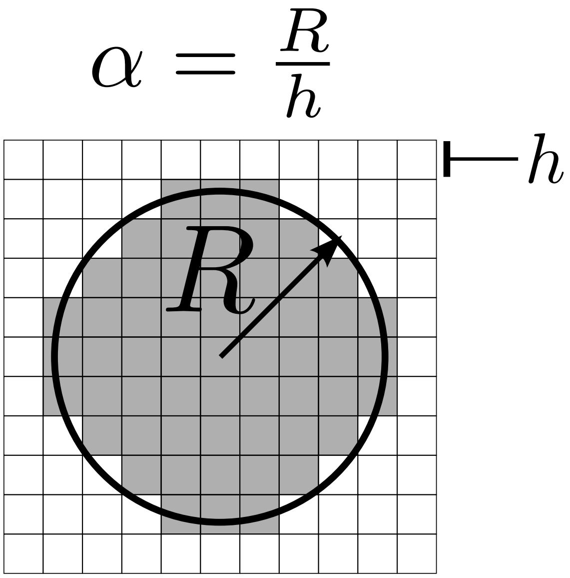

Figure 4.2: Discretization of particles on lattice. For a particle with radius R on a lattice with lattice spacing h, the center of the particle is located at the center of a lattice site, and the particle contains all lattice sites whose center is within the area of the particle. The level of discretization is given by $\alpha = R/h$.

The rate of moving the entire particle one lattice space by diffusion is still given by

$$\Gamma_D = \frac{D}{h^2}, \tag{4.9}$$

where D is the diffusion coefficient of the particle. The rate of convection along a lattice direction, $\mathbf{e}_i$, with velocity, $\mathbf{v}$, is given by

$$\Gamma_C = \frac{\max\left(0, \mathbf{v} \cdot \mathbf{e}_i\right)}{h}. \tag{4.10}$$

For directions that have a negative or zero velocity magnitude, the particles only move by diffusion. The particle velocity is given by the average velocity over all particle-occupied lattice sites. The total rate of motion is

$$\Gamma_{\mathrm{motion}} = \Gamma_C + \Gamma_D. \tag{4.11}$$

In this chapter, only particles driven by convective motion will be considered ($D = 0$). Site exclusion is enforced by setting the rate of events causing overlap to 0. In the low concentration limit, the algorithmic diffusive error that is introduced by discretizing the system is

$$D_{\mathrm{err}} = \frac{vh}{2}. \tag{4.12}$$

An error Peclet number can be defined on the particle scale, i.e.

$$Pe_{\mathrm{LKMC}} = \frac{vR}{D_{\mathrm{err}}} = \frac{vR}{vh/2} = 2\alpha. \tag{4.13}$$

Thus, for a purely convective situation ($D = 0$), Pe_{LKMC} remains finite because of algorithm diffusion, but can be increased arbitrarily by increasing α (increasing the grid resolution relative to a monomer radius). Increasing lattice resolution increases the number of moves required for a particle or aggregate to traverse a given distance, thereby increasing the computational cost of the simulation. Note, however, that the number of possible particle events at any time is unchanged as the lattice resolution is changed. It should also be noted that as the particle size distribution coarsens during a simulation, the effective value of Pe_{LKMC} actually increases (the relative contribution of spurious diffusion to the dynamics is reduced).

In addition to particle move events, when two particles are in contact on the lattice, an aggregation event occurs with a prescribed rate, Γ_{agg}, which is another input into the LKMC model. To match the test case presented in the previous section, after an aggregation event between particles of size R_i and R_j, the new particle of size $\sqrt{R_i^2 + R_j^2}$ is placed at the nearest lattice site to the center of mass of the original particles. If the new particle overlaps another particle on the lattice, the new particle is placed at the nearest position that has no overlap. Other types of aggregate morphological relaxation dynamics can be included into the LKMC framework by modeling the relaxation process explicitly; the idealized choice used in the following calculations simplifies the comparison to PBE model predictions. In the limit of perfect, or ideal, collision efficiency ($\epsilon = 1$), as soon as two particles come into contact an aggregation event occurs. This corresponds to the limit where $\Gamma_{\mathrm{agg}} = \infty$, which is computationally realized by setting Γ_{agg} many orders larger than the next largest rate in the system. For finite values of Γ_{agg}, the probability that an aggregation event occurs after particle contact is less than unity ($\epsilon < 1$). A model for imperfect, or nonideal, collisions that establishes a connection between a given value of ϵ and the corresponding Γ_{agg} is described in Section 4.4.

In the previous chapter, particles only occupied one lattice site ($\alpha = 1$) for all time. Here, particles can occupy multiple lattice sites ($\alpha \geq 1$) and a particle can be blocked by multiple other particles. The reverse situation is also possible, in which one particle directly blocks several others; examples are shown in Figure 4.3. The pass forward algorithm (PFA) is directly extended to these situations by evenly splitting the convective rate between particles in the direction of flow. For example, a particle that is being blocking by two particles (Figure 4.3A) passes its half rate to each particle in the direction of flow. Conversely, when one particle blocks two others, the sum of the blocked particle convective rates is passed forward to the blocking particle, as shown in Figure 4.3B.

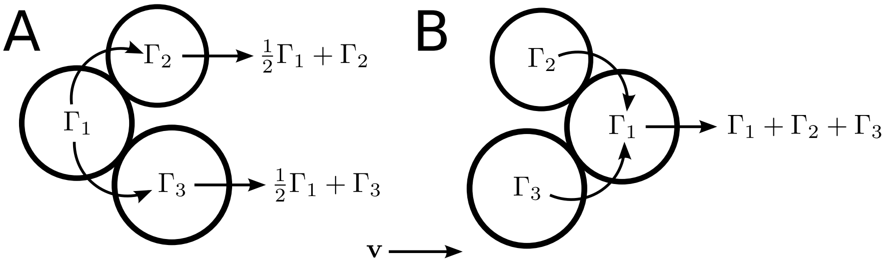

Figure 4.3: Rate passing scheme. (A) A particle can be blocked from moving in the direction of flow by two (or more) particles. In this case, particle 1 has convective rate Γ_1 and passes half this rate to particles 2 and 3. The total convective rates of particles 2 and 3 are $\frac{1}{2}\Gamma_1 + \Gamma_2$ and $\frac{1}{2}\Gamma_1 + \Gamma_3$, respectively. (B) A single particle can block two (or more) particles in the direction of flow. In this case particles 2 and 3 pass their convective rates to particle 1, which has a total convective rate of $\Gamma_1 + \Gamma_2 + \Gamma_3$.

4.3 Ideal ($\epsilon = 1$) aggregation in constant shear flow

The total concentration of particles in a constant-shearing fluid as a function of time is shown in Figure 4.4 for both the LKMC and PBE methods when $\epsilon = 1$ ($\Gamma_{\text{agg}} = \infty$). The rate at which particle coalesce decreases as the simulation progress due to the decreasing particle concentration. In fact, as shown in Equation 4.2, the aggregation rate is expected to scale as the square of the particle concentration. The agreement between the LKMC results and the PBE solution is strongly influenced by the resolution of the lattice. For coarse lattices, particles tend to aggregate too rapidly, an error that arises from the diffusive error (Equation 4.12), which creates additional collisions. This error decreases as the lattice spacing decreases, and for values of α greater than approximately 10, the LKMC results match the PBE for all simulated time. A more detailed comparison between the two methods at a specific time is shown in Figure 4.5, where individual components of the overall size distribution are shown. For $\alpha = 15$ at $t = 500\,\text{s}$, the agreement is quantitative within the spread of the LKMC results. The temporal evolution of the concentration of the first 4 particle sizes for the PBE and LKMC is compared in Figure 4.6. For both the PBE and LKMC, the system starts with all monomers that decay monotonically. All clusters come to a maximum and then decay, where the time to maximum is shorter for smaller clusters. For all cluster sizes, the LKMC matches the PBE over the simulated time.

4.4 Nonideal ($\epsilon < 1$) aggregation in constant shear flow

The lack of explicit hydrodynamic interparticle interactions in the present LKMC algorithm can create artifacts in the nonideal collision case. Consider the situation where a faster-moving particle approaches a slower-moving one and becomes blocked. In the ideal collision case, instantaneous aggregation results, and a new, single particle is created. In

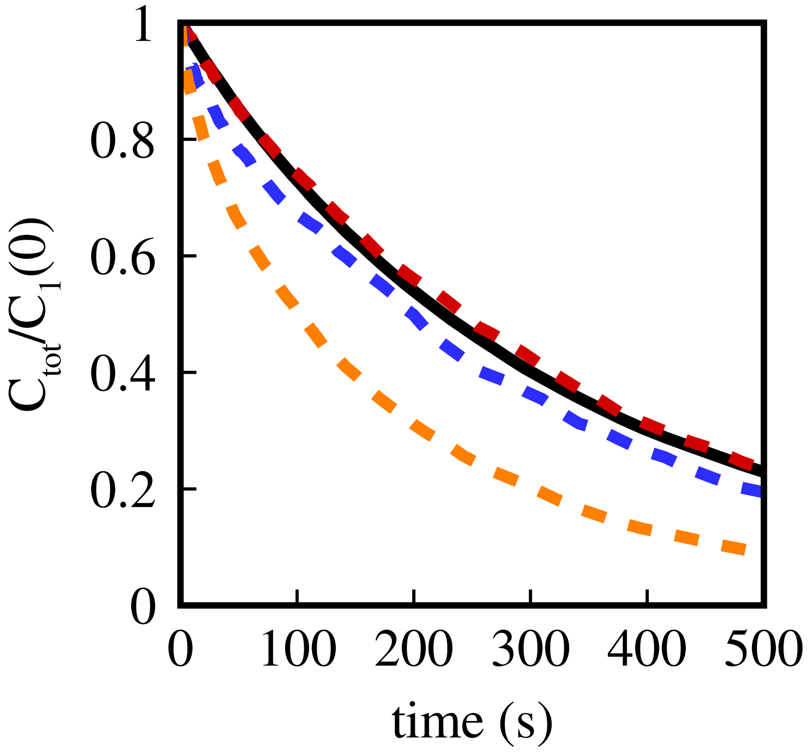

Figure 4.4: Total particle concentration compared for LKMC and PBE for ideal aggregation of particles at constant shear rate with $\phi = 0.005$, $G = 1\,\mathrm{s}^{-1}$, $\epsilon = 1$, $L_x = 40$, $L_y = 0.3$, and $R_0 = 0.01$. The total particle concentration, $C_{\mathrm{tot}} = \sum C_i$, is normalized by the initial monomer concentration, $C_1(0)$. Black, PBE; orange, LKMC $\alpha = 1$; blue, LKMC $\alpha = 5$; red, LKMC $\alpha = 15$.

the nonideal case (finite Γ_{agg}), however, the blocking cannot be resolved until the particles aggregate. In other words, an aggregation event will take place for every collision even when Γ_{agg} is very small, because there is no mechanism for the colliding particles to disentangle following the collision. In reality, lubrication forces allow particles to slide around each other over a finite time interval.

This difficulty is resolved by introducing an additional event, namely the switching of coordinates in the direction of flow of a pair of particles, as shown in Figure 4.7.

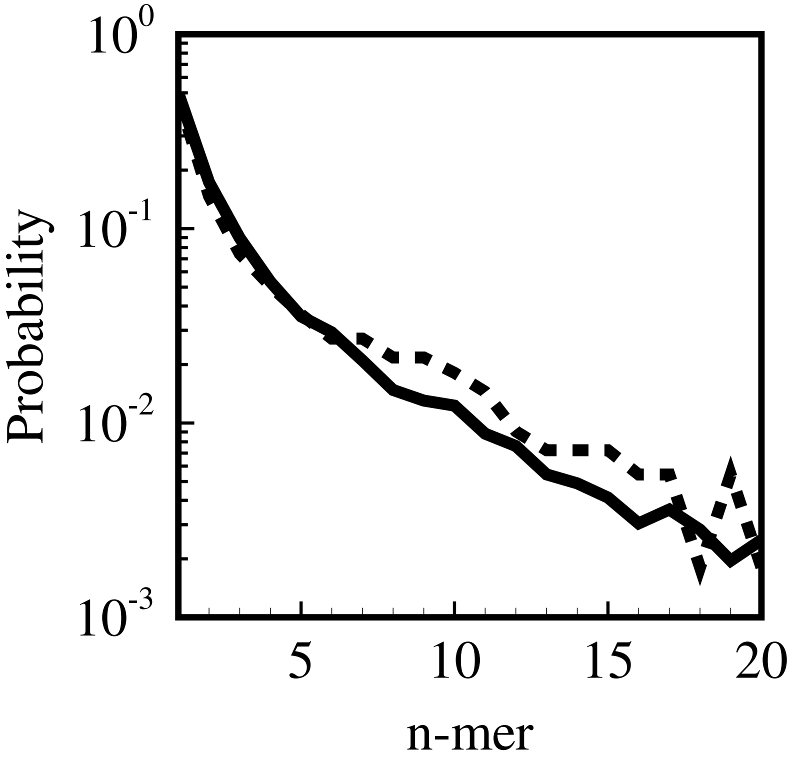

Figure 4.5: Distribution of particle sizes at $t = 500\,\mathrm{s}$ at constant shear with the same conditions as Figure 4.4 for PBE (solid line) and LKMC (dotted line) with $\alpha = 15$.

Consider two nearest-neighbor particles, i and j, colliding at an angle θ with respect to the direction of flow (see Figure 4.7). The interaction time for this event is assumed to be $\Delta t = 2r\cos\theta/\Delta v$, where r is the magnitude of the vector pointing from one particle center to the other particle center, and Δv is the velocity difference between the two particles. The timescale for switching as a function of contact angle and local shear rate, G, is given by

$$\Delta t = \frac{2}{G}\cot\theta. \tag{4.14}$$

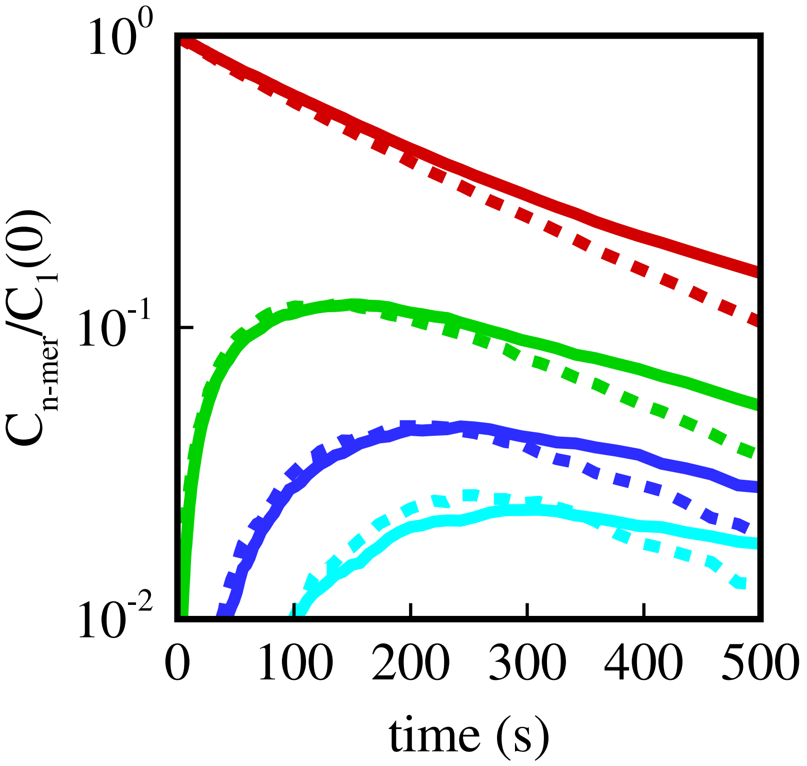

Figure 4.6: Temporal evolution of the concentration of the first four particle sizes at constant shear rate with the same conditions as Figure 4.4 for PBE (solid lines) and LKMC (dotted lines) with $\alpha = 15$. Red, monomer; green, 2-mer; blue, 3-mer; cyan, 4-mer.

The corresponding rate expression for pair switching is given by

$$\Gamma_{\text{flip}} = \frac{G}{2} \tan\theta. \tag{4.15}$$

To compare LKMC to the PBE, a quantitative connection between the collision efficiency parameter, ϵ, the switching rate, Γ_{flip}, and the aggregation rate, Γ_{agg} is needed. Over the contact time interval, and for a given (constant) aggregation rate, the probability that two particles have not aggregated is exponentially distributed $P_0 = \exp\left(-\Gamma_{\text{agg}}\Delta t\right)$.

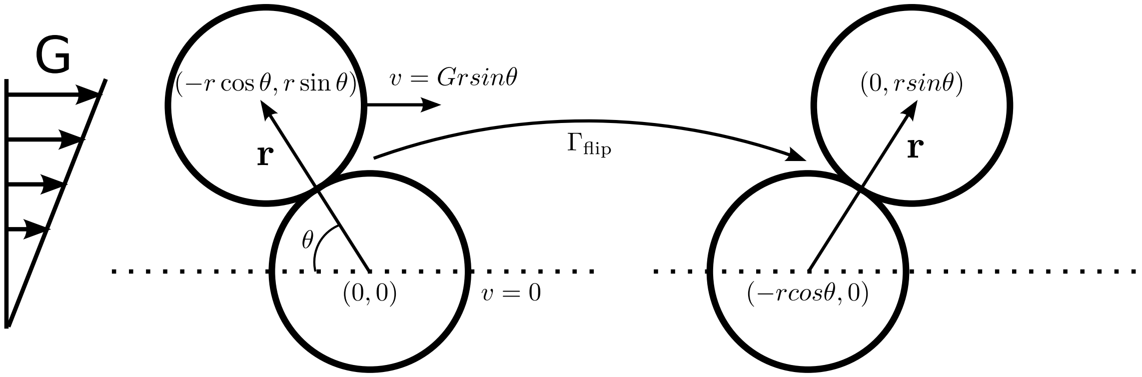

Figure 4.7: Particle switches create nonideal collisions in LKMC. The vector that points from the center of the reference sphere to the center of the colliding sphere is $\mathbf{r}$, which makes an angle θ to the direction of flow and has a magnitude of $r = R_i + R_j$, where i and j are the reference and colliding spheres. At a local shear rate G, the colliding particle has a relative velocity of $Gr\sin\theta$. The colliding particle moves $r\cos\theta$ and the reference particle moves $-r\cos\theta$ in the direction of flow during a particle switch event. For a more complex flow, the velocity vector is decomposed in the lattice directions and the switching rate is calculated independently for each direction.

Therefore, the probability that the particles have aggregated during a collision with a specific angle of contact, θ is given by

$$P(\theta) = 1 - \exp\left(-\Gamma_{\text{agg}}\Delta t\right) = 1 - \exp\left(-2\frac{\Gamma_{\text{agg}}}{G}\cot\theta\right). \tag{4.16}$$

The collision efficiency is the probability that *any* collision between two particles will produce a successful aggregation event. The collision efficiency within an LKMC simulation is generally given by

$$\epsilon = \frac{\int_0^{\pi/2} J(\theta)P(\theta)\,\mathrm{d}\theta}{\int_0^{\pi/2} J(\theta)\,\mathrm{d}\theta}, \tag{4.17}$$

where $J(\theta)$ is the flux of particles arriving at a reference particle with collision angle θ. In the case of rectilinear particle trajectories with locally constant shear rate, the arrival flux is given by (compare to Equations 4.4 and 4.5 where the flux is defined in Cartesian coordinates)

$$J(\theta) = C_j G \left(R_i + R_j \right) \sin\theta. \tag{4.18}$$

Note that the arrival flux is nonuniform and increases with increasing contact angle. Inserting Equation 4.18 into Equation 4.17 provides an expression of the average sticking probability based on LKMC parameters,

$$\epsilon = 1 - \int_0^{\pi/2} \sin\theta \exp\left(-2\frac{\Gamma_{\mathrm{agg}}}{G} \cot\theta \right) \mathrm{d}\theta. \tag{4.19}$$

The collision efficiency is therefore explicitly dependent on the dimensionless ratio of the aggregation rate to the shear rate, Γ_{agg}/G.

As shown in Figure 4.8, the integral expression in Equation 4.19 was evaluated numerically for $10^{-3} < \Gamma_{\mathrm{agg}}/G < 10^{3}$. When the aggregation rate is large relative to the shear rate, the ideal aggregation limit is obtained and $\epsilon \approx 1$. As the aggregation rate becomes small relative to the shear rate, $\epsilon \rightarrow 0$. The crossover between ideal collisions and non-ideal collisions appears naturally at $\Gamma_{\mathrm{agg}}/G \approx 1$, confirming the relevance of this ratio in dictating the overall collision efficiency. Equation 4.19 and Figure 4.8 provide the correspondence between the spatially resolved particle interactions, through the rate of aggregation and the interaction time, and the spatially averaged collision efficiency in the PBE. Since the interaction time depends only on the local flow characteristics in this model, only one free parameter, Γ_{agg}, needs to be specified in LKMC.

LMKC simulations of aggregation in constant shear flow were performed for $10^{-2} < \Gamma_{\mathrm{agg}}/G < 10^{2}$ and $G = 1\,\mathrm{s}^{-1}$. The temporal evolution of the total concentration of clusters for the different cases is compared to the corresponding PBE simulations in Figure 4.9. In each PBE case, the corresponding value of ϵ was obtained from numerical

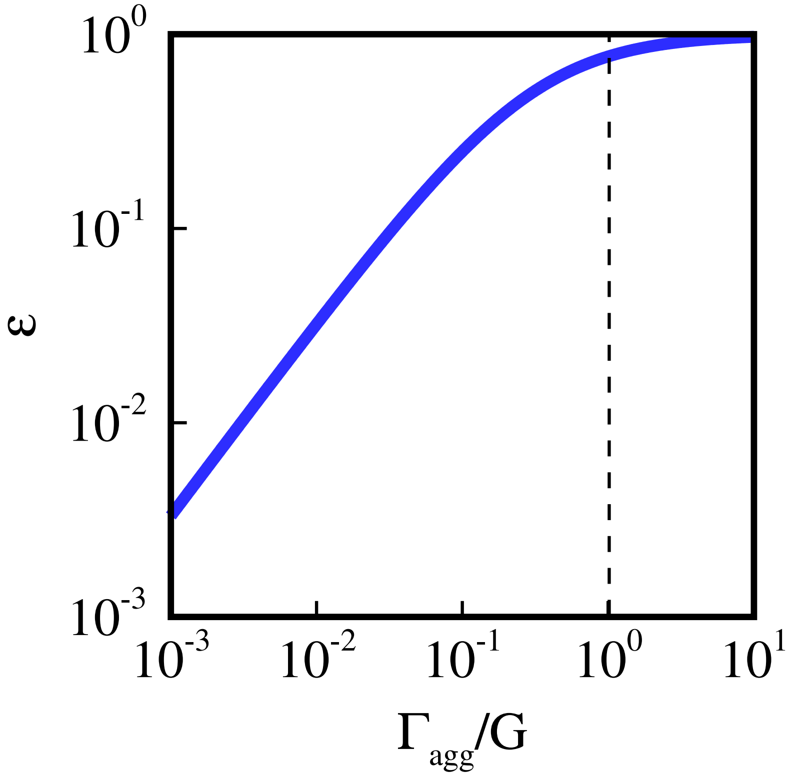

Figure 4.8: Collision efficiency in LKMC simulation. Numerical integration of collision efficiency varying with the ratio of the aggregation rate to the shear rate (Equation 4.19).

integration of Equation 4.19 (Figure 4.8), and agreement between the two simulation approaches is observed over 4 orders of magnitude in the ratio Γ_{agg}/G. Note that for coarse size distributions, the total number of clusters is small, and the corresponding statistical fluctuations in the LKMC result become larger. To avoid this type of error in numerical solutions of the PBE, the constant number Monte Carlo (CNMC) method [124] aims to keep the number of clusters constant throughout the simulation by increasing the size of the simulation domain considered. The CNMC method is a solution method for the mean-field PBE. In principal the constant number principal could be applied to the LKMC method, but would require replicating the system in the direction of flow, which

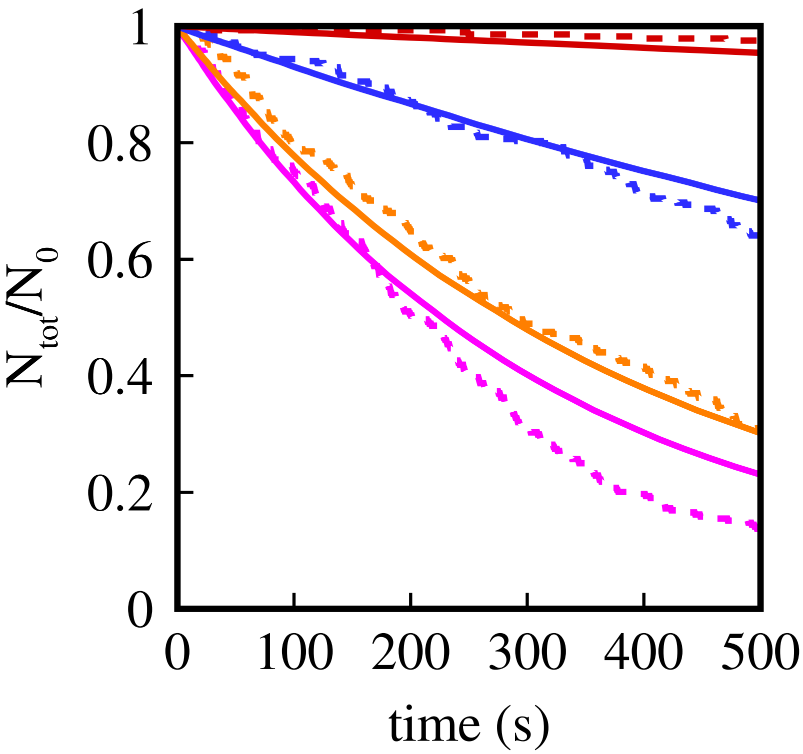

Figure 4.9: Comparison between LKMC (dashed lines) for various ratios of aggregation rate to shear rate (red, $\Gamma_{\text{agg}}/G = 0.01$; blue, $\Gamma_{\text{agg}}/G = 0.1$; orange, $\Gamma_{\text{agg}}/G = 1$; and purple, $\Gamma_{\text{agg}}/G = 100$) and PBE (solid lines) with corresponding collision efficiency determined from numerical integration from Equation 4.19 (Figure 4.8). $G = 1\,\text{s}^{-1}$, $\phi = 0.0005$, $\alpha = 10$, $L_x = 20$, $L_y = 1$, and $R_0 = 0.001$ for all LKMC simulations.

may incur computational penalties or statistical errors.

4.5 Platelet aggregation in tubular channels

In this section, the contact time model is compared to the behavior of a physical system with hydrodynamic interactions and cellular bonding. Bell et al. have measured size distributions of adenosine diphosphate (ADP)-stimulated platelet aggregates at the outlet of a tube at four average shear rates: 41.9, 168, 335, and $1000\,\text{s}^{-1}$ [31]. By assuming a linear velocity profile at the average shear rate of the tube, it was possible to extract an effective collision efficiency for platelets. Overall, the collision efficiency was found to decrease with increasing shear rate, a result that is qualitatively consistent with the particle interaction model used here.

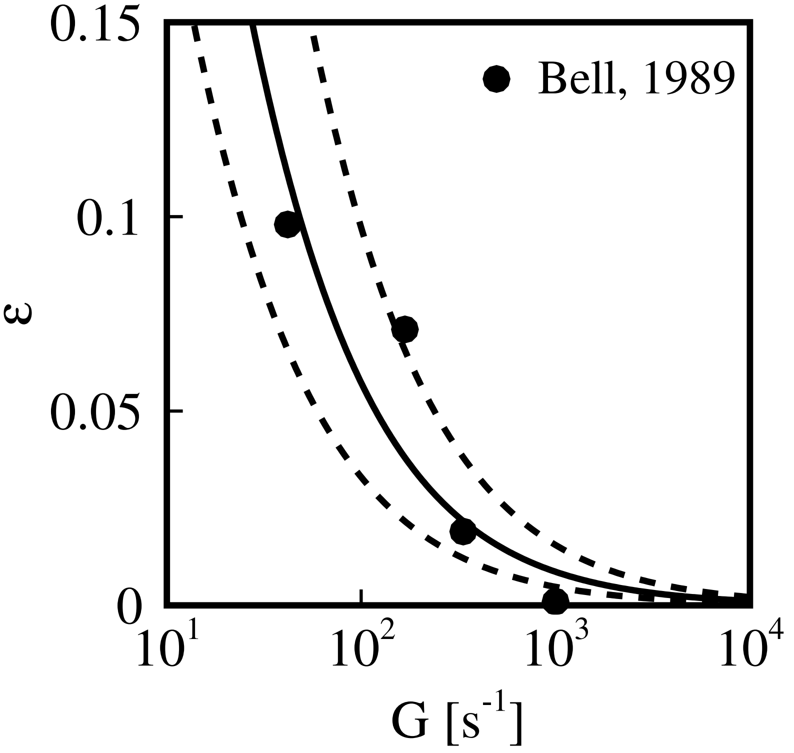

Figure 4.10: Comparison of contact time model with experimentally determined collision efficiencies for ADP-stimulated platelet aggregation. Circles, Bell et al. data [31]. Solid line, contact time model with a best-fit aggregation rate of $0.683\,\mathrm{s}^{-1}$; dotted lines, contact time model with an aggregation rate of $0.683 \pm 50\,\%$.

To compare the results of Bell et al. and the contact time model, the single aggregation rate parameter, Γ_{agg}, that best matches the experimentally derived collision efficiency at each shear rate was found to be $\Gamma_{\mathrm{agg}} = 0.683\,\mathrm{s}^{-1}$. As shown in Figure 4.10, the contact time model used in the LKMC method provides a good quantitative description of the shear-rate dependence on the collision efficiency for platelets. The dotted lines represent ±50 % of the regressed rate of aggregation, which captures some of the uncertainty due to the approximations used to calculated the collision efficiency in Bell et al. The regressed aggregation rate can be qualitatively interpreted in terms of the time required to form bonds that are strong enough to hold platelets together. The value of $\Gamma_{\text{agg}} = 0.683\,\text{s}^{-1}$ is a net aggregation rate that characterizes the result of fast (but unstable) GPIb-von Willebrand Factor bonds and slower (but stable) glycoprotein $\alpha_{2b}\beta_3$-fibrinogen bonds. Multiple bonds between $\alpha_{2b}\beta_3$ on one platelet and bound fibrinogen molecules on another platelet (and vice versa) are required for stable aggregation, and $\Gamma_{\text{agg}} = 0.683\,\text{s}^{-1}$ is consistent with $O(1\,\text{s})$ time for multiple high affinity $\alpha_{2b}\beta_3$-fibrinogen complexes to form (a single $\alpha_{2b}\beta_3$-fibrinogen bond requires $O(0.1\,\text{s})$ to form [125]).

4.6 Aggregation in nonperiodic, open systems

In an open system, the aggregation process takes place along a domain of finite length with particles entering the domain and leaving the domain. Four types of flow are considered here: plug flow, constant shear flow, parabolic (parallel-plate) flow, and a more complex situation with baffles. In the following simulations, the inlet condition is a fixed particle volume fraction of monomers with a uniform radius distribution, $R_0 = 0.01$. This inlet condition is implemented by defining a new event in the LKMC simulation that inserts a particle into the domain such that the center of mass is R_0/h lattice units from the boundary, which allows for the insertion of the entire particle onto the lattice. The rate for inserting a particle with center of mass located at a specific lattice site i is proportional to the total flux of fluid through that lattice site, $v_i h$ where v_i is the velocity magnitude normal to the boundary, and the concentration of monomer particles in the inlet, C_0,

$$\Gamma_{\text{inlet}}(i) = v_i h C_0. \tag{4.20}$$

Only the overall inlet rate, $\sum \Gamma_{\text{inlet}}(j)$, where the summation is over valid inlet sites, is used as an event in LKMC to determine when a new particle is inserted into the domain. After that event is chosen to occur, the particle's center of mass is placed at a specific lattice site i with probability $\Gamma_{\text{inlet}}(i)/\sum \Gamma_{\text{inlet}}(j)$. If this causes particle-particle overlap, this site is rejected and a new site is chosen until site exclusion is satisfied.

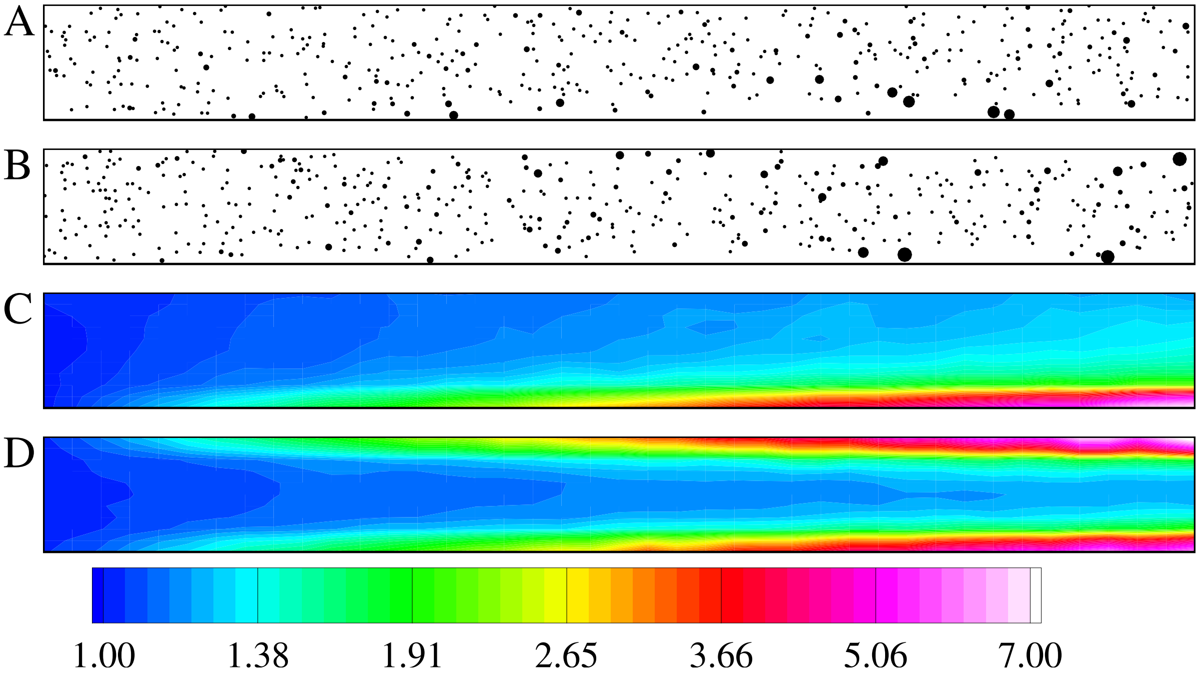

Figure 4.11: Comparison of particle size for constant shear rate and parabolic velocity profile in an open system. Flow is from left to right with dimensions $L_x = 20$ and $L_y = 1$. The aspect ratio of each panel is enhanced to 10:1 for readability. $\alpha = 1$, $h = 0.001$, $\phi = 0.01$, and $R_0 = 0.01$. **(a,c)** constant shear rate with an average velocity of 2×10^5. **(b,d)** Parabolic velocity profile with an average velocity of 2×10^5. **(a–b)** Snapshot of particles during an LKMC simulation. Radii of particles enhanced by a factor of 3. **(c–d)** Colorbar represents the average particle size relative to the monomer size, $\left(\langle R\rangle / R_0\right)^2$.

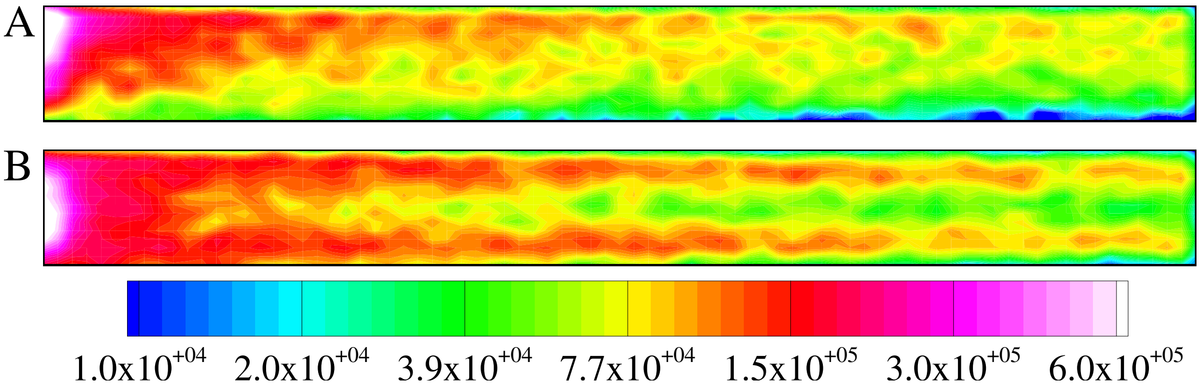

Figure 4.12: Comparison of aggregation rate for constant shear rate and parabolic velocity profile in an open system. Colorbar is in units of aggregation events per unit area time. Flow is from left to right with dimensions $L_x = 20$ and $L_y = 1$. The aspect ratio of each panel is enhanced to 10:1 for readability. $\alpha = 10$, $h = 0.001$, $\phi = 0.01$, and $R_0 = 0.01$. (a) constant shear rate with an average velocity of 2×10^5.(b) Parabolic velocity profile with an average velocity of 2×10^5.

In the following examples, a finite, rectangular domain with dimensions, $L_x = 20$, $L_y = 1$ was employed. A uniformly distributed square lattice with $h = 0.001$ was used in all cases. In the constant shear case, the prescribed velocity profile is given by

$$v_x(y) = 2 \times 10^5 y, \tag{4.21}$$

while the parabolic velocity profile is given by

$$v_x(y) = 3 \times 10^5 \left(1 - y^2\right). \tag{4.22}$$

In the latter case, the y origin is defined at the centerline of the domain. The total flow rate in both cases is the same. Steady-state quantities, averaged over sufficiently long time intervals, are measured for open systems whereas time-dependent quantities were measured in Figures 4.4–4.6 and 4.9. In Figure 4.11, the average particle sizes in a fluid with constant shear rate and with parabolic velocity profile are compared. As expected, the largest particles were found in regions with the longest residence time; in both cases, these regions were adjacent to the channel walls. In parabolic velocity profile, the region near the wall also exhibits the highest shear rate. The aggregation rates at steady state are compared in Figure 4.12. Note that although the shear rate was constant across the height of the domain in constant shear flow (Figure 4.12A), the aggregation rate was found to vary across the width of the channel. The reason for this apparently anomaly is a direct consequence of the variation in residence time across the height of the channel. Thus, more time for particle aggregation is available in the slower-moving streamlines and the aggregation rate decreases more rapidly with distance along the length of the channel (aggregation rate scales as GC^2, see Equation 4.2). In the parabolic case, the y locations with the highest aggregation rate along the channel occur near, but not at, the plate surfaces. These regions present an optimal balance between high shear rate and relatively low residence time.

The particle size distributions exiting the two channels are compared in Figure 4.13. Although the total flow rate is the same in all three cases, the parabolic flow example leads to the largest particles on average. The reason for this can be understood mathematically by considering an approximate solution to the PBE in which all particles are assumed to be the same size ($R_i \approx R_j = R_\infty$) [43]. The PBE becomes

$$\frac{\mathrm{d}C_\infty}{\mathrm{d}t} = -2G\epsilon R_\infty^2 C_\infty^2, \tag{4.23}$$

where C_∞ is the overall concentration of particles. Equation 4.23 can be simplified using

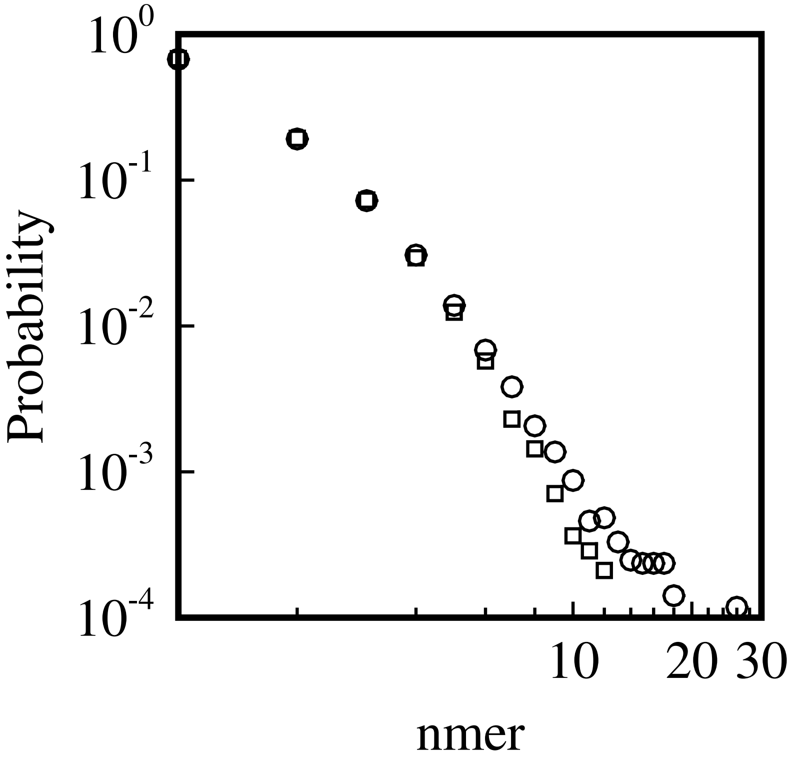

Figure 4.13: Outlet particle size distribution at steady state for open systems. Squares, constant shear rate; circles, parabolic velocity profile. The conditions are the same as in Figures 4.12 and 4.11.

the definition of the volume fraction, which is constant,

$$\phi = \pi R_\infty^2 C_\infty. \tag{4.24}$$

Thus

$$\frac{\mathrm{d}C_\infty}{\mathrm{d}t} = -\frac{2\phi}{\pi} G C_\infty. \tag{4.25}$$

Integrating over a particular streamline in unidirectional flow with a velocity magnitude,

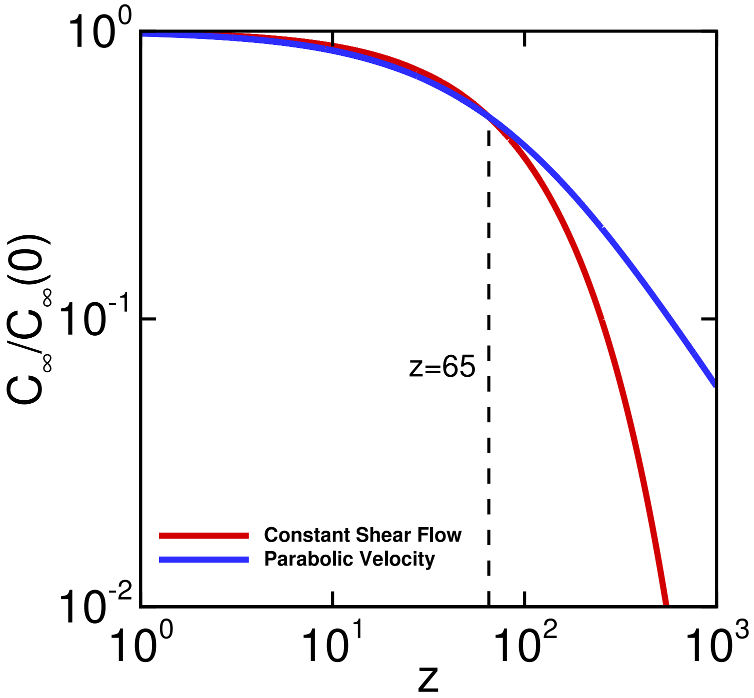

Figure 4.14: Comparison of the mixing-cup averaged particle concentration from an approximate analytic solution (Equations 4.30 and 4.31). Blue line, parabolic velocity profile; red line, flow with constant shear rate. z is the ratio of the channel length to width. The cross-over point occurs at $z \approx 65$

v, gives

$$C_\infty = C_\infty(0)\exp\left(-\frac{2\phi}{\pi}G\frac{x}{v}\right), \tag{4.26}$$

where x is the distance along the streamline (x/v is the residence time), and G is the local shear rate [46]. The mixing-cup averaged concentration of particles exiting the channel is then given by

$$\bar{C}_\infty = \frac{\int vC_\infty(y)\,\mathrm{d}y}{\int v\,\mathrm{d}y}. \tag{4.27}$$

For a parabolic velocity profile in a channel of half-height, 0.5, the concentration exiting

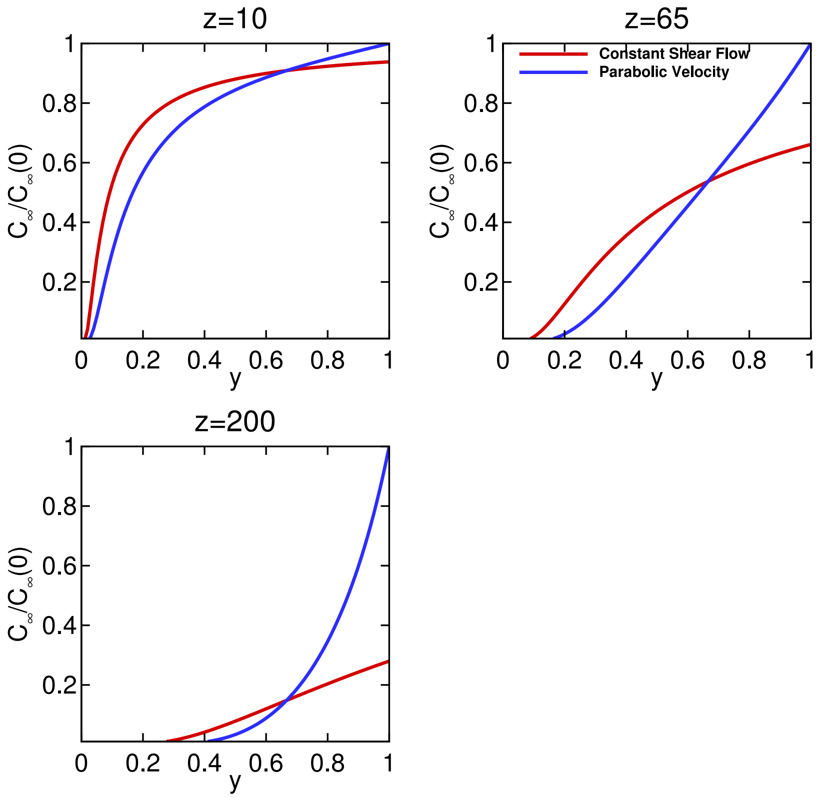

Figure 4.15: Comparison of the particle concentration from an approximate analytic solution (Equations 4.28 and 4.29). Blue line, parabolic velocity profile; red line, flow with constant shear rate. z is the ratio of the channel length to width, and y is the fractional distance width of the channel in constant shear rate and the fractional distance to the half-height in parabolic velocity flow. The cross-over point occurs at $z \approx 65$

at a particular streamline at a distance y from the center is

$$C_\infty = C_\infty(0) \exp\left(-\frac{8\phi z}{\pi}\frac{y}{1-y^2}\right), \tag{4.28}$$

where z is the ratio of the length of the channel to the height of the channel, $2H = 1$.

For constant shear rate flow, the concentration exiting at a particular streamline at a distance y from the stationary wall with channel width 1 is

$$C_\infty = C_\infty(0) \exp\left(-\frac{2\phi z}{\pi}\frac{1}{y}\right), \tag{4.29}$$

where z is the ratio of the length of the channel to the height of the channel, $H = 1$. The mixing-cup averaged concentration for a parabolic velocity profile is

$$\bar{C}_\infty = \int_0^1 \frac{3}{2}\left(1 - y^2\right) \exp\left(-\frac{8\phi z}{\pi}\frac{y}{1 - y^2}\right), \tag{4.30}$$

The mixing-cup averaged concentration for flow with a constant shear rate is

$$\bar{C}_\infty = \int_0^1 2y \exp\left(-\frac{2\phi z}{\pi}\frac{1}{y}\right), \tag{4.31}$$

Note that the concentration and mixing-cup averaged concentration is only dependent on the *shape* of the velocity profile and the length-to-width ratio of the channel. They do not depend on the velocity magnitude. Numerical solution of Equations 4.30 and 4.31 (Figure 4.14) demonstrates that for short channels, slightly more aggregation takes place in a parabolic velocity field, consistent with results in Figure 4.13 (lower concentration or larger particles). However, as the channel length increases, the averaged aggregation extent becomes greater in the constant shear rate case. The crossover occurs at a length-to-height ratio of 65. To understand the differences at high and low shear rate, the concentrations at several channel ratios are plotted in Figure 4.15. For any size channel with parabolic velocity profile, the concentration of particles at the center ($y = 1$) is unchanged, $C_\infty = C_\infty(0)$, since the shear rate is 0. For constant shear rate flow in long channels, the concentration of particles throughout the channel is much lower than the initial value ($C_\infty < C_\infty(0)$). So, for long channels, constant shear flow will produce coarser particles in the outlet. However, for short channels ($z < 65$), the concentration is lower in a larger region near the wall in parabolic velocity flow.

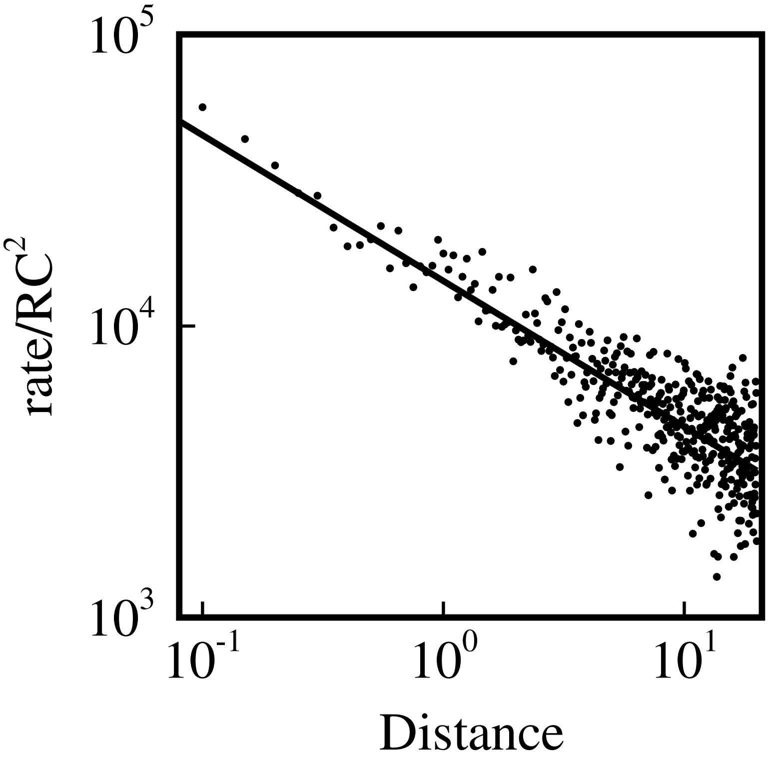

Figure 4.16: Comparison of 1D Brownian aggregation kernel from Equation 4.36 (line) to plug flow LKMC simulation (symbols). The radius of particles in LKMC is taken as the average particle radius at that position. $L_x = 20$, $L_y = 1$, $\alpha = 10$, $h = 0.001$, $\phi = 0.01$, $R_0 = 0.01$, and $v = 2 \times 10^5$.

Plug flow also leads to measurable aggregation (Figure 4.16), even though the aggregation kernel should be zero ($G = 0$). The aggregation is driven by algorithmic diffusion in the LKMC simulation. The extent of aggregation can be determined from the time-dependent aggregation kernel in 1D since the diffusion only occurs in the direction of flow. Consider a set of particles at initial concentration C_0 diffusing in one dimension. A fixed, reference particle is defined at the origin and the flux of particles from the positive x direction are considered. The boundary condition at the surface of the reference particle is $C(0,t) = 0$ for ideal collisions. To compare the results to the pseudo-steady aggregation kernel, we assume that the far-field concentration does not change, i.e. $C(\infty, t) = C_0$. The concentration profile around the reference sphere is given by the diffusion equation

$$\frac{\partial C}{\partial t} = 2D\frac{\partial^2 C}{\partial x^2}, \tag{4.32}$$

where the factor of 2 arises from fixing the reference particle. The solution for this PDE collapses onto a single solution with respect to a penetration length that grows as the square root of time as

$$C(x,t) = C_0 \mathrm{erf}\left(-\frac{x}{g(t)}\right), \text{ where } g(t) = 2\sqrt{2Dt}. \tag{4.33}$$

The flux of particles to the reference particle surface at $x = 0_+$ is

$$J_+ = -2R_{\text{collision}} D \left.\frac{\partial C}{\partial x}\right|_{x=0_+} = 2\left(R_i + R_j\right)\left(\frac{2D}{\pi t}\right)^{\frac{1}{2}} C_0, \tag{4.34}$$

where $\partial C/\partial x|_{x=0_+} = C_0\sqrt{2/\pi D t}$, $R_{\text{collision}} = R_i + R_j$, and the subscript $+$ indicates flux of particles from the positive x direction. The total flux per unit area is

$$J = \frac{1}{2}\left(|J_-| + |J_+|\right) C_0 = 2\left(R_i + R_j\right)\left(\frac{2D}{\pi t}\right)^{\frac{1}{2}} C_0^2, \tag{4.35}$$

where the factor of 1/2 arises from double counting collisions and the absolute value of the flux from the positive and negative directions are equal. The kernel is then given by

$$k_{i,j} = 2\left(R_i + R_j\right)\left(\frac{2D}{\pi t}\right)^{\frac{1}{2}} \tag{4.36}$$

The Brownian kernel with the algorithmic diffusion coefficient (Equation 4.12) explains the aggregation seen in plug flow (Figure 4.16). The particle size increases slowly along the channel relative to the shear driven processes in Figure 4.11, and the extent of aggregation due to algorithmic diffusion can be controlled by increasing the grid resolution relative to the monomer size.

4.7 Aggregation in complex flows: Parallel plate reactor with baffles

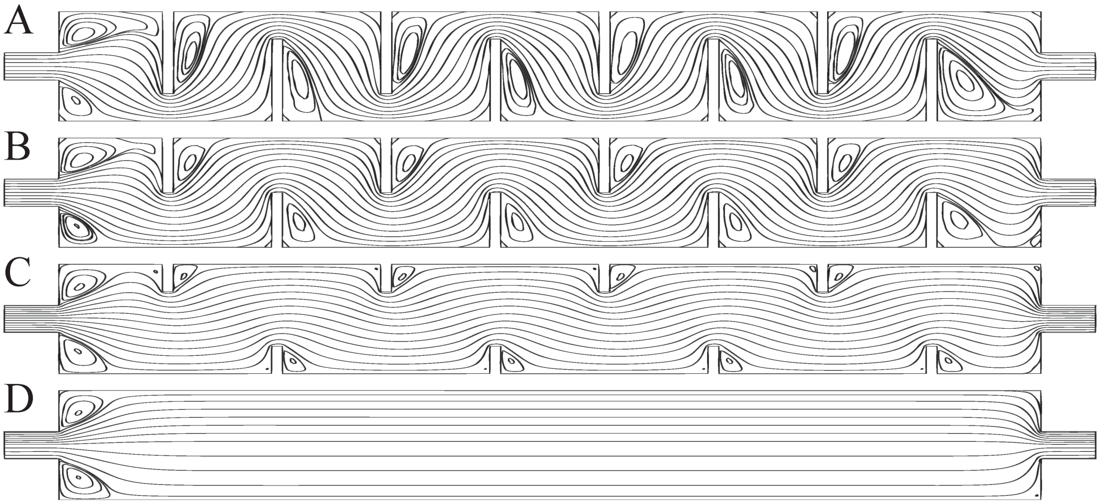

Figure 4.17: Geometry of baffle reactors with flow from left to right. Overall dimensions of $L_x = 20$ and $L_y = 2$. Inlet and outlet have length 1 and width 0.5. Baffles are 0.2 units thick and (a) 1.5 units, (b) 1 unit, (c) 0.5 units, and (d) 0 units long. $\alpha = 10$, $h = 0.00133$, $\phi = 0.02$, $R = 0.00133$.

The aggregation LKMC model was used to investigate particle aggregation in a system with complex flow. A rectangular channel with sudden expansions and contractions and varying baffle heights was considered. The choice of this type of flow geometry is applicable to realistic situations in which there are regions of high residence time (standing vortices) and regions of high shear rate (squeezing flow), e.g. stenotic and valvular flows in blood vessels or flow in shell-and-tube heat exchangers). Such geometries cannot be considered in the mean-field PBE framework, necessitating the use of a spatially resolved approach. The LKMC simulation domain considered here includes a total of eight baffles that are equally spaced and originate from alternating channel walls, as shown in Figure 4.17. Four cases were considered in which the baffle height was varied from 0 to 0.75 of the channel width. The resulting flow streamlines for each case are shown in Figure 4.17. The fluid is incompressible, and the average normal velocity in the inlet is 20 ($Re = 10$). The velocity field for each geometry was determined by a finite element solution of the Navier-Stokes equation (COMSOL Multiphysics).

The particle aggregation rates are shown for all four cases in Figure 4.18. The effect of the baffles is generally to locally increase the shear rate and therefore the aggregation rate, an effect that increases with increasing baffle height. Note that as the particles coarsen, the aggregation rate decreases down the channel due to lower particle concentration. In the recirculation regions adjacent to each baffle, the aggregation rate is low corresponding to the very low shear rate there. The corresponding average particle size distribution for each case is shown in Figure 4.19. Most notably, extremely large particles were found in the recirculation regions where the residence time is very long, leading to a broad size distribution at the reactor exit. This often undesirable effect increases with increasing baffle height, demonstrating how the present simulation tool could be used to optimize

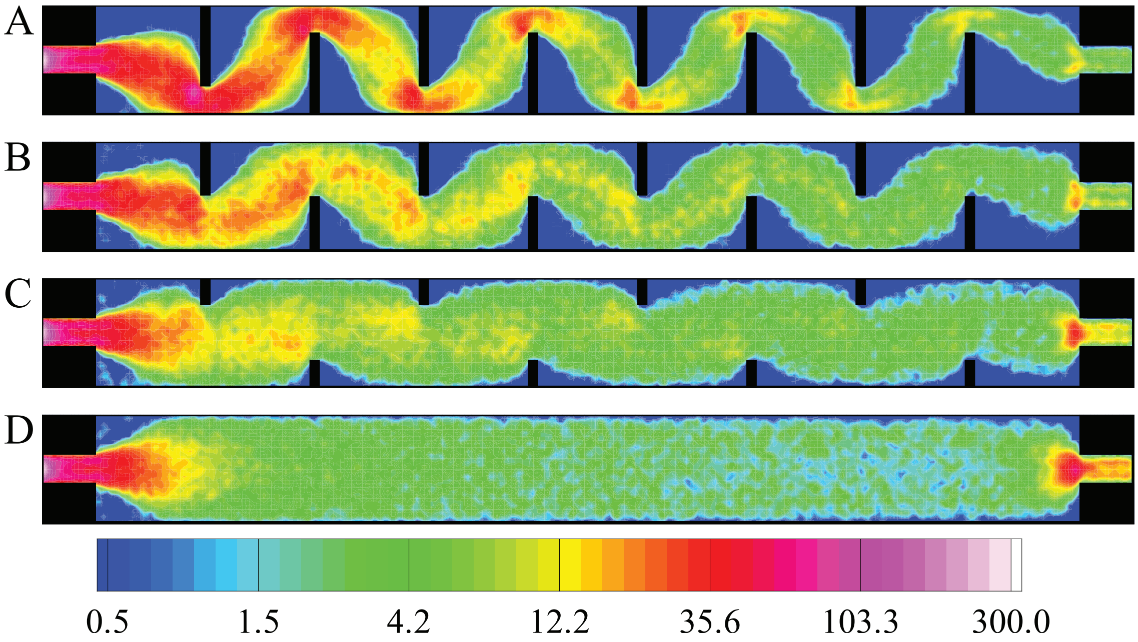

Figure 4.18: Aggregation rate at steady state in baffle reactors from Figure 4.17. Color bar is in units of aggregation events per unit area time.

reactor geometries in the presence of competing objectives.

4.8 Conclusions

The convective LKMC method has been extended for simulating particle aggregation in the presence of complex fluid flow. A contact time model was developed to account for the finite time that particles are within some distance to aggregate. The contact time model was necessary to overcome the lack of hydrodynamic interactions within this implementation of the LKMC algorithm. The contact time model accounts for the local shear rate and particle-particle contact angle and can be directly compared to the PBE. The contact time model was further analyzed in the context of platelet aggregation using regression to experimentally inferred sticking coefficients in a tubular microchannel. A

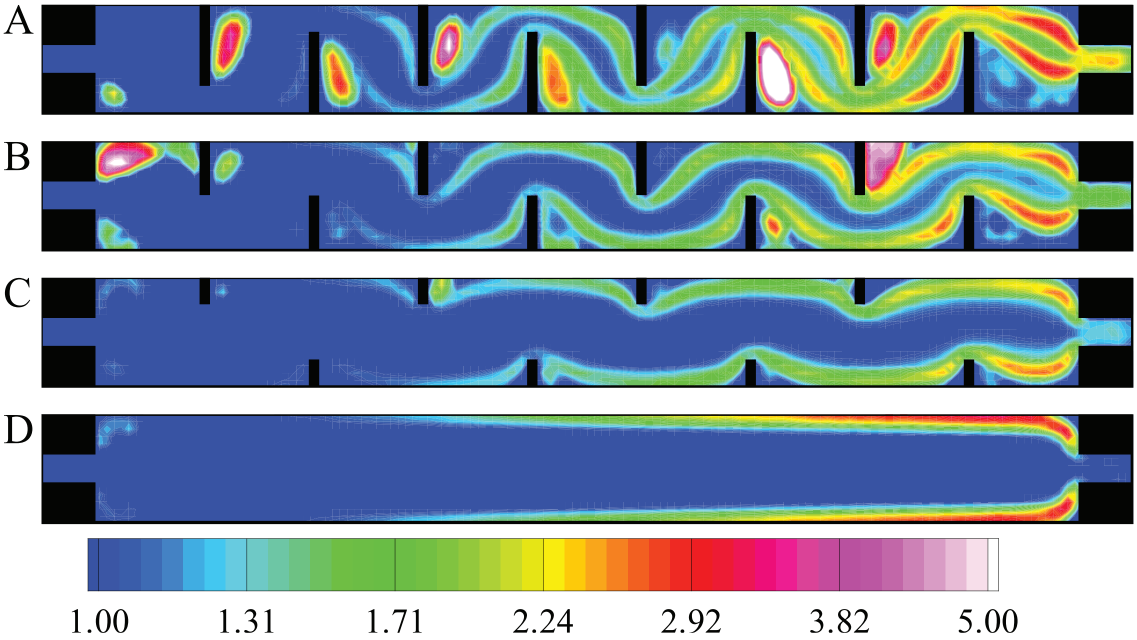

Figure 4.19: Average dimensionless particle size in baffle reactors from Figure 4.17. Color bar represents average particle size relative to monomer: $\left(R/R_0\right)^2$.

single extracted aggregation rate is able to adequately describe an experimentally inferred platelet collision efficiency over a large range of averaged shear rates within tubular flows. Moreover, the inferred aggregation rate is physiologically reasonable, which provides further evidence for the validity of the interaction model.

The LKMC model was validated using a series of simple examples that can be described with a population balance equation formulation. Although the LKMC simulations were fully able to capture the spatiotemporal evolution in all tested cases, the resolution of the particle on the lattice is an important parameter in setting the accuracy of the method. In general, coarser grids lead to an increase in numerical diffusion, which alters the physics of the aggregation process. The LKMC model was then applied to flow examples that are well beyond the scope of the PBE-based approaches. The LKMC approach was easily able to address baffled parallel-plate geometries with variable baffle heights that produce a highly heterogeneous shear-rate distribution within the domain.

Chapter 5

Multiscale prediction of patient-specific platelet deposition under flow

A cartoon representation of the biological and physical mechanisms of platelet aggregation is shown in Figure 5.1. Initial adhesion is started by collagen exposure. GPIb-IX-V on the platelet mediates transient adhesion to vWF that is bound to collagen. The main collagen receptor responsible for signaling is GPVI. Intracellular calcium concentration generally rises in response to an activating signal, and an increased level of calcium causes activation of the platelet integrins. The integrin $\alpha_2\beta_1$ mediates firm adhesion to collagen. Activated platelets, shown as shaded in Figure 5.1, release soluble platelet agonists such as ADP and TXA_2, which also cause an increase in intracellular calcium. The soluble agonists form a boundary layer in the blood flow, through which platelets from the bulk fluid are recruited to the injury site. Activated platelets also display the active fibrinogen receptor $\alpha_{2b}\beta_3$. Two activated platelets can form $\alpha_{2b}\beta_3$-fibrinogen-$\alpha_{2b}\beta_3$ bonds that allow propagation of the clot into the lumen of the vessel.

This simplified view of platelet aggregation neglects the effect of thrombin generation and the release of other platelet agonists such as epinephrine and serotonin. Although these molecules are clinically important for clotting function, a simplified representation of platelet aggregation is considered here to enable patient-specific predictions under flow. Addition of these factors is discussed in Chapter 6.

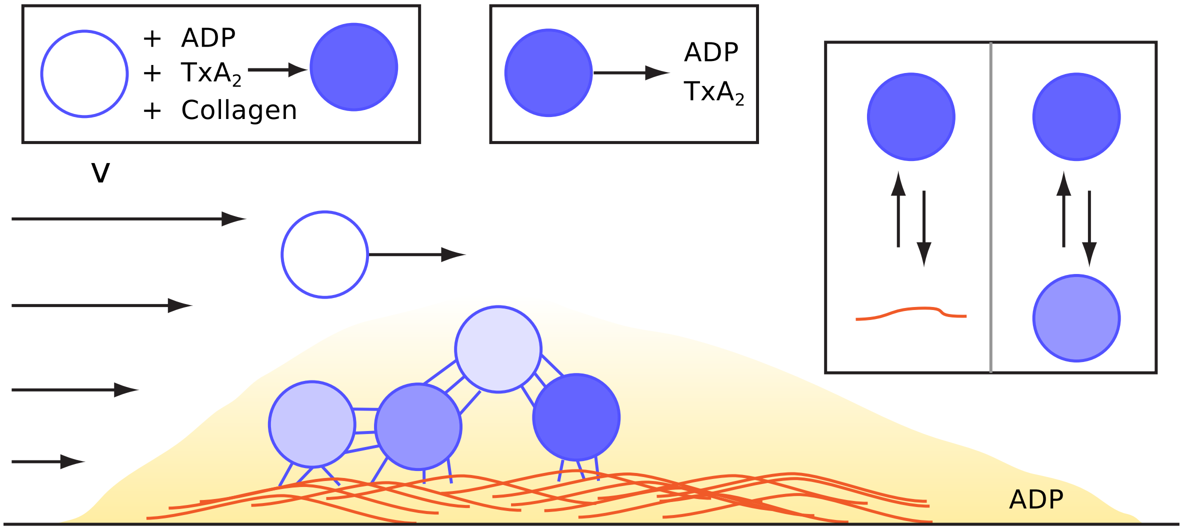

Figure 5.1: Cartoon representation of platelet aggregation.Exposure of collagen (orange fibers) starts the platelet response. Platelets bind to collagen and become activated through GPVI (color change: white to blue). Sufficiently activated platelets release soluble platelet agonists, ADP and TXA_2. The soluble agonists form a boundary layer with the fluid flow (only ADP is shown in this figure). Platelets firmly adhere to collagen through the $\alpha_2\beta_1$ integrin. A platelet-platelet bond can form through $\alpha_{2b}\beta_3$-fibrinogen-$\alpha_{2b}\beta_3$ binding.

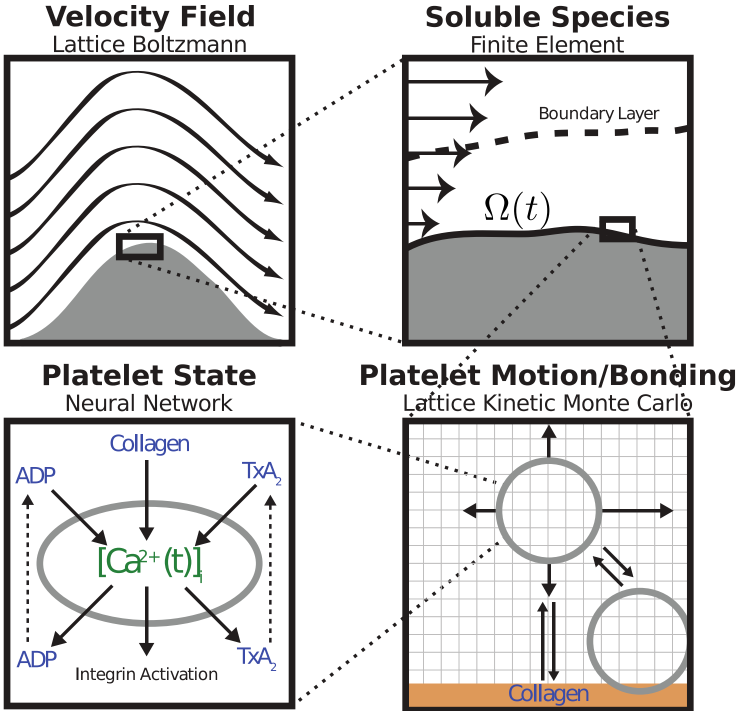

Figure 5.2: The multiscale model has four main components: fluid flow, transport of soluble species, motion and binding of platelets, and the activation state of each platelet. The fluid flow is perturbed by the growing clot and is determined using the lattice Boltzmann method. The released soluble agonists form a boundary layer in the flow, and this process is determined using the finite element method. Platelet motion and bonding are simulated with lattice kinetic Monte Carlo. Platelet activation state is estimated from the history of intracellular calcium concentration, which is determined by a neural network model.

5.1 Multiscale model

The multiscale model is assembled according to Figure 5.2. The fluid flow is perturbed as the clot grows into the lumen of the vessel (top-left). The lattice Boltzmann (LB) method is used to solve for the velocity field of the fluid. Platelets in the growing aggregate release ADP and TXA_2 into the fluid, and a boundary layer is formed with the flow (top-right). The dynamics of this process are determined with a finite element method solution of the convection-diffusion-reaction equation. Platelets move in the fluid by convection and diffusion. They also bind to the collagen surface as well as previously bound platelets (bottom-right). The motion and binding of platelets is simulated using the convective LKMC algorithm developed in Chapters 3 and 4. The level of integrin activation for each platelet is estimated through the intracellular calcium concentration (bottom-left). The intracellular calcium concentration is determined using a neural network trained on a specific patient's platelet phenotyping experiment.

5.2 Experimental methods

5.2.1 Pairwise agonist scanning and neural network training

Platelet calcium measurements and neural network training were performed by Manash Chatterjee. A 384-well agonist plate was assembled with varying concentrations of three agonists—ADP, U46619, and convulxin (CVX) at $0.1\times\mathrm{EC}_{50}$, $1\times\mathrm{EC}_{50}$, $10\times\mathrm{EC}_{50}$ levels (EC_{50} levels were 1 µM, 1 µM, and 5 nM for ADP, U46619, and CVX, respectively)—and the inhibitor iloprost at a single concentration (1 µM). Platelet rich plasma (PRP) was obtained from each of the three donors, incubated with Fluo4-NW dye, and assembled onto a 384-well platelet plate. Pairwise combinations of agonists and inhibitors were pipetted from the agonist plate onto the platelet plate and fluorescence was measured to assess calcium mobilization. This procedure was named pairwise agonist scanning (PAS).

A neural network (NN) was trained to predict platelet calcium concentration for any agonist dose and combination. The structure of the NN is given in more detail in Section 5.3.3. The training set (experimental data) consisted of concentrations of the 4 agonists or inhibitors (ADP, U46619, CVX, and iloprost) input to each well and corresponding measured calcium transient at each of the 74 conditions. The structure of the NARX (Nonlinear AutoRegressive network with eXogenous inputs) model had 2 processing layers with 8 and 4 nodes and output feedback over 128 s to each layer. The hyperbolic tangent transfer function was used in all processing layers, and a linear transfer function was used in the output layer. Training was performed using Levenberg-Marquardt backpropagation until the performance of the model (mean squared error) was $\approx 1 \times 10^{-5}$. To prevent over-fitting, 10% of the experimental data was excluded from the training set, and the weights and biases were adjusted only as long as the error decreased in this testing-set in addition to continual decrease in training-set error. A unique NN was trained for each donor's PAS experiment and was input into the multiscale model.

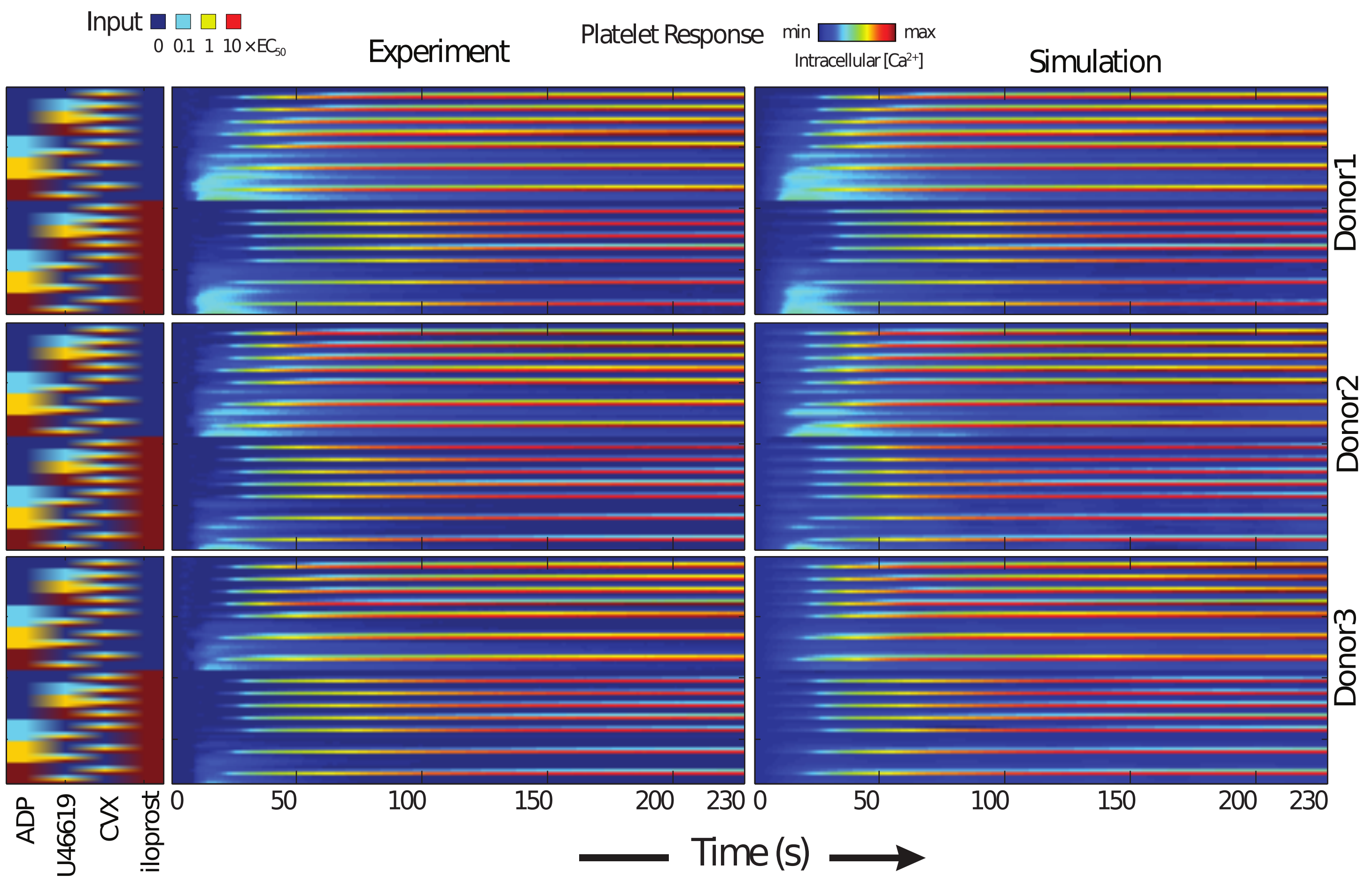

Figure 5.3: Pairwise agonist scanning for 3 donors. Calcium traces were measured in the presence of low, medium, and high doses of ADP, U46619, convulxin (CVX) in the presence or absence of iloprost and simulated by the neural network (NN).

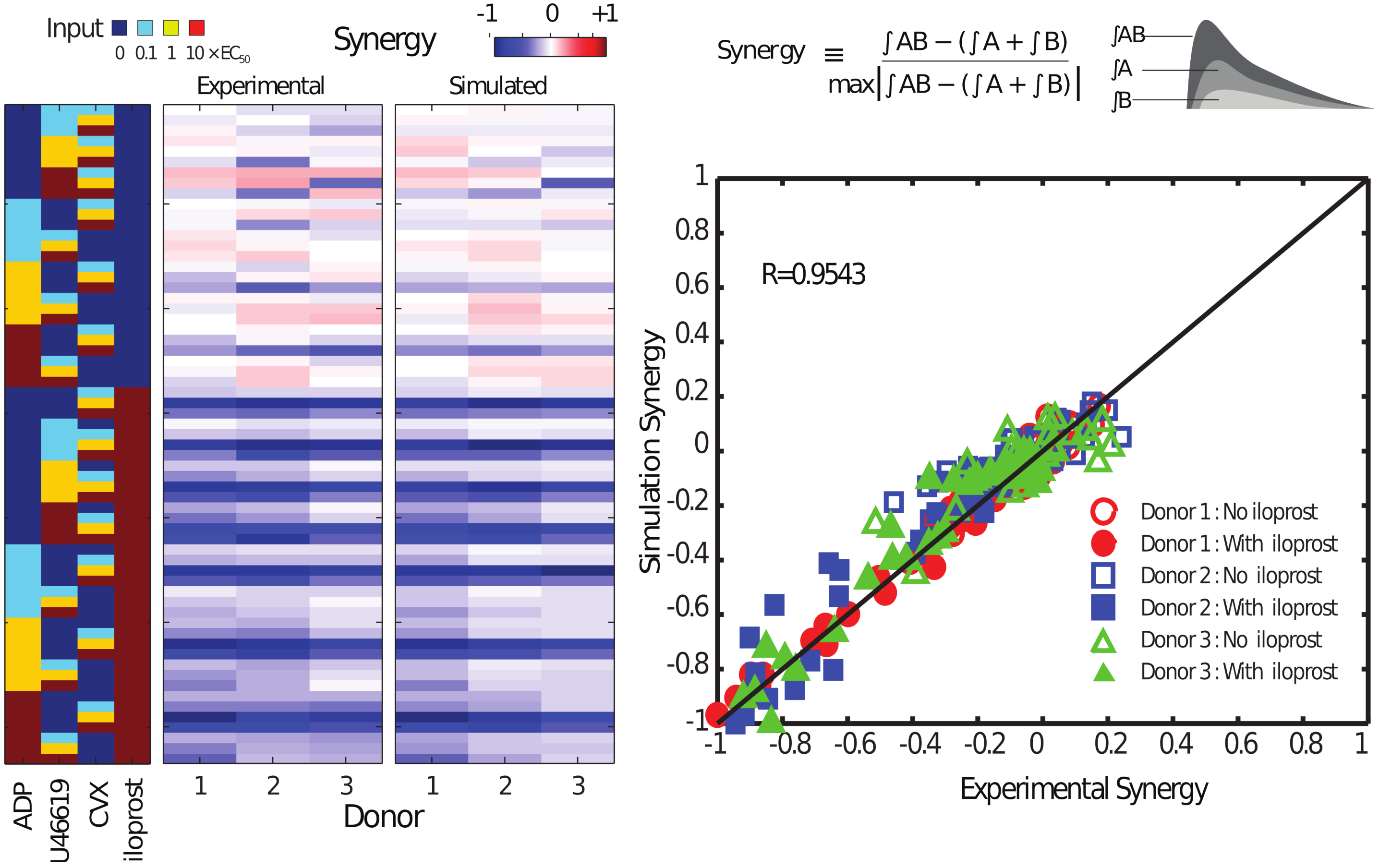

Figure 5.4: The normalized synergy parameters ($-1/ \leq S \leq 1$) for all measured pairs (± iloprost) were calculated for each donor as well as for the donor-specific NN-simulated calcium responses under identical conditions (left). Measured and NN-simulated synergy values were highly correlated indicating successful training of the NN models (right).

The trained NN accurately modeled the calcium responses within 5 % at all times. The measured synergies for 63 conditions, containing two or three inputs (two agonists with or without iloprost), provide a synergy vector, which is a measurement of an individual's phenotype. The synergy score for a condition with two agonists, A and B, is defined as

$$S_{AB} = \frac{\int AB - \left(\int A + \int B\right)}{\max\left|\int A + \int B\right|}, \tag{5.1}$$

where $\int A$ is the integral of the intracellular calcium concentration minus baseline for a condition with agonist A, i.e. $\int A = \int \left([\mathrm{Ca}^{2+}]_A(t') - [\mathrm{Ca}^{2+}]_0\right) \mathrm{d}t'$. The synergy vector is a unique and repeatable fingerprint of the individual [67]. The NN training resulted in accurate prediction of this measured synergy vector for each donor with the synergy scores highly correlated between experiment and simulation. A summary of the experimental data and NN training for 3 donors is shown in Figures 5.3 and 5.4.

5.2.2 Microfluidic models of platelet aggregation

The microfluidic experiments were performed by Tom Colace. In brief, a microfluidic channel with cross sectional dimensions of 250 µm wide and 60 µm high was laid perpendicular to a strip of patterned equine collagen type 1, 250 µm wide. Whole PPACK-treated blood was perfused over the collagen strip at a constant flow rate using a syringe pump, and the platelet density on the collagen patch was measured by a fluorescent anti-CD41 antibody (Alexafluor 647-conjugated anti-CD41). Blood was treated with 3 types of treatment: COX-1 inhibition (aspirin and indomethacin), P2Y$_1$ inhibition (MRS-2179), and IP receptor stimulation (iloprost). Fluorescence was measured for 500 s for 8 channels simultaneously on a single device. Multiple devices were run from a single donor's blood draw to obtain a large number of repeats.

5.3 Multiscale model methods

5.3.1 Model domain and grid structures

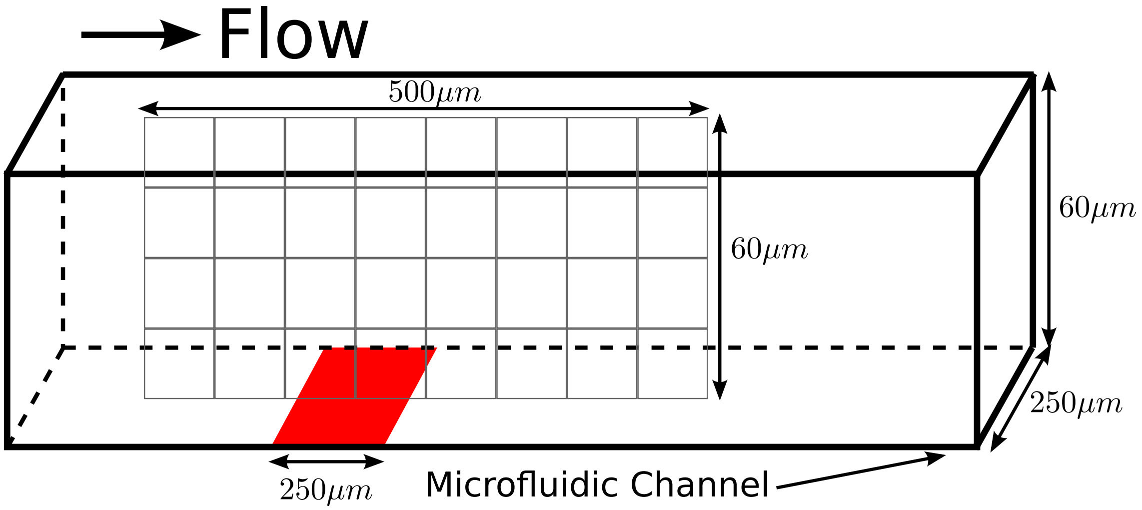

Figure 5.5: The multiscale model domain is a slice from the center of a microfluidic channel (cross-sectional dimensions: 250 µm×60 µm). The multiscale model domain is 500 µm long and 60 µm high.

As shown in Figure 5.5 the domain of the multiscale model is taken as a two-dimensional slice of the microfluidic channel. The length of the domain in this work is 500 µm, and the height is 60 µm. The collagen patch (250 µm long) starts 100 µm from the inlet and ends 150 µm from the outlet. The slice is conceptually taken in the center of the channel in the third dimension (125 µm from each wall).

For LKMC, a uniformly discretized grid with lattice spacing, $h_{\text{LKMC}} = 0.5\,\mu\text{m}$, was chosen so that individual platelets would be resolved by multiple lattice sites (Figure 5.6). Each platelet of radius, $R = 1.5\,\mu\text{m}$ [126], was centered on a lattice site and occupied all

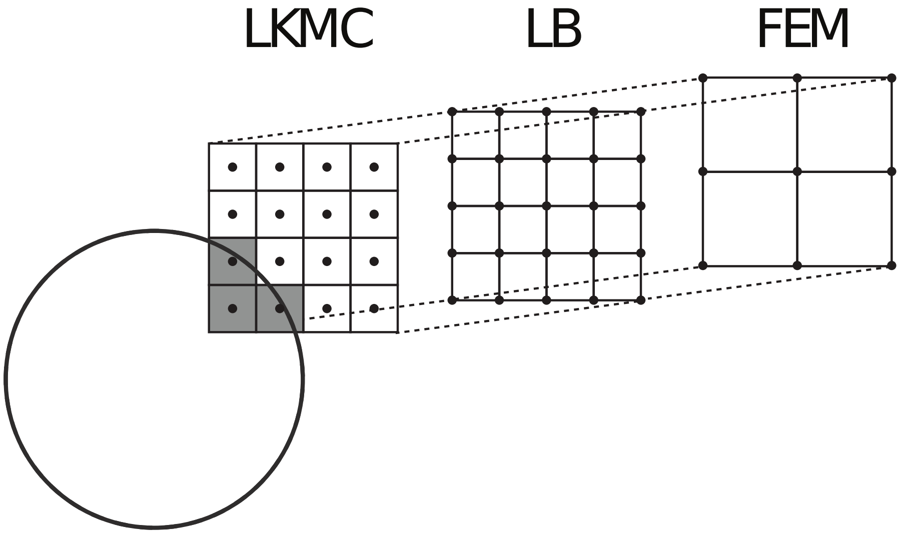

Figure 5.6: Each platelet (circle) is resolved by multiple lattice sites on the LKMC grid with lattice spacing h_{LKMC}. The LB grid has the same lattice spacing as LKMC, $h_{\mathrm{LB}} = h_{\mathrm{LKMC}}$ but is offset by half a lattice space. Each LKMC node is at the center of 4 LB lattice nodes and vice versa. The FEM grid nodes are coincident with the LB grid nodes every 2 LB lattice spaces, $h_{\mathrm{FEM}} = 2h_{\mathrm{LB}}$. Multiple LKMC and LB nodes and FEM elements resolve each platelet. A single FEM element may contain parts of multiple platelets and fluid at the same time.

lattice sites within the platelet radius. For LB, a uniformly discretized grid with the same lattice spacing as LKMC, $h_{\mathrm{LB}} = h_{\mathrm{LKMC}} = 0.5\,\mu\mathrm{m}$, was chosen, and the lattice nodes were offset from the LKMC nodes by half a lattice spacing. For FEM, a uniformly discretized grid with a coarser lattice spacing, $h_{\mathrm{FEM}} = 2h_{\mathrm{LB}} = 1\,\mu\mathrm{m}$, was aligned with the LB grid at every 2 LB nodes. A single platelet was described by multiple lattice nodes on the LKMC and LB grids and multiple elements on the FEM grid. A single FEM element was large enough to contain parts of multiple platelets and fluid at the same time. The significance of the different levels of grid resolution is discussed within each method.

5.3.2 LKMC model

The input into kinetic Monte Carlo is the rate for all possible events including convection, diffusion, binding, and unbinding events. The rate of motion of a single platelet on the lattice by diffusion in any of the 4 lattice directions is given by

$$\Gamma_D = \frac{D}{h_{\mathrm{LKMC}}^2}, \tag{5.2}$$

where D is the effective platelet diffusivity due to Brownian and red blood cell (RBC) motion. The motion of RBCs augments the apparent platelet diffusivity to $D_{\mathrm{platelet}} = 1.25 \times 10^{-7}\,\mathrm{cm}^2\,\mathrm{s}^{-1}$ [127]. For comparison, the Stokes-Einstein platelet diffusivity is $\approx 2.2 \times 10^{-9}\,\mathrm{cm}^2\,\mathrm{s}^{-1}$. An excluded volume interaction is enforced by site exclusion where the rate of any event that causes particle overlap on the lattice is set to zero. Along a lattice direction, $\mathbf{e}_i$, the rate of motion of a single platelet on the lattice by convection is given by

$$\Gamma_C = \frac{\max\left(\mathbf{v} \cdot \mathbf{e}_i, 0\right)}{h_{\mathrm{LKMC}}}, \tag{5.3}$$

where the velocity of the platelet is taken as the area-average of the local fluid velocity, $\mathbf{v}$.

RBC motion, besides augmenting the apparent diffusivity of platelets, creates an inhomogeneous radial platelet distribution, where the platelet concentration is highest near the walls. Yeh, Calvez, and Eckstein experimentally measured the radial concentration profile of platelets in whole blood [128]. They modeled the RBC effect as an effective radial platelet drift velocity, which was derived from the measured concentration profile. The drift velocity in the two dimensional channel used here is shown in Figure 5.7, where a negative drift velocity is towards the wall. The resulting concentration profile

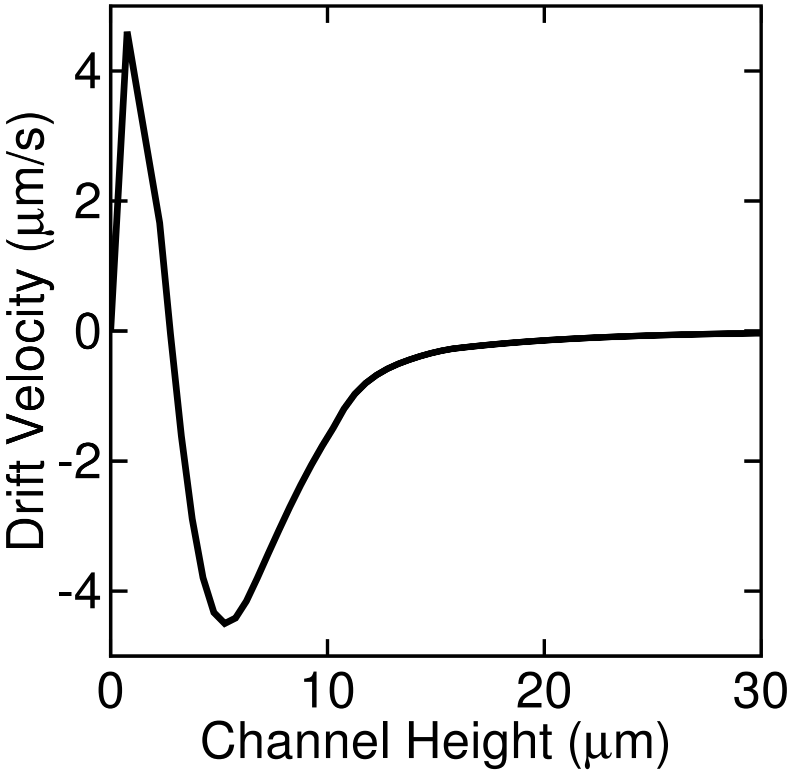

Figure 5.7: Platelet drift velocity from Yeh, Calvez, and Eckstein due to RBC motion [128]. The x-axis starts at the wall, so a positive height points into the channel. A positive velocity points away from the wall, so the negative velocity within the center of the channel pushes platelets towards the wall.

for a 60 µm channel is shown in Figure 5.8. The maximum radial drift is approximately 4 µm s^{-1}, which results in a maximum platelet concentration of 3.75 times the bulk, $C_{\text{bulk}} = 1.5 \times 10^5$ platelet µL^{-1}. The concentration of platelets at the wall is slightly less than the overall maximum and is approximately 3 times the bulk. Thus, the total effect of RBC motion is an increased concentration of platelets near the wall and increased platelet diffusivity.

During a move event, the chosen platelet is moved one lattice space in the direction

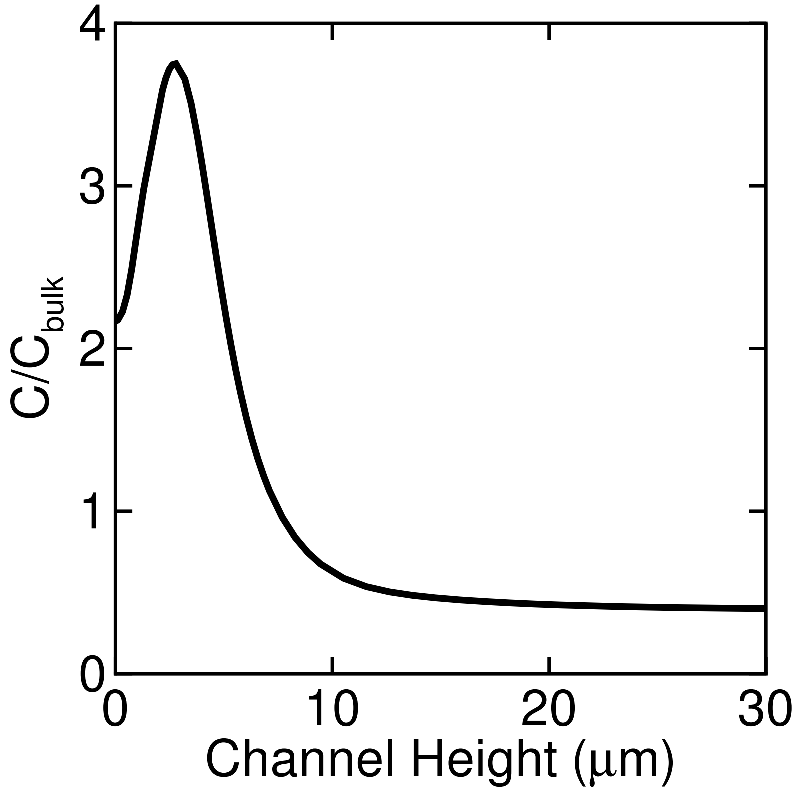

Figure 5.8: Platelet concentration profile resulting from the drift velocity in Figure 5.7. The bulk concentration of platelets is given by $C_{\text{bulk}} = 1.5 \times 10^5$ platelet µL^{-1}.

chosen. The rates of all local platelets (other platelets that are nearest neighbors before or after the event) and the current platelet are updated after the event is executed. Particle blocking on the lattice is handled similar to Chapters 3 and 4, whereby convective rates of blocked particles are passed in the direction of flow. Flipping rates as described in Chapter 4 are also implemented. A platelet that is bound to collagen or another platelet is defined to be immobile, and the motion rates for this platelet are set to 0.

Binding rates are dependent on the extent of inside-out signaling for $\alpha_2\beta_1$ and $\alpha_{2b}\beta_3$. The internal activation state, $\xi_i(t)$, of the ith platelet was estimated from the integral of the intracellular calcium concentration above the baseline concentration,

$$\xi_i(t) = \int_{-\infty}^{t} \left(\left[\mathrm{Ca}^{2+}\right]_i (t') - \left[\mathrm{Ca}^{2+}\right]_0 \right) \mathrm{d}t', \tag{5.4}$$

where $\left[\mathrm{Ca}^{2+}\right]_0$ was set to 100 nM [129], and the time-dependent calcium concentration was computed using the donor-specific NN, which accounts for exposure to collagen, ADP, and TXA_2 along the platelet trajectory. The integrated calcium concentration, $\xi_i(t)$, for each platelet was then used to define a time-dependent extent of inside-out signaling, $F(\xi_i)$, for $\alpha_2\beta_1$ and $\alpha_{2b}\beta_3$ integrin activation,

$$F(\xi_i) = \alpha + (1 - \alpha)\frac{\xi_i^n}{\xi_i^n + \xi_{50}^n}, \tag{5.5}$$

where n controls the sharpness of the response, and ξ_{50} is the internal activation state required for 50% activation. In the present work, the values of $n = 0.75$ and $\xi_{50} = 9\,\mu\mathrm{M\,s}$ were employed for both $\alpha_2\beta_1$ and $\alpha_{2b}\beta_3$ integrin activation. Activation of calDAG-GEFI downstream of calcium signaling and talin-1 binding causes a conformational change in integrins to a high affinity state [130]. $\alpha_2\beta_1$ and $\alpha_{2b}\beta_3$ are both activated through this pathway, so it is expected that the activation dynamics will be similar. However, the quantity of receptors and the affinity of the receptors for their ligands may differ. The quantity α represents the basal level of integrin activation and was set to 0.001 in all simulations so that $0.001 \leq F \leq 1$.

The overall rate of attachment of a platelet to collagen is defined by

$$\Gamma_{\mathrm{att}}^{\mathrm{collagen}} = k_{\mathrm{att}}^{\mathrm{collagen}} F(\xi_i), \tag{5.6}$$

where $k_{\text{att}}^{\text{collagen}}$ is the attachment rate of a fully activated platelet ($F = 1$) and accounts for receptor and ligand copy numbers, single bond kinetics, and the effects of von Willebrand Factor. The attachment rate to collagen ranges from $\alpha k_{\text{att}}^{\text{collagen}}$ ($F = 0$) to $k_{\text{att}}^{\text{collagen}}$ ($F = 1$). Similarly, the rate of attachment between two platelets via fibrinogen, $\Gamma_{\text{att}}^{\text{fibrinogen}}$, depends on the activation states of both platelets. To model the two-body interaction, the rate of binding between platelets i and j is given by the geometric mean of integrin activation,

$$\Gamma_{\text{att}}^{\text{fibrinogen}} = k_{\text{att}}^{\text{fibrinogen}} \sqrt{F(\xi_i)F(\xi_j)}. \tag{5.7}$$

The detachment rate of platelets from collagen, $\Gamma_{\text{det}}^{\text{collagen}}$, is modeled using the Bell exponential [131] to describe force-dependent breakage of receptor-ligand bonds,

$$\Gamma_{\text{det}}^{\text{collagen}} = k_{\text{det}}^{\text{collagen}} F(\xi_i)^{-1} \exp\left(\frac{\gamma_i}{\gamma_c}\right), \tag{5.8}$$

where $F(\xi_i)^{-1}$ accounts for the increased number of bonds that must be broken as the cell activates, γ_i is the local shear rate around platelet i, and γ_c is the characteristic shear rate required to initiate accelerated bond breakage. The detachment rate between platelets bound via fibrinogen is similarly given by

$$\Gamma_{\text{det}}^{\text{fibrinogen}} = k_{\text{det}}^{\text{fibrinogen}} \left(F(\xi_i)F(\xi_j)\right)^{-1/2} \exp\left(\frac{\gamma_i}{\gamma_c}\right). \tag{5.9}$$

5.3.3 NN model

For a cell with local agonist concentrations,

$$c = \left([\text{ADP}], [\text{U46619}], [\text{CVX}], [\text{iloprost}]\right), \tag{5.10}$$

the NN predicts the intracellular calcium concentration, $\left[\mathrm{Ca}^{2+}\right]$. U46619 is the experimental analog of TXA_2. U46619 and TXA_2 may have separate affinities for TP, and this effect is captured by calculating an effective U46619 concentration as

$$[\mathrm{U46619}] = \theta\,[\mathrm{TXA}_2]\,. \tag{5.11}$$

θ modulates the ratio of potency between TXA_2 and U46619, where a value of $\theta > 1$ represents more potent TXA_2. The platelet calcium measurements were performed with convulxin (CVX) instead of collagen, so the effective potency of the collagen patch is determined by the CVX concentration, which is an input into the simulation. The agonist concentrations are mapped to the interval $[-1, 1]$ from a log scale, where the concentrations at $[0.01\times\mathrm{EC}_{50}, 0.1\times\mathrm{EC}_{50}, 1\times\mathrm{EC}_{50}, 1\times\mathrm{EC}_{50}]$ are mapped to $[-1, -1/3, 1/3, 1]$. Concentrations larger than $10\times\mathrm{EC}_{50}$ are mapped to the maximum, 1, and concentrations smaller than $0.01\times\mathrm{EC}_{50}$ are mapped to the minimum, -1. The EC_{50}values are 1 µM for ADP and 1 µM for U46619 [67]. The $\mathrm{EC}_{50}$of CVX is 5 nM [67]. The NN input for iloprost was either -1 for platelets not treated with iloprost or 1 for platelets treated with iloprost. The local concentrations of ADP and TXA_2 are determined through the average concentration over the platelet area.

The output of the NN model must be mapped to intracellular calcium concentration for input into the platelet bonding model (calculation of ξ in Equation 5.4). The output of the NN is linearly mapped from the interval $[-1, 1]$ to [0.1 µM, 1 µM], where 0.1 µM is the resting level of intracellular calcium and 1 µM represents maximal calcium mobilization [129].

Figure 5.9 shows the structure of the NN with connectivity between the layers. The mapped inputs, $c^{(4\times1)}$, are fed into each node of the first layer of the NN with weights

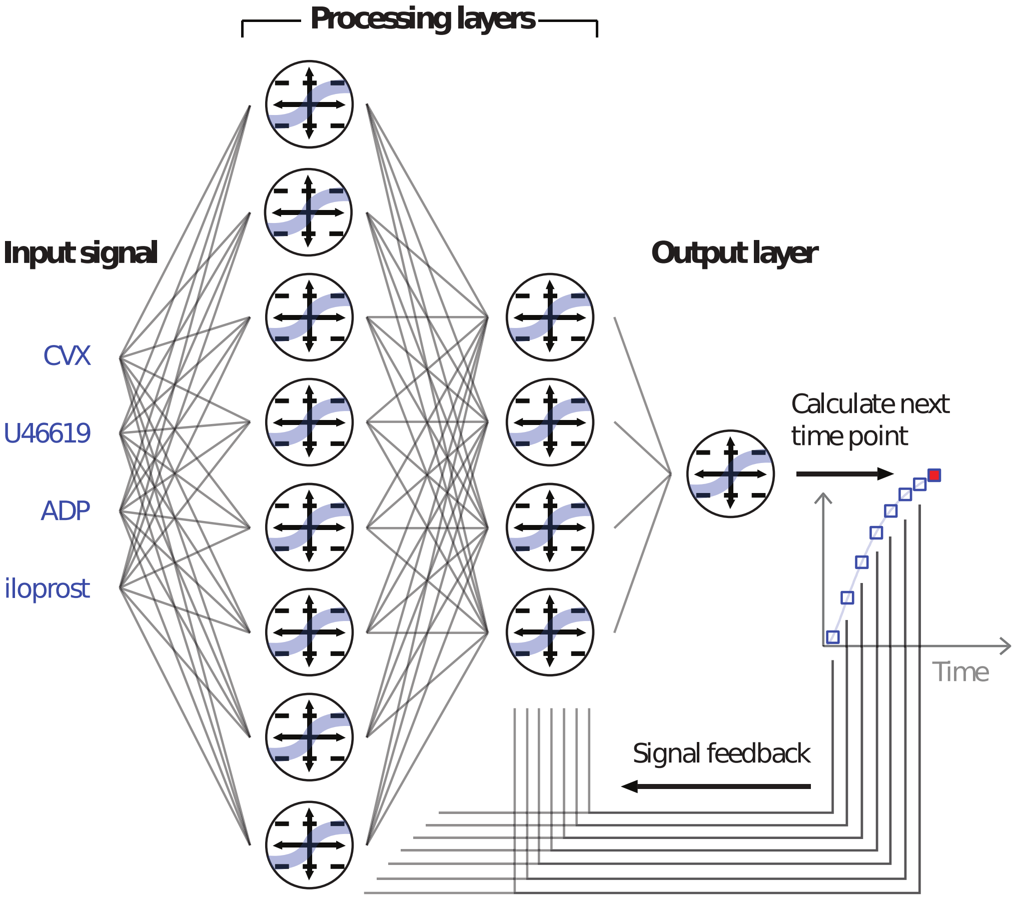

Figure 5.9: Neural network with 4 inputs (ADP, U46619, CVX, and iloprost) and 1 time-dependent output (intracellular calcium concentration) with 2 processing layers (8 and 4 nodes) and output feedback into the processing layers. The transfer function at each processing layer node is the hyperbolic tangent function.

$IW^{(8\times4)}$. The time history of the NN output, $z^{(8\times1)}$, at times $[t-1, t-2, t-4, t-8, t-16, t-32, t-64, t-128]$ s, where t is the time of the next solution ($t-1$ is the time of the current solution), is weighted with $A_1^{(8\times8)}$ and is also fed to the first layer. The sum of the weighted inputs, the weighted time history, and a constant bias at each node, $b_1^{(8\times1)}$, is transformed with the hyperbolic tangent function, tanh, and the outputs of all nodes in the first layer are fed into each node of the second layer of the NN with weights

$LW_1^{(4\times8)}$. The time history is also fed back to the second layer with weights $A_2^{(4\times8)}$. In the second layer, the weighted inputs, time history, and a constant bias, $b_2^{(4\times1)}$, are again transformed with the hyperbolic tangent function, and the output of each node is fed to the output layer with weights $LW_2^{(1\times4)}$. The sum of the weighted inputs and constant bias, $b_3^{(1\times1)}$, are linearly combined to obtain the solution at time t. The output from the first layer is given by

$$l_1^{(8\times1)} = f\left(IW^{(8\times4)}c^{(4\times1)} + A_1^{(8\times8)}z^{(8\times1)} + b_1^{(8\times1)}\right)^{(8\times1)}, \tag{5.12}$$

where $f() = \tanh()$. The output from the second layer is given by

$$l_2^{(4\times1)} = f\left(LW_1^{(4\times8)}l_1^{(8\times1)} + A_2^{(4\times8)}z^{(8\times1)} + b_2^{(4\times1)}\right)^{(4\times1)}. \tag{5.13}$$

The output from the NN is

$$y(t)^{(1\times1)} = LW_2^{(1\times4)}l_2^{(4\times1)} + b_3^{(1\times1)} \tag{5.14}$$

The superscripts in Equations 5.12-5.14 represent the dimensionality of each matrix or vector. The solution of a NN is simply a set of matrix-vector multiplications with transformation functions. The initial time history of intracellular calcium concentration of a platelet was set to 100 nM, the basal level.

The NN only solves for $[\mathrm{Ca}^{2+}]$ at integer times, but we would like to be able to resolve the intracellular calcium concentration at a finer time resolution. An interpolation-prediction scheme is used to accomplish this goal. If a solution of the NN is known at time t_1, the next solution is at time $t_2 = t_1 + 1$. For a multiscale model time, t^* where

$t_1 < t^* < t_2$, the solution at time t_2 is predicted with the current system state. The solution at time t^* is linearly interpolated from the known solution at t_1 and the predicted solution at time t_2.

5.3.4 Lattice Boltzmann model

Lattice Boltzmann (LB) solves for the velocity field around the growing platelet deposit by simulating the advection of and collisions between packets of fluid on a lattice. The lattice spacing is the same as LKMC grid ($h_{\mathrm{LB}} = h_{\mathrm{LKMC}}$), and the lattice nodes are offset from the LKMC nodes by half a lattice spacing (Figure 5.6). In two dimensions, each node has 9 types of fluid velocities that stream to its 8 nearest neighbors and itself (D2Q9 lattice). The algorithm has two main steps: collision and streaming. During a streaming step, fluid is streamed to neighboring lattice nodes, and during the collision step, fluid is relaxed to an equilibrium configuration. The process of streaming and collision effectively solves the Navier-Stokes and continuity equations [38]. The time step for streaming and collision was set as $\Delta t_{\mathrm{LB}} = 1 \times 10^{-7}\,\mathrm{s}$.

The inlet condition is fully-developed flow at a flow rate Q, and the outlet condition is a constant pressure, P_o. The two walls have no-slip boundary conditions. Bound platelets are also represented as no-slip surfaces. Since the LB grid is offset from the LKMC grid, the no-slip boundary conditions are naturally defined at the interface between the solid and liquid (Figure 5.6). Free flowing platelets are ignored in the LB model, but the hydrodynamic effect of a bound platelet on the fluid is explicitly handled in this model. Although the hydrodynamics between two free-flowing platelets are not captured, a bound platelet will perturb the trajectories of the free-flowing platelets. See Section 2.3 for more detail on LB methods.

5.3.5 Finite element model

The concentration fields, $C_j(x, y, t)$ where $j =$ ADP and TXA$_2$, are determined by finite element method (FEM) solution of the convection-diffusion-reaction equation,

$$\frac{\partial C_j}{\partial t} + \mathbf{v} \cdot \nabla C_j = D_j \nabla^2 C_j + R_j, \tag{5.15}$$

where D_j is the Brownian diffusion coefficient of ADP or TXA$_2$ (augmentation effects for small solutes in blood flow are relatively small [132]). R_j is the volumetric rate of release or generation of ADP or TXA$_2$, and $\mathbf{v}$ is the velocity field (obtained from LB). The platelet release rate of soluble species ADP and TXA$_2$ depends on the internal activation state, ξ_i. It is assumed that each platelet only releases ADP and TXA$_2$ if $\xi_i(t)$ is larger than the critical threshold, $\xi_{\text{crit}} = \xi_{50} = 9\,\mu\text{M}\,\text{s}$, where the critical threshold is defined to be the same as the ξ_{50} value for the integrin activation function. The time at which a platelet's activation state reaches ξ_{crit} is denoted as t_{release}. For $t > t_{\text{release}}$, the rate of release of ADP and TXA$_2$ is modeled by an exponential decay of the form

$$R_j(t) = \begin{cases} \frac{M_j}{\tau_j} \exp\left(-\frac{t - t_{\text{release}}}{\tau_j}\right), & \text{for } t \geq t_{\text{release}} \\ 0, & \text{for } t < t_{\text{release}} \end{cases} \tag{5.16}$$

where M_j is the total amount of releasable ADP or TXA$_2$ in a platelet and τ_j is the characteristic time constant of release. Once activated, each platelet releases 1×10^{-8} nmol [133] of ADP with a time constant of 5 s [134] and 4×10^{-10} nmol of TXA$_2$ with a time constant of 100 s [135].

In FEM, the system domain is split into discrete elements where the solution is approximated within the elements by interpolation functions. Here, bilinear interpolation functions are used, and nodes are located at the corners of the quadrilateral elements. The FEM nodes align with the LB grid every 2 LB nodes, so that each FEM element contains 4 LKMC nodes (Figure 5.6). The velocity in an element is taken as the average velocity of all LB nodes within that element. The release rate within an element is taken as the area-weighted release rate of all platelets within the element. For example, if an element contains 10% of a platelet's area, the generation rate within that element is 10% of that platelet's release rate (Equation 5.16). The location of platelets are only used to determine the generation rate in Equation 5.15, R_j, although the velocity field, which is obtained from LB, depends on the location of the bound platelets. The soluble species can be transported through platelets as if they were stagnant fluid. The weak form of the original PDE is obtained by weighting each term with the interpolation functions and integrating over each element, i.e.

$$\int_{\Omega} \phi_i \left(\frac{\partial C_j}{\partial t} + \mathbf{v} \cdot \nabla C_j - D_j \nabla^2 C_j - R_j \right) = 0, \tag{5.17}$$

where Ω is the domain of a single element and ϕ_i is a single interpolation function within that element. The time derivative was approximated using the Crank-Nicolson scheme with a time step of $\Delta t = 1 \times 10^{-2}$ s. See Section 2.2 for more detail on FEM methods.

5.3.6 Multiscale model coupling

The flow of information between models is given in Figure 5.10. LKMC provides the position of all platelets in the domain and the bonding state of each platelet. LKMC requires the velocity field of the fluid (LB) to calculate convective rates of motion and the activation state of each platelet (NN) to determine the bonding and unbonding rates. The

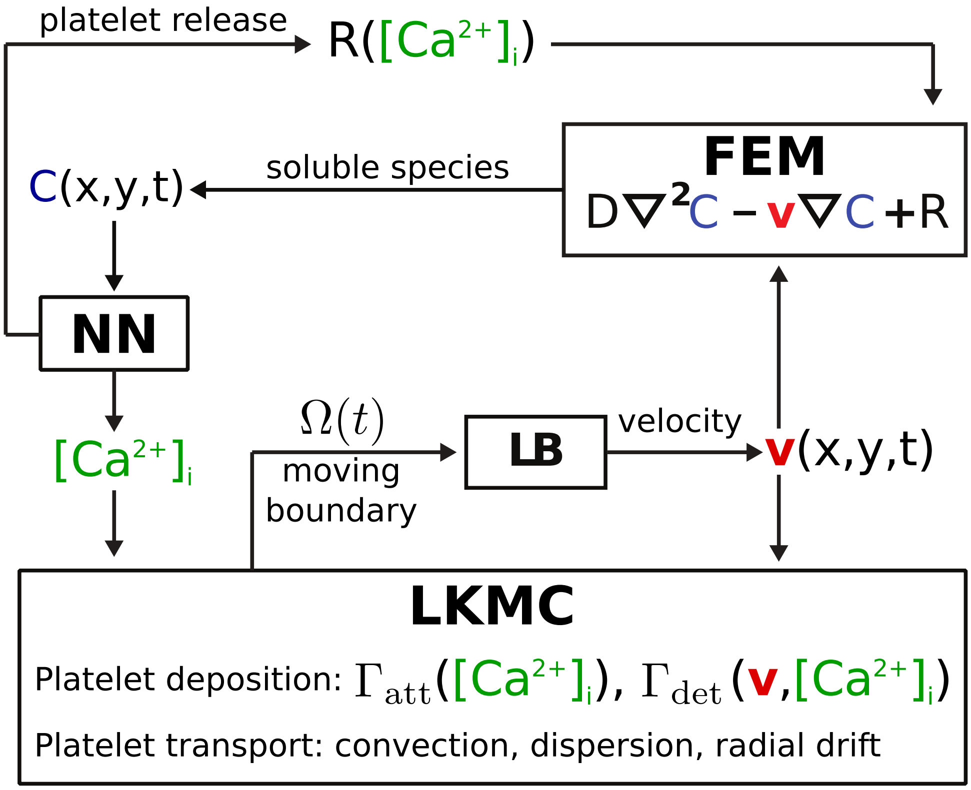

Figure 5.10: Multiscale model coupling. The LKMC method simulates platelet attachment and detachment and platelet transport. The input for the LB method is the location of all bound platelets and the output is the velocity field. The NN integrates the local agonist histories of each platelet to obtain the intracellular calcium concentration. FEM solves the reaction-diffusion-convection equation, where the platelet release rate depends on the activation states of the platelets.

NN provides the activation state of each platelet, and the input into the NN is the local concentration of platelet agonists, which requires both the platelet positions (LKMC) and the concentration field of soluble agonists (FEM). The LB method provides the velocity field and requires the location of all bonded platelets (LKMC) for the location of the no-slip surfaces. FEM provides the concentration field and requires the release rate of platelets, which depends on the location of platelets (LKMC) and the activation states (NN), and the velocity field (LB).

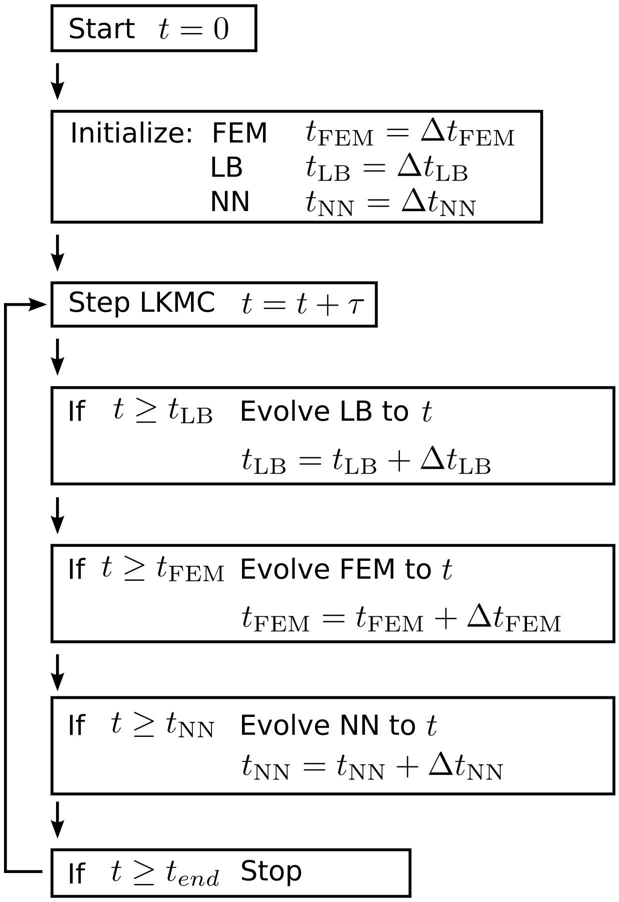

Figure 5.11: Multiscale model time stepping. Δt_i for each method ($i = \mathrm{FEM}, \mathrm{LB}, \mathrm{orNN}$) is the time step at which information is exchanged. t_i for each method is the next time at which information is exchanged. t is the overall system time, which is kept by LKMC, and τ is the time step for a single LKMC move.

The coupling of the individual models only occurred at specified time intervals: $\Delta t_{\mathrm{LB}} = 5 \times 10^{-3}\,\mathrm{s}$, $\Delta t_{\mathrm{FEM}} = 1 \times 10^{-2}\,\mathrm{s}$, and $\Delta t_{\mathrm{NN}} = 1 \times 10^{-2}\,\mathrm{s}$. LKMC always exchanged information during updates, so in this case, LKMC simply had a coupling time of $\Delta t_{\mathrm{LKMC}} = 5 \times 10^{-3}\,\mathrm{s}$. At the start of the simulation ($t = 0\,\mathrm{s}$) LKMC, LB, FEM, and the NN were all specified by the initial condition for each method. The LKMC method was stepped forward in time until the first coupling time was reached ($t = 5 \times 10^{-3}\,\mathrm{s}$), and then the appropriate methods were stepped forward in time with the current system state. During the first update, LB received the current configuration of bound platelets from LKMC, and then LB was simulated until the system time current system time ($t_{\mathrm{LKMC}} = 5 \times 10^{-3}\,\mathrm{s}$). Then, the LKMC method with an updated velocity field resumed stepping forward in time until the next coupling time ($t = 1 \times 10^{-2}\,\mathrm{s}$) occurred. During this update all models share information: LKMC updated the positions of all platelets and the bound states of all platelets in FEM, LB, and NN; LB updated the velocity field in LKMC and FEM; FEM updated the concentration field in NN; and NN updated the activation state in FEM and LKMC. This process repeats until the end of the simulation time (see Figure 5.11).

The time scale for velocity field relaxation was generally $<< 10^{-3}\,\mathrm{s}$, so the velocity field reached a steady state in LB significantly before reaching the current system time. To gain computational efficiency, LB was only simulated until steady-state was achieved as determined by convergence of the velocity field. At the next coupling time, the boundary condition only changed if a platelet underwent a bonding or unbonding event. If this occurred, LB was again simulated until steady-state. If not, the steady-state solution from the previous step was kept, and no LB simulation was needed. In this way, the velocity field was only updated if a platelet had a bonding or nonbonding event.

5.4 Results

5.4.1 Model parameters

The multiscale model contains 21 parameters (Table 5.1) held constant in all simulations. Some parameters are known quantities derived from experiment including C_{platelet}, ρ_{blood}, μ_{blood}, R_{platelet}, D_{platelet}, D_{ADP}, D_{TXA2}, M_{ADP}, M_{TXA2}, τ_{ADP}, and τ_{TXA2}. C_{CVX} is the potency of the collagen surface with respect to the agonist used in Pairwise Agonist Scanning (PAS), CVX. The effective surface concentration of CVX depends on the type of collagen used as well as surface density. θ is the relative potency of TXA_2 to U46619, which is a TXA_2 analog used in PAS. The effective concentration of U46619 was defined as $[\text{U46619}] = \theta[\text{TXA}_2]$. A value of $\theta > 1$ represents the situation where TXA_2 has a higher affinity for TP. The remaining parameters (n, ξ_{50}, $k_{\text{att}}^{\text{collagen}}$, $k_{\text{det}}^{\text{collagen}}$,$k_{\text{att}}^{\text{fibrinogen}}$, $k_{\text{det}}^{\text{fibrinogen}}$) were constrained using the temporal evolution of the platelet density for several drug conditions (control, indomethacin, and iloprost) using one donor (Donor 1) (Section 5.4.3).

Table 5.1: Parameters for multiscale model

Symbol	**Name**	**Value**	**Ref./Comment**
C_{platelet}	Bulk number density of platelets	$1.5 \times 10^5\,\mathrm{platelet}\,\mathrm{\mu L}^{-1}$	Ref. [136]
ρ_{blood}	Density of blood	$1\,\mathrm{g}\,\mathrm{cm}^{-3}$	Ref. [137]
μ_{blood}	Viscosity of blood	$0.03\,\mathrm{g}\,\mathrm{cm}^{-2}$	Ref. [138]
R_{platelet}	Radius of platelet	$1.5 \times 10^{-4}\,\mathrm{cm}$	Ref. [126]
D_{platelet}	Diffusion (dispersion) coefficient of platelet	$1.25 \times 10^{-7}\,\mathrm{cm}^2\,\mathrm{s}^{-1}$	Ref. [127]
D_{ADP}	Diffusion (dispersion) coefficient of ADP	$2.37 \times 10^{-6}\,\mathrm{cm}^2\,\mathrm{s}^{-1}$	Ref. [21]
D_{TXA2}	Diffusion (dispersion) coefficient of TXA_2	$2.14 \times 10^{-6}\,\mathrm{cm}^2\,\mathrm{s}^{-1}$	Ref. [21]
M_{ADP}	Total amount of releasable ADP	$1 \times 10^{-8}\,\mathrm{nmol}\,\mathrm{platelet}^{-1}$	Ref. [133]
M_{TXA2}	Total amount of TXA_2 generated	$4 \times 10^{-10}\,\mathrm{nmol}\,\mathrm{platelet}^{-1}$	Ref. [135]
τ_{ADP}	Release time constant for ADP	$5\,\mathrm{s}$	Ref. [134]
τ_{TXA2}	Release time constant for TXA_2	$100\,\mathrm{s}$	Ref. [135]
C_{CVX}	Effective concentration of collagen	$0.5 \times \mathrm{EC}_{50}$ of CVX	soluble vs. surface ligand
θ	Relative potency of TXA_2/U46619	15	Relative binding affinity for TP receptor
α	Resting level of integrin activation	0.001	1 active integrin per 1000 on platelet surface

Continued on next page

Table 5.1 – continued from previous page

Symbol	**Name**	**Value**	**Ref./Comment**
n	Sharpness of activation function	0.75	Expected value: $0.5 < n < 2$
ξ_{50}	Critical value for 50% activation and platelet release	$9\,\mu\mathrm{M\,s}$	Strong calcium mobilization ($1\,\mu\mathrm{M}$ for $10\,\mathrm{s}$)
$k_{\mathrm{att}}^{\mathrm{collagen}}$	Attachment rate constant for collagen binding	$1000\,\mathrm{s}^{-1}$	Includes vWF/GPIb
$k_{\mathrm{att}}^{\mathrm{fibrinogen}}$	Attachment rate constant for fibrinogen-mediated binding	$50\,\mathrm{s}^{-1}$	
$k_{\mathrm{det}}^{\mathrm{collagen}}$	Detachment rate constant for collagen binding	$5 \times 10^{-4}\,\mathrm{s}^{-1}$	
$k_{\mathrm{det}}^{\mathrm{fibrinogen}}$	Detachment rate constant for fibrinogen-mediated binding	$5 \times 10^{-5}\,\mathrm{s}^{-1}$	
γ_{c}	Critical shear rate	$200\,\mathrm{s}^{-1}$	

5.4.2 Simulations of platelet function

Multiscale simulations predicted the density of platelets adherent to the surface, platelet activation states, the spatiotemporal dynamics of ADP and TXA_2 release, morphology of the growing aggregate, and the distribution of shear along the solid-fluid boundary. The state of a representative simulation at 500 s is shown in Figure 5.12, and more time points are shown in Appendix A. Initially, platelets only adhered to the collagen surface until the adherent platelets became sufficiently activated to release ADP and TXA_2. The released ADP and TXA_2 formed a boundary layer extending up to 10 µm from the platelet deposit, which was sufficient to recruit platelets in the near-wall region. Within the boundary layer, concentrations of up to 10 µM ADP and 0.1 µM TXA_2 were observed. Concentrations of ADP and TXA_2 and the boundary layer thickness were consistent with earlier continuum models that imposed a thrombus growth rate and geometry [21]. TXA_2 concentrations were found to be sub-physiological ($< 0.0067\,\mu\text{M}$ or $< 0.1 \times \text{EC}_{50}$) until a sufficient platelet mass accumulated at the surface after 250 s. Boundary layer ADP concentrations were within the effective dynamic range ($[0.1\,\mu\text{M}, 10\,\mu\text{M}]$ or $[0.1 \times \text{EC}_{50}, 10 \times \text{EC}_{50}]$) throughout the simulation. The ADP concentration profile had spatial and temporal fluctuations of 2 to 3 orders in magnitude, while the TXA_2 concentration profile had less than an order of magnitude of spatial fluctuations and no temporal fluctuations. Spatial fluctuations in the TXA_2 profile were created by an inhomogeneous distribution of platelet density along the surface. The strong temporal and spatial fluctuations in the concentration of ADP were predominately driven by the short release time (5 s), whereas the longer release time of TXA_2 (100 s) smoothed fluctuations. Appendix B contains representative snapshots at 500 s of the simulation for all 3 donors with the pharmacological mediators indomethacin (no TXA_2), iloprost, and MRS-2179 (no ADP).

Platelets interacting with collagen became the most activated due to the sustained calcium mobilization in collagen signaling, while platelets that were stimulated only by ADP and TXA_2 had only a transient increase in intracellular calcium. Figure 5.13 shows the internal

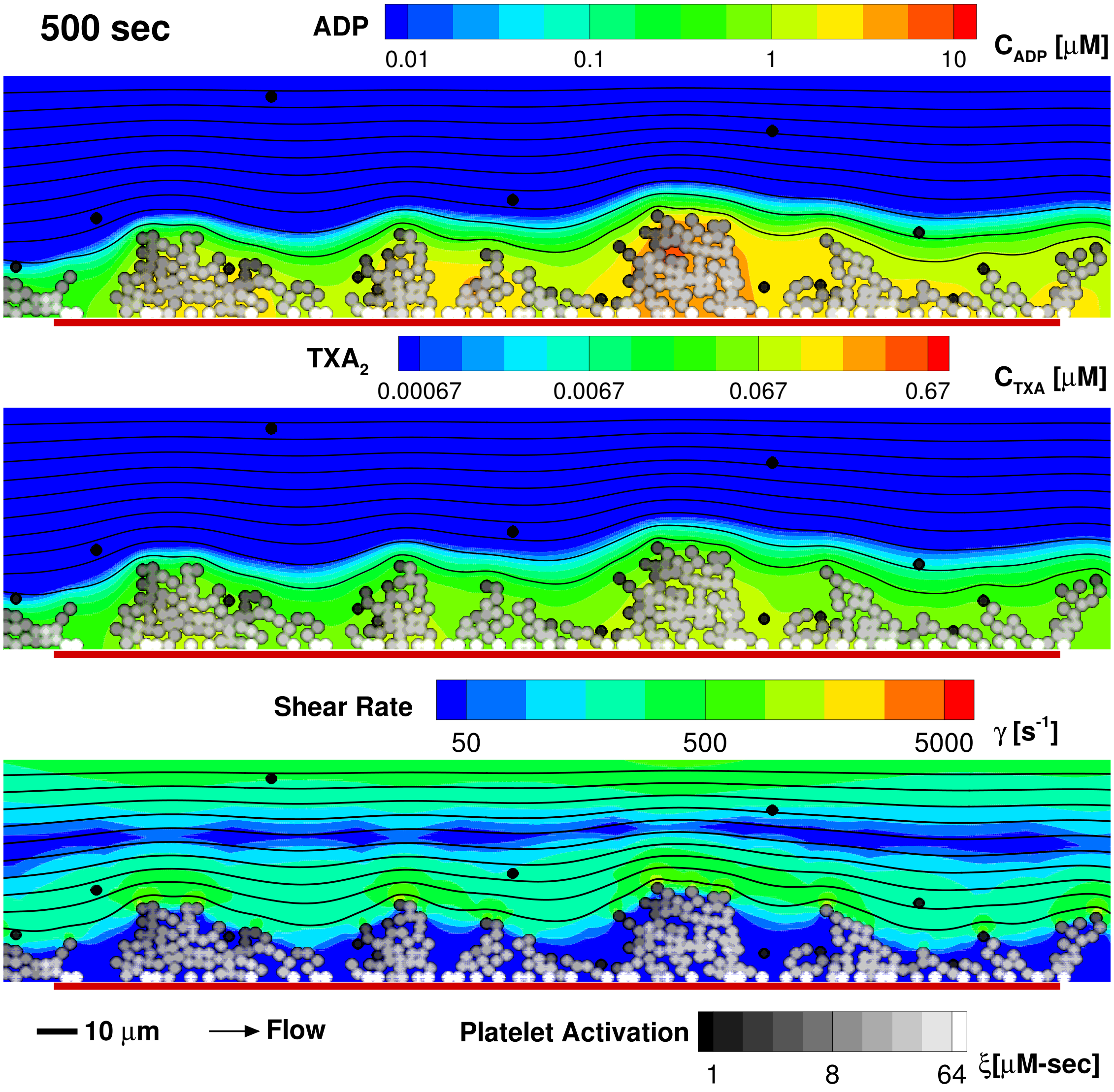

Figure 5.12: Multiscale simulation of patient-specific platelet deposition under flow for Donor 1. Platelet activation (black, unactivated; white, activated) and deposition at 500 s (inlet wall shear rate, 200 s^{-1}) for Donor 1 in the presence of ADP (top) and TXA$_2$ (middle). Flow: left to right (streamlines, black lines); surface collagen (250 μm long): red bar.

activation state of all platelets bound to the surface at 500 s. Red lines show platelets bound to collagen while blue lines show platelets bound only to other platelets. Platelets bound to collagen have a sustained rise in intracellular calcium leading to higher levels of platelet activation than platelets bound only to other platelets (stimulated only by ADP and TXA_2). The history of a single platelet that was not bound to collagen is shown in Figure 5.14. The intracellular calcium concentration shows a transient increase above baseline, 100 µM, to almost 400 nM. The internal activation state, ξ, eventually rises above ξ_{50}, but does not see the steady increase seen in cells exposed to collagen (Figure 5.13). Integrin activation reaches 70 % of maximum by the end of the simulation time. Note that the platelet was only in the domain for less than 300 s.

The platelets participating in the initial platelet-collagen interactions (< 100 s) experienced a fluid shear close to the initial wall shear rate of $200\,\mathrm{s}^{-1}$ (Figures A.1–A.2). The shear rate along the solid-fluid boundary became highly heterogeneous during the simulation with areas of high shear rate (5-10 fold increase above 200 s) at the projections into the flow geometry and areas of near zero shear rate in the valleys between platelet aggregates by the end of the simulation (Figure 5.12). Thus, within a single simulation (and the corresponding microfluidic experiment) a large range of shear rates are sampled by platelets, even in the presence of a constant inlet wall shear rate. Low shear recirculation regions of up to 10 µm were formed within the valleys of the platelet deposit (Figure 5.15). At 500 s, the platelet deposit was characterized by platelet clusters 20 to 30 µm in length, fully consistent with microfluidic measurements of platelet cluster size on collagen at this shear rate [62].

5.4.3 Multiscale model predictions of donor-specific platelet deposition under flow

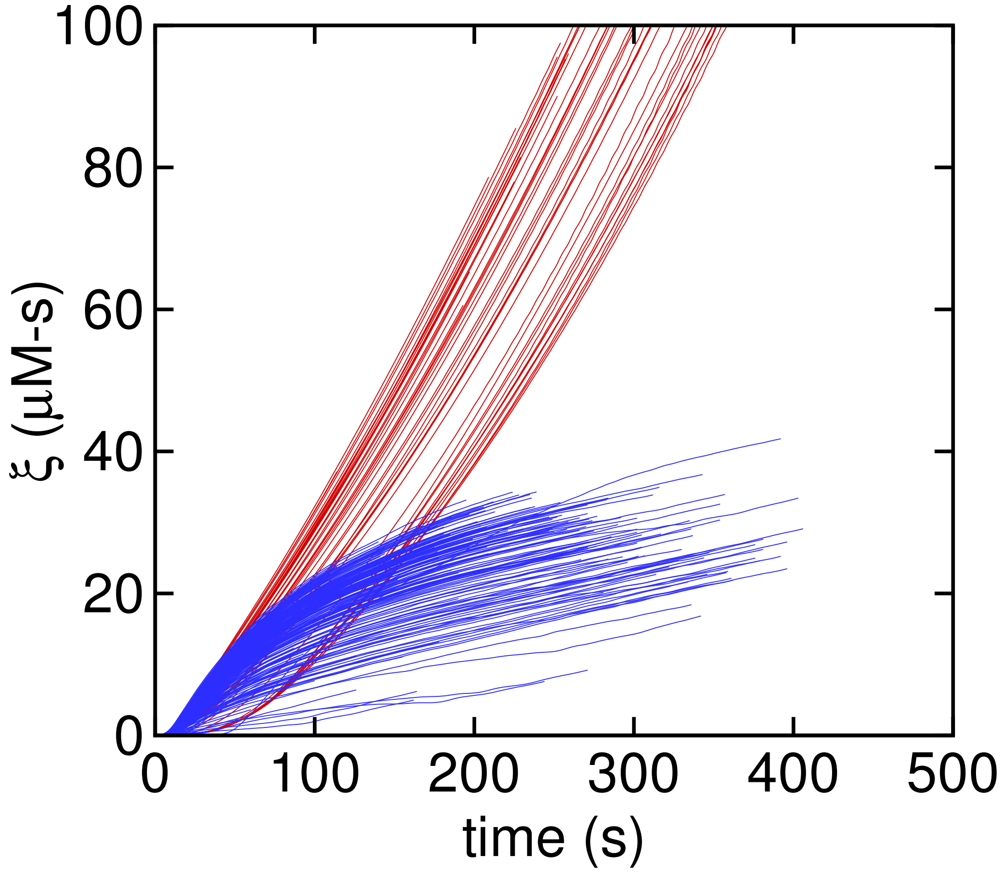

Figure 5.13: Platelet activation in multiscale model simulation for Donor 1. Each line represents the time history of platelet activation, ξ, for each platelet bound to the surface at 500s. Red lines are platelets that are bound to collagen, and possibly other platelets, and blue lines are platelets that are not bound to collagen, but to other platelets. $t = 0$ for each platelet is defined as the time the platelet entered the simulation domain.

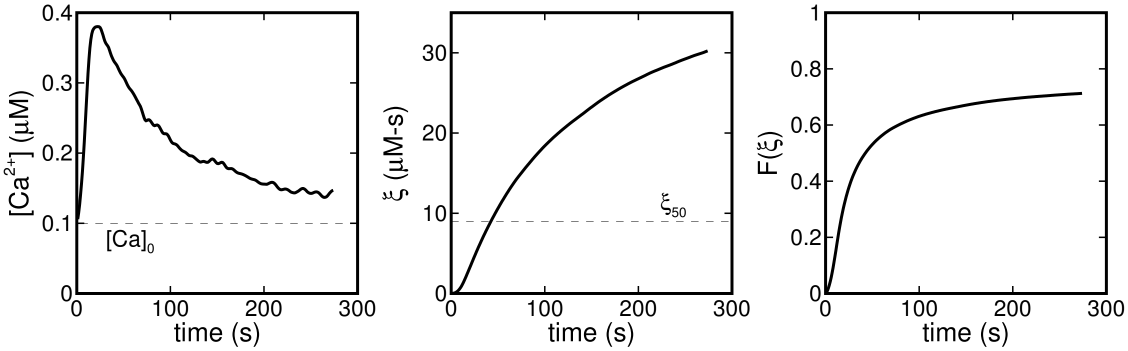

Figure 5.14: Single platelet activation history. Intracellular calcium concentration (left) in response to ADP and TXA_2 stimulation over approximately 250 s transiently increased to almost 400 nM from a basal level of 100 nM. The platelet activation state (middle), ξ, which is related to the integral of intracellular calcium (Equation 5.4), reaches a value above ξ_{50}, but does not achieve a sustained increase. The value of integrin-activation, $F(\xi)$ from Equation 5.5, (right) reaches a maximum of 0.7.

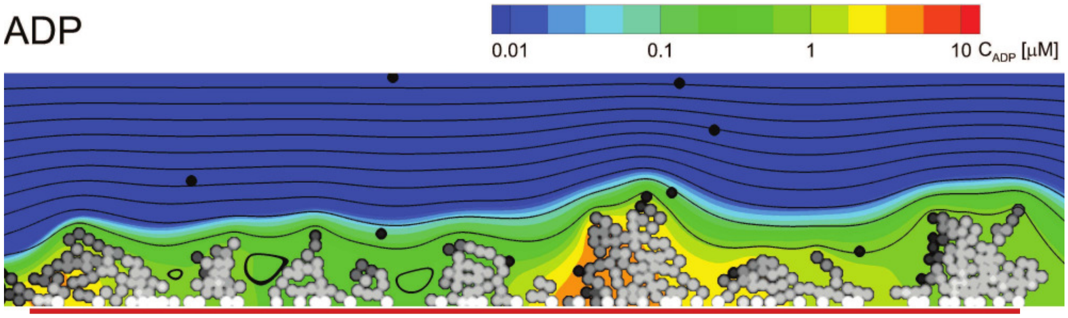

Figure 5.15: Recirculation zones in multiscale simulation. Platelet activation (black, unactivated; white, activated) and deposition at 500 s (inlet wall shear rate, 200 s^{-1}) for Donor 1 in the presence of ADP (top) and TXA_2. Flow: left to right (streamlines, black lines); surface collagen (250 μm long): red bar.

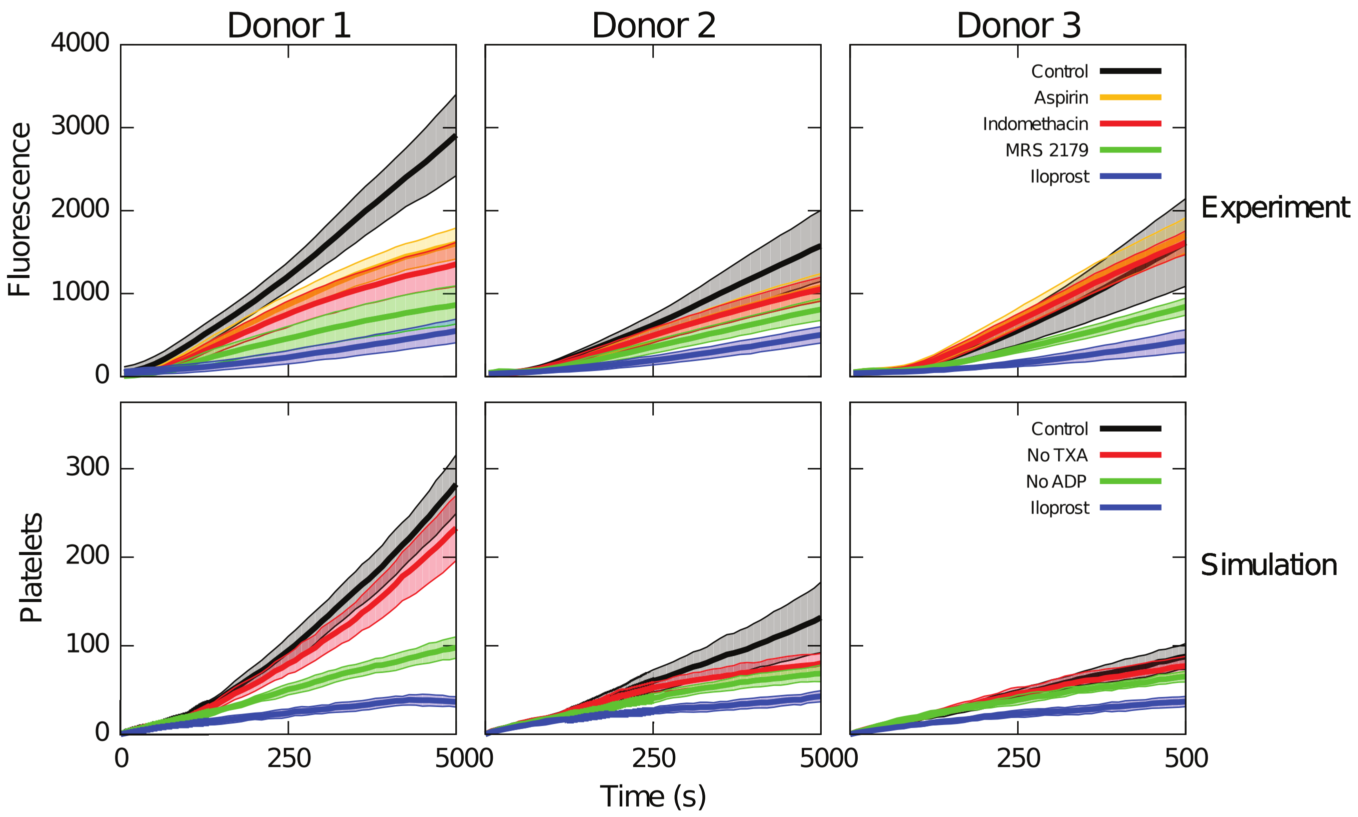

Figure 5.16: Comparison of microfluidic experiment and multiscale simulations of platelet deposition. Measured platelet deposition dynamics for 3 donors in the presence of aspirin, indomethacin, MRS-2179, and iloprost (top row) and corresponding donor-specific multiscale simulations with no TXA_2 (indomethacin or aspirin), no ADP (MRS-2179), and iloprost treatment (bottom row). Shading shows standard deviation. Experiment: control, n=24, 22, and 22 for Donors 1, 2, and 3 respectively; aspirin, n=8; indomethacin, n=8; MRS-2719, n=8; iloprost, n=14. Simulation: n=16 for all conditions and donors.

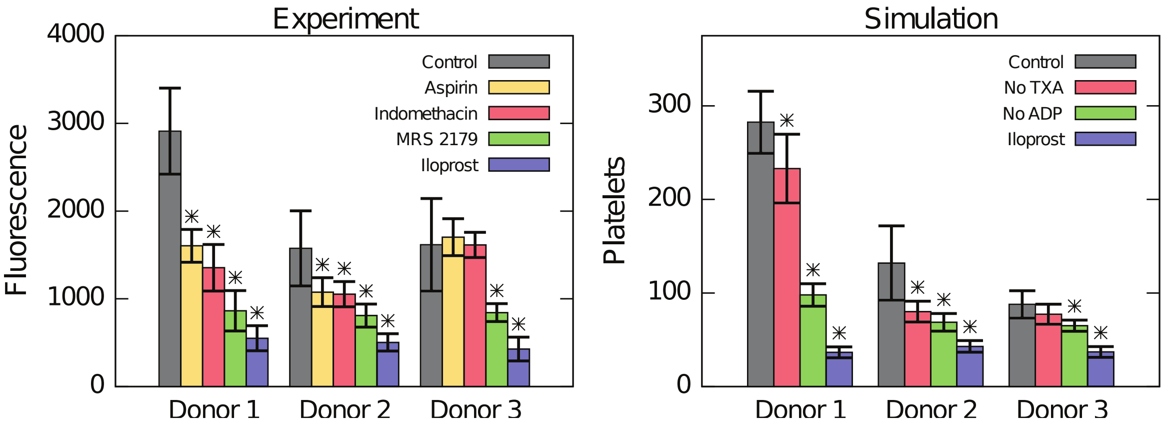

Figure 5.17: Comparison of microfluidic experiment (left) and multiscale simulation (right) at 500 s for Donors 1–3. Experiment: control, n=24, 22, and 22 for Donors 1, 2, and 3 respectively; aspirin, n=8; indomethacin, n=8; MRS-2719, n=8; iloprost, n=14. Simulation: n=16 for all conditions and donors. * $p < 0.01$, relative to control for each donor.

Using microfluidic devices, realtime platelet deposition from PPACK-treated whole blood flowing over fibrillar collagen (250 µm × 250 µm patch) was measured for 500 s at an inlet wall shear rate of $200\,\mathrm{s}^{-1}$ for 3 separate donors under untreated conditions or in the presence of ASA (acetylsalicylic acid or aspirin), indomethacin, MRS-2179, or iloprost (Figure 5.16). In the two dimensional simulations, the overall extent of platelet deposition was measured by the number of platelets on a patch with surface area of $750\,\mu\mathrm{m}^2$ (a 250 µm × 3 µm slice) (Figure 5.16) over 500 s. In the simulations, a total of 100 to 300 platelets were deposited on the collagen surface at 500 s for the control condition (corresponding to 8,000 to 25,000 platelets on a 250 µm × 250 µm area), which compares very well with maximal deposition measured in the microfluidic experiment (20,000 platelets at a fluorescence of 3000 in Figure 5.16). A wide variety of platelet biology was examined using drug treatments. For both experiment and simulation, all donors were most sensitive to iloprost and least sensitive to removal of TXA_2 via indomethacin or aspirin treatment ($[TXA_2] = 0$ in the simulation). The effect of removing ADP induced calcium mobilization via MRS-2179 treatment ($[ADP] = 0$ in the simulation) was between that of iloprost and removing TXA_2. Blood from Donor 1 was observed to produce significantly larger clots at 500 s than blood from Donors 2 and 3 under control conditions ($p < 0.001$) (Figure 5.17), a trait predicted in multiscale modeling. In both experiment and simulation, Donors 1 and 2 exhibited significant sensitivity ($p < 0.01$) to COX-1 therapy (indomethacin or aspirin in the experiment; $[TXA_2] = 0$ in the simulation) at 500 s, while Donor 3 was insensitive to indomethacin or aspirin in both simulation and experiment. For Donors 1 and 2, the effect of removing TXA_2 via COX-1 inhibition occurred after approximately 250 s in the experiment, which corresponded well to the time at which physiologically active levels of TXA_2 were predicted to occur in the boundary layer from the simulations. In both simulation and experiment, the effect of ADP removal or iloprost treatment occurred after 100 s, the time at which propagation of the platelet aggregate away from the clot surface began.

5.5 Discussion

Although some model parameters were fit to overall trends in the platelet density for Donor 1, there were no parameter combinations that allowed for the fit of each individual output. For example, there is no simple set of parameters that can be tuned to fit the dynamic response of iloprost relative to control. This information is embedded in the NN. After choosing initial guesses for each unknown parameter, individual parameters and sometimes sets of parameters, generally two or three, were varied to find regions of parameter space that closely matched the experimental trends for Donor 1. In general, it was found that the ranked order of pharmacological treatment was consistent for any parameter set but the overall potency could be varied especially by changing the critical value for agonist release and integrin activation, ξ_{50}. In general, choosing a small value of ξ_{50} resulted in relatively uniform, large clots over all donors and drug treatments, while choosing a large value of ξ_{50} resulted in relatively uniform, small clots for all donors and drug treatments. The relative affinity of U46619 and TXA_2 to TP, θ, can be used to tune the potency of COX-1 therapy, but only to a limited degree, i.e. a hundred-fold change in θ did not drastically alter the results. This suggests that ADP signaling is the main modulator of clot formation, and TXA_2 plays a more minor role at the conditions explored. This trend is also seen in the difference between the potencies of MRS-2179 and COX-1 therapies. Iloprost was found to be the most potent therapy by damping the calcium signal to all other agonists. The model was also found to be robust to changes in donor and other pharmacological therapy (MRS-2179 therapy was not used to train the model). Ideally, these parameters should be verified from experimental values or more detailed models of platelet-platelet binding [75, 76], but the parameters found in this model are physiologically reasonable. The model also predicted donor-specific platelet aggregate densities.

The standard deviation in the platelet density of the simulation was comparable to that observed with the microfluidic chamber replicates. The simulation results were expected to have a larger spread from taking a small slice of the microfluidic chamber. Several assumptions of homogeneity were made in the model that reduced the variability within the simulations as compared to the microfluidic experiments. Platelets were assumed to have a uniform radius, although in blood platelets have a size distribution. In the microfluidic chambers, the fibrillar collagen is not likely to be uniformly deposited within each patch and when compared across channels, while in the simulation the surface was assumed to be homogeneous. In the simulations, platelets were assumed to have the same activation dynamics, although there is evidence that subpopulations of platelets have different phenotypes [139, 140].

To bridge the gap between in vitro and in vivo prediction, more accurate vessel geometries should be considered in the future, including stenotic vessels. Thrombin generation is also a key component of clotting in vivo. The coagulation cascade was neglected in this model to enable patient-specific predictions of platelet function but is necessary for predictions of clinical value. Some challenges of including thrombin generation in a multiscale model are discussed in Chapter 6. Another limitation is the lack of multicell fragmentation kernels and solid-mechanics calculations. For large clot structures that approach occlusion, platelet aggregates can begin to fragment in clusters rather than a cell-by-cell erosion process. For small clusters, the erosion process is expected to dominate the fragmentatin process. To account for stress-concentrating geometry formation, Picioreanu et al. removed sections of cellular aggregates that exceeded some critical stress threshold due to the surrounding fluid flow [141]. They also found that small clusters tend to undergo cell erosion rather than multi-cell fragmentation (sloughing in the biofilm literature).

5.6 Conclusions

The multiscale model represents the first computational model of thrombosis that includes a patient-specific representation of platelet signaling with validation to patient-specific flow experiments. This is a major step towards creating a comprehensive multiscale model to predict clotting and bleeding risk in vivo. The key aspects of platelet aggregation captured by the model are platelet signaling, platelet binding, platelet motion, transport of soluble agonists (ADP and TXA_2), and hemodynamics. Platelet signaling was obtained from high-throughput experimental measures of intracellular calcium, which was the source of platelet-specific platelet phenotype. The platelet calcium phenotype was previously shown to be repeatably patient-specific [67]. A neural network trained on a specific donor's experimental data was then used in the multiscale model. An integration activation state was estimated from the integral of the calcium concentration above the basal level. This allowed for direct comparison to microfluidic models of platelet aggregation to collagen in flow. The model accurately described platelet aggregation for three donors and three pharmacological treatments (COX-1 therapy, $P2Y_1$ inhibition, and iloprost stimulation).

To further tailor the model to a specific donor, more detailed information can be included in the model, e.g. platelet size distribution and receptor copy number. The addition of thrombin generation to this model will further the clinical predictive power. However, patient-specific experimental coagulation phenotyping and models for describing these results will need to be developed to truly make patient-specific predictions with thrombin generation.

Chapter 6

Future work

6.1 Thrombin generation

Thrombin generation is an essential process in stable clot formation. Thrombin is generated through the coagulation cascade, a series of enzymatic steps that each convert a zymogen to an active enzyme, e.g. the zymogen V is converted to the active enzyme Va by thrombin (IIa). The cascade is started physiologically by the exposure of tissue factor (TF) at the site of injury. TF binds VIIa to produce small amounts of Xa and IXa. Xa is capable of cleaving prothrombin (II) to thrombin (IIa) initially but is much slower than the action of Xa in conjunction with its cofactor Va, which is itself produced by thrombin. IXa along with its cofactor VIIIa serve to generate large amounts of Xa. VIIIa is also produced by thrombin. The intrinsic cascade including Factor XIa further amplify the procoagulant signal . There are several layers of inhibition including antithrombin III (ATIII) and activated protein C (APC) mediated deactivation of Factors Va and VIIIa. Thrombin is a potent platelet activator by cleaving short peptides in the extracellular domain of the PAR receptors, and many of the steps in the cascade are sped up when assembled on the platelet surface. Thrombin also converts fibrinogen to fibrin, which polymerizes to form a stabilizing meshwork within and around the clot.

Thrombin generation is critical to include in clinically relevant models of thrombosis. Deficiencies in Factors XIII or IX are known as Hemophilia, which presents a large risk of bleeding. Factor V Leiden reduces the inhibitory actions of APC and results in a hypercoagulable disorder. Hockin et al. developed one of the first models of well-mixed thrombin generation with a tissue factor stimulus [68]. Kuharsky and Fogelson described a coagulation model in flow that accounted for the arrival and removal of species to the surrounding fluid flow [70]. Later, Leiderman and Fogelson extended the previous model under flow by explicitly modeling the transport processes coupled to platelet deposition [84]. Chatterjee et al. considered a well-mixed system, but included the effects of platelet activation and the intrinsic pathway starting with XIIa activation [71]. Xu et al. included a coagulation model in a cellular Potts model of platelet deposition [85].

The multiscale model in Chapter 5 contains 2 partial differential equations (PDEs): one for ADP and one for TXA_2. These PDEs are uncoupled for a static platelet configuration and are coupled only through the recruitment of new platelets. Coagulation models typically contain on the order of 50 coupled PDEs with several time scales including fast binding and unbinding of coagulation factors and slow generation of active enzymes. It is computationally challenging to include a stiff system of PDEs for simulations of hundreds to thousands of conditions needed to make patient-specific predictions with several pharmacological mediators. For example, the simulations in Figure 5.16 required 192 simulations (16 repeats × 3 donors × 4 conditions). Including thrombin generation for prediction of a wide range of conditions will require optimization of the finite element method (FEM) to achieve faster solution times. Some avenues for reducing computational time are using a nonuniform grid or a moving grid for FEM and simplifying the reaction network (reduce the stiffness and number of PDEs).

6.2 Pressure driven flow within clot

A no-slip boundary condition was imposed on the interface of the bound platelets and the fluid. For small, dense platelet deposits, the flow within the clot is likely to be small. For larger structures, pressure driven flow through the porous clot can contribute to transport of soluble species. The structure of a clot in vivo is not well understood as are the transport properties within the clot. In principal, the pore size within the clot structure could be predicted from a three dimensional simulation, and the flow through the structure could be resolved at the fluid pore level. However, platelets may not maintain an idealized shape inside the clot structure, which will change the pore size distribution. After approximately 10 minutes, platelets will also spread out on the surface. Furthermore, resolving fluid flow on the pore level is computationally costly, so a more coarse-grained approach may be more appropriate. Leiderman and Fogelson used a Brinkman term within the Navier-Stokes equation for the porous flow through the clot structure [84]. A similar scheme is easily adapted to simulations using lattice Boltzmann [142]. Xu et al. described flow within the clot using Darcy's law which was coupled to the normal Navier-Stokes equation in the rest of the domain [85]. However, with current experimental data, it is unclear what the appropriate parameters are for these models or whether inter-clot flow is important to the dynamics of clot growth for the conditions studied here.

6.2.1 Bleeding model

A situation in which inter-clot flow is likely to be important is in a bleeding model, where blood is flowing through the clot itself into the surrounding tissue or air. The pressure drop between the blood and the interstitial fluid (or air) can be much higher than the pressure drop across the clot in the vessel itself. The increased pressure drop will increase the driving force for inter-clot flow. In addition to describing inter-clot flow, another difficulty in modeling bleeding is defining the boundary conditions at the injury not only for the flow but for transport of soluble species and the distribution of collagen.

A bleeding model is likely to drastically change the initial dynamics of platelet aggregation. Platelets will directly flow into the injured surface instead of flowing over the surface, increasing the deposition rate initially. Platelet aggregates will impede flow through the injured surface, which will decrease platelet flux to regions with large aggregates. Regions that do not not have large aggregates will have a relative increase in platelet flux. So bleeding may actually serve as a mechanism to form a more uniform clot structure.

6.3 Detailed signaling model for each platelet

Platelet signaling in the multiscale model was predicted by neural networks trained on experimental data. If we want to make a prediction about how a change in intracellular signaling in the platelet, e.g. disruption of store operated calcium entry, affects clot growth, a high-throughput experiment and training of a neural network is necessary. These experiments may be feasible in animal models where knockouts can be produced, but for human platelets an *in silico* approach is attractive. A platelet signaling model was developed by Purvis et al. to study platelet calcium mobilization in response to ADP stimulation of $P2Y_1$ [65]. In the multiscale model in Chapter 5, platelets also signal through IP, TP, and GPVI (the receptors for iloprost, TXA_2, and collagen, respectively). Developing a detailed model with these receptors would enable simulations where arbitrary changes are made to the signaling within platelets. Furthermore, such a detailed description based on kinetic equations can be solved stochastically to investigate how signal noise within individual platelets affects clot formation.

6.4 Platelet heterogeneity

Heterogeneity of platelets can be manifested in distributions of platelet sizes, receptors on the platelet surface, excitability of the platelets, amount of stored ADP in dense granules, etc. In the multiscale model in this thesis, each platelet was the same size and considered to have the same integrin activation dynamics. Flow cytometry could be used to quantify patient-specific distributions in the model for platelet size and receptor number although the donors in this work were found to have similar receptor number distributions. ADP content can be estimated through a luciferase assay to measure ATP release. Although the ratio of ATP to ADP is known inside the dense granules, it is not likely to be equivalent in all donors, so this measurement may be more valuable to discover large defects in granule release.

Appendix A

Time course of multiscale simulations

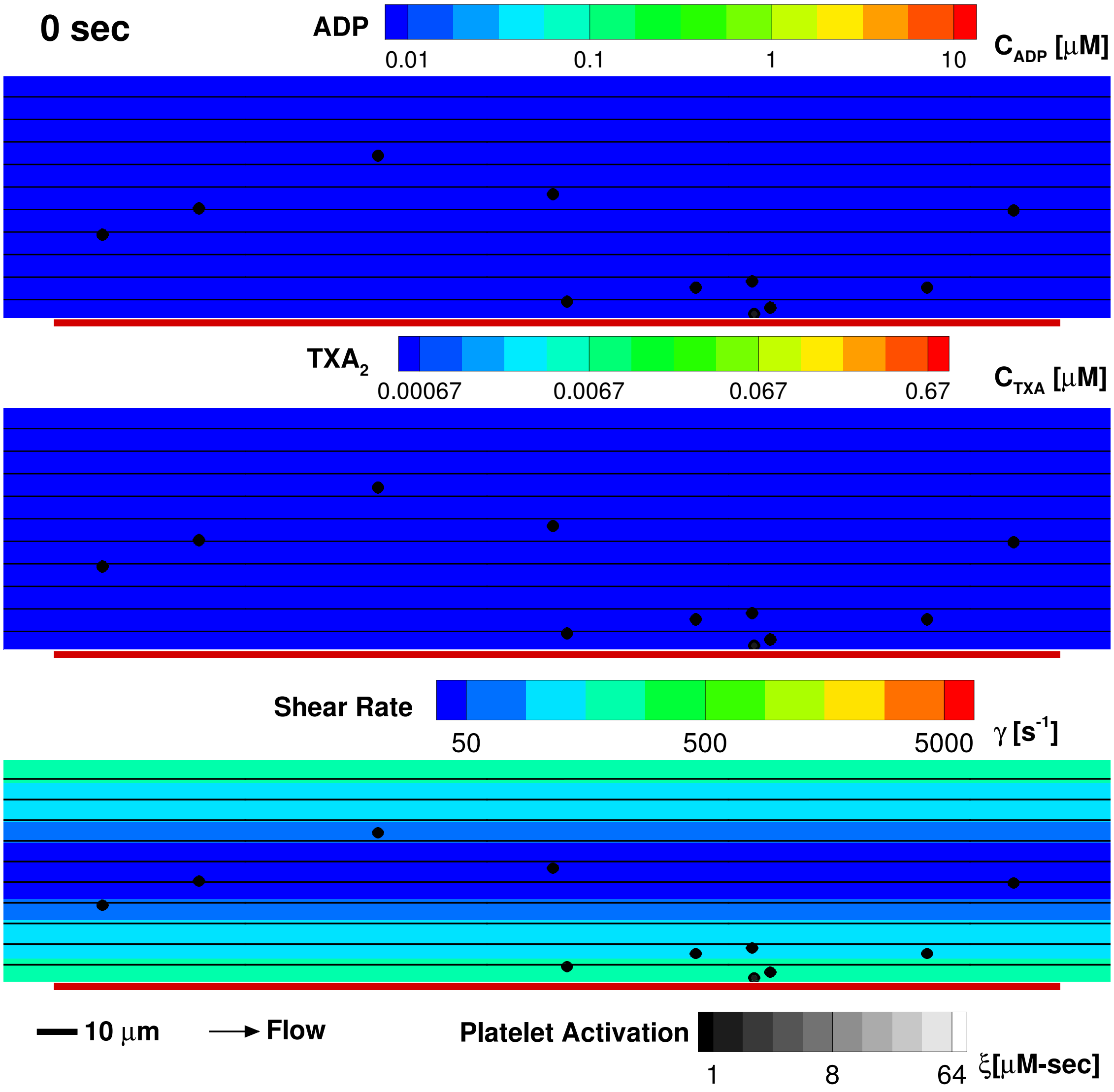

Figure A.1: Multiscale simulation of patient-specific platelet deposition under flow. Platelet activation (black, unactivated; white, activated) and deposition at 0 s (inlet wall shear rate, 200 s^{-1}) for Donor 1 in the presence of ADP (top) and TXA_2 (middle). Flow: left to right (streamlines, black lines); surface collagen (250 µm long): red bar.

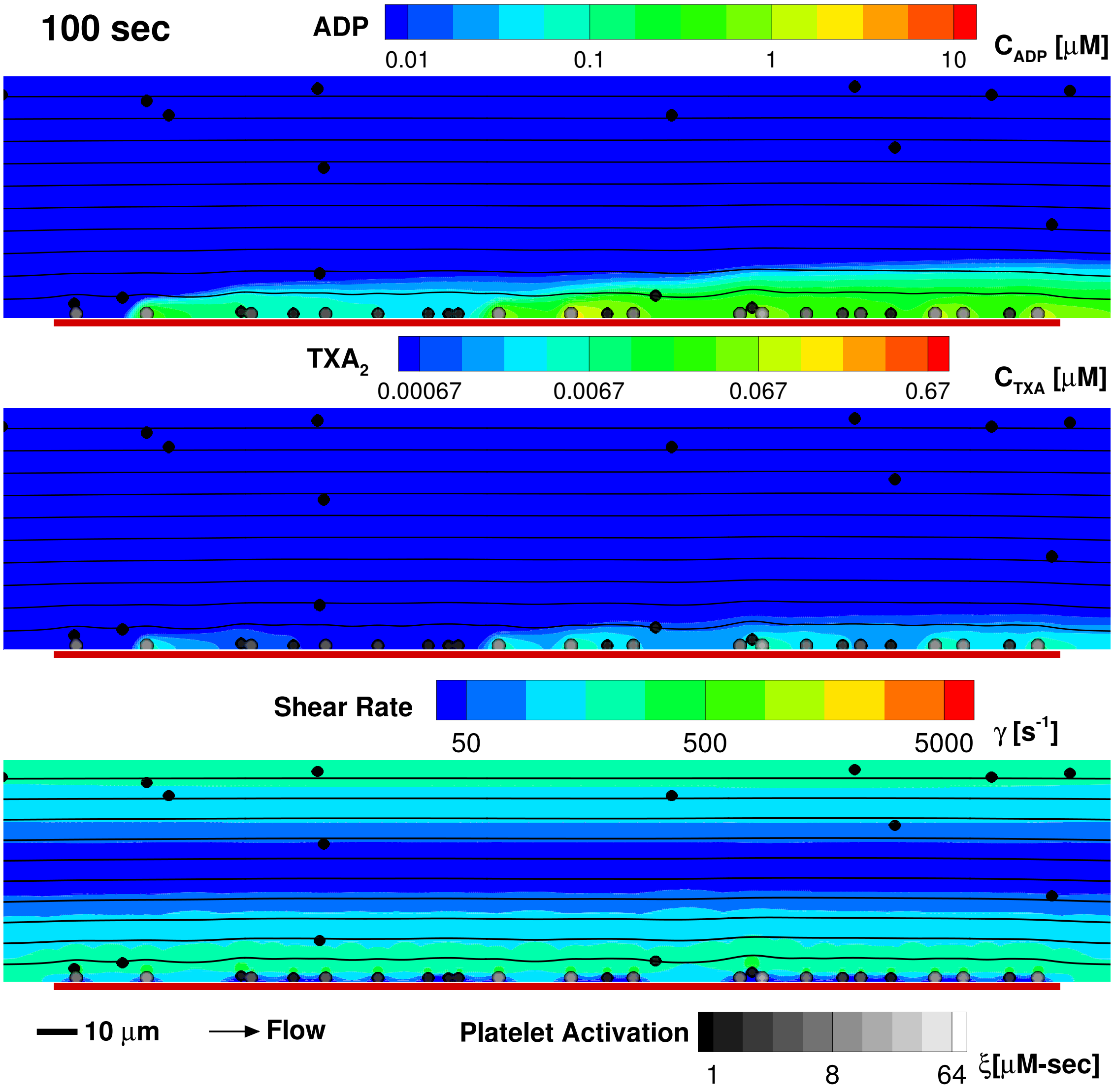

Figure A.2: Multiscale simulation of patient-specific platelet deposition under flow. Platelet activation (black, unactivated; white, activated) and deposition at 100 s (inlet wall shear rate, 200 s^{-1}) for Donor 1 in the presence of ADP (top) and TXA_2 (middle). Flow: left to right (streamlines, black lines); surface collagen (250 µm long): red bar.

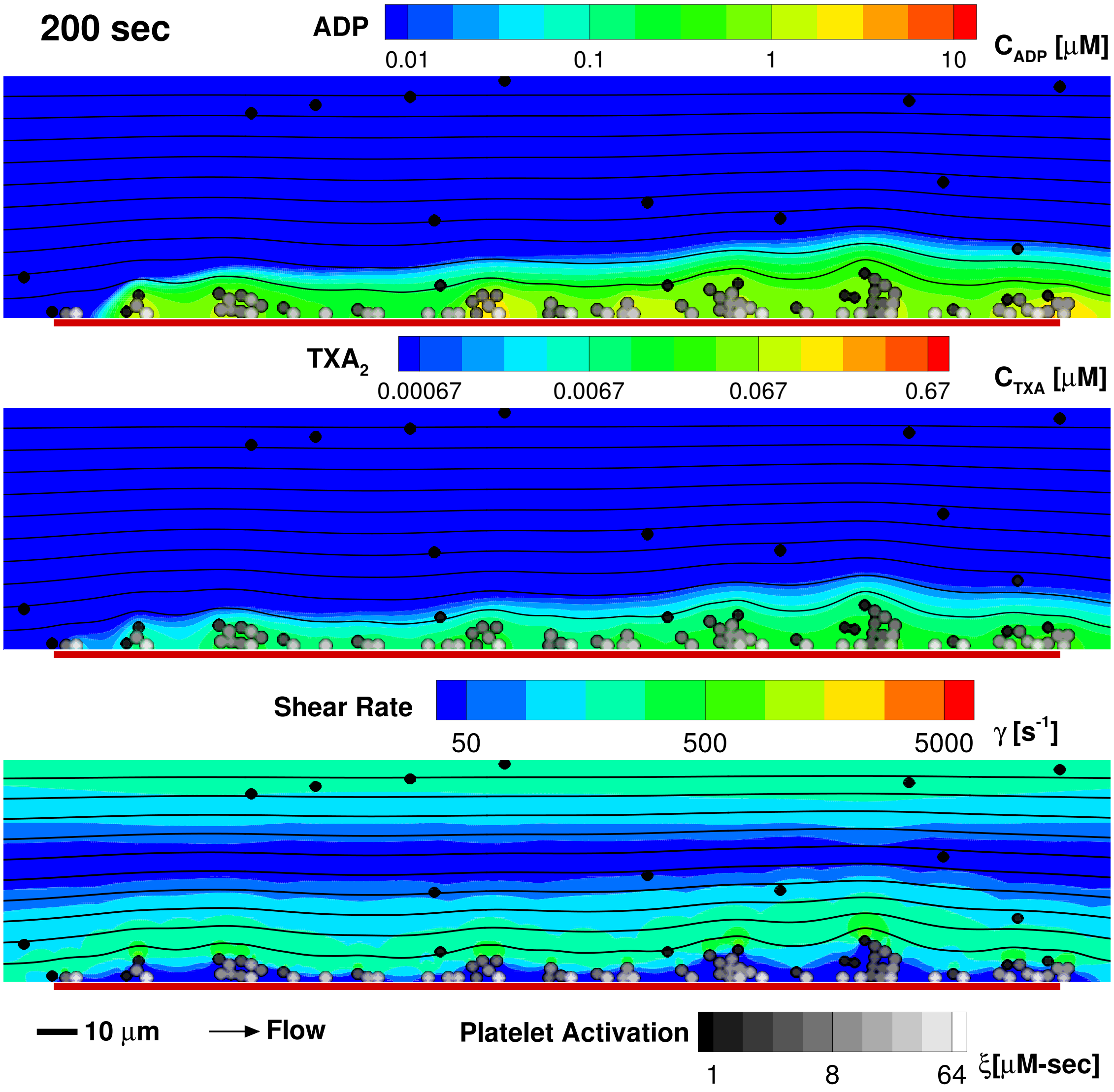

Figure A.3: Multiscale simulation of patient-specific platelet deposition under flow. Platelet activation (black, unactivated; white, activated) and deposition at 200 s (inlet wall shear rate, $200\,s^{-1}$) for Donor 1 in the presence of ADP (top) and TXA_2 (middle). Flow: left to right (streamlines, black lines); surface collagen (250 μm long): red bar.

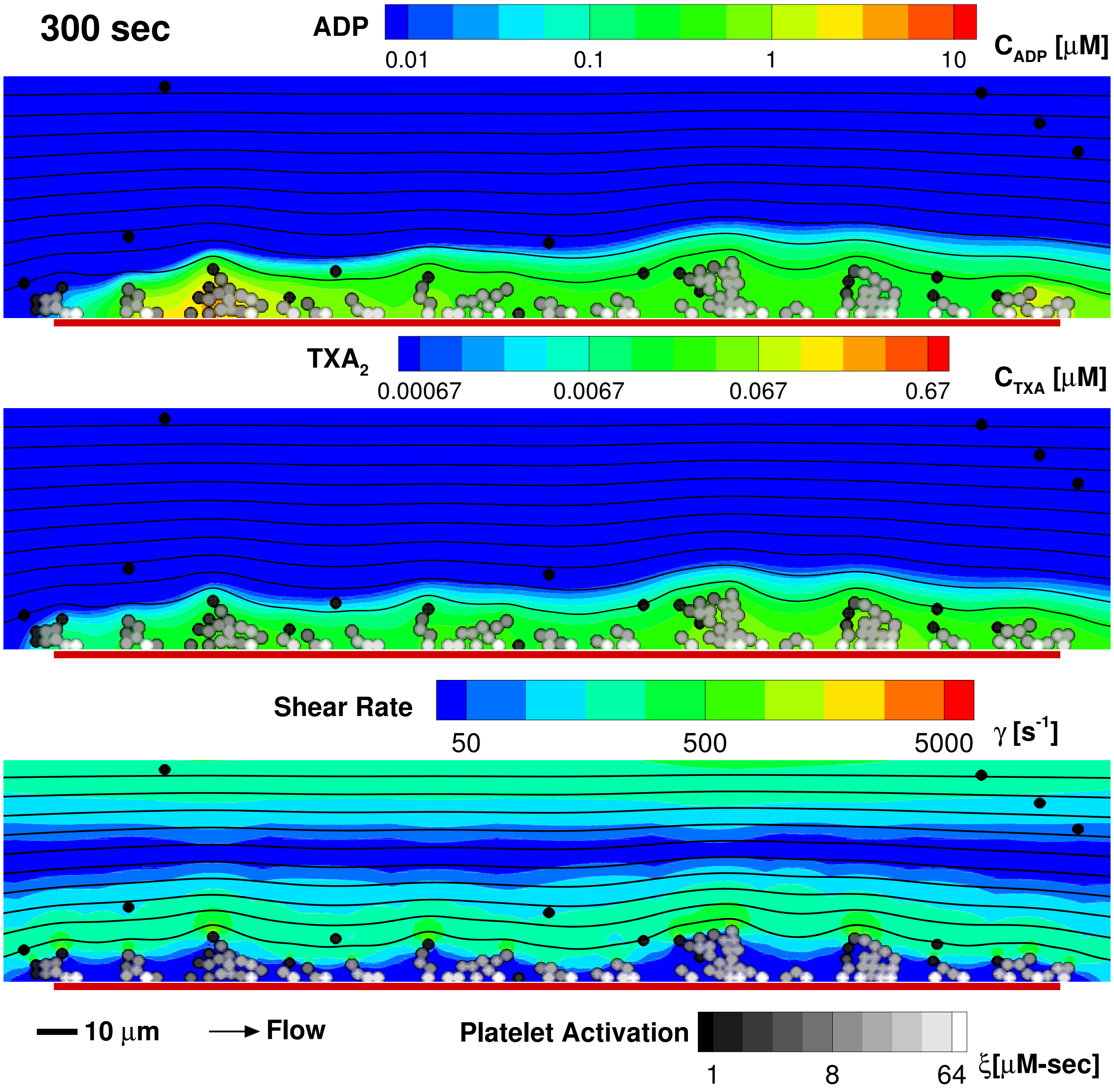

Figure A.4: Multiscale simulation of patient-specific platelet deposition under flow. Platelet activation (black, unactivated; white, activated) and deposition at 300 s (inlet wall shear rate, $200\,\mathrm{s}^{-1}$) for Donor 1 in the presence of ADP (top) and TXA_2 (middle). Flow: left to right (streamlines, black lines); surface collagen (250 µm long): red bar.

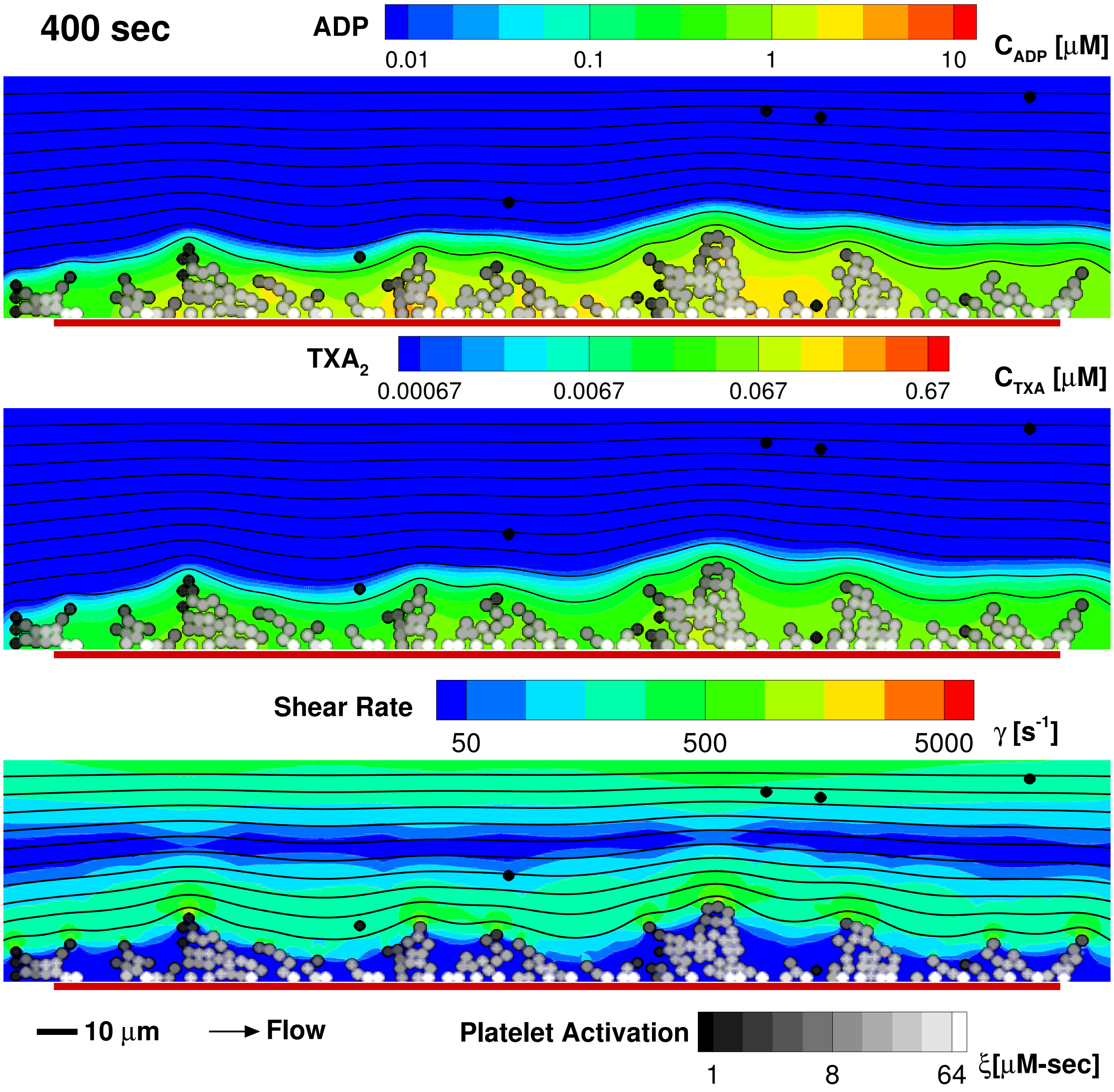

Figure A.5: Multiscale simulation of patient-specific platelet deposition under flow. Platelet activation (black, unactivated; white, activated) and deposition at 400 s (inlet wall shear rate, 200 s^{-1}) for Donor 1 in the presence of ADP (top) and TXA_2 (middle). Flow: left to right (streamlines, black lines); surface collagen (250 μm long): red bar.

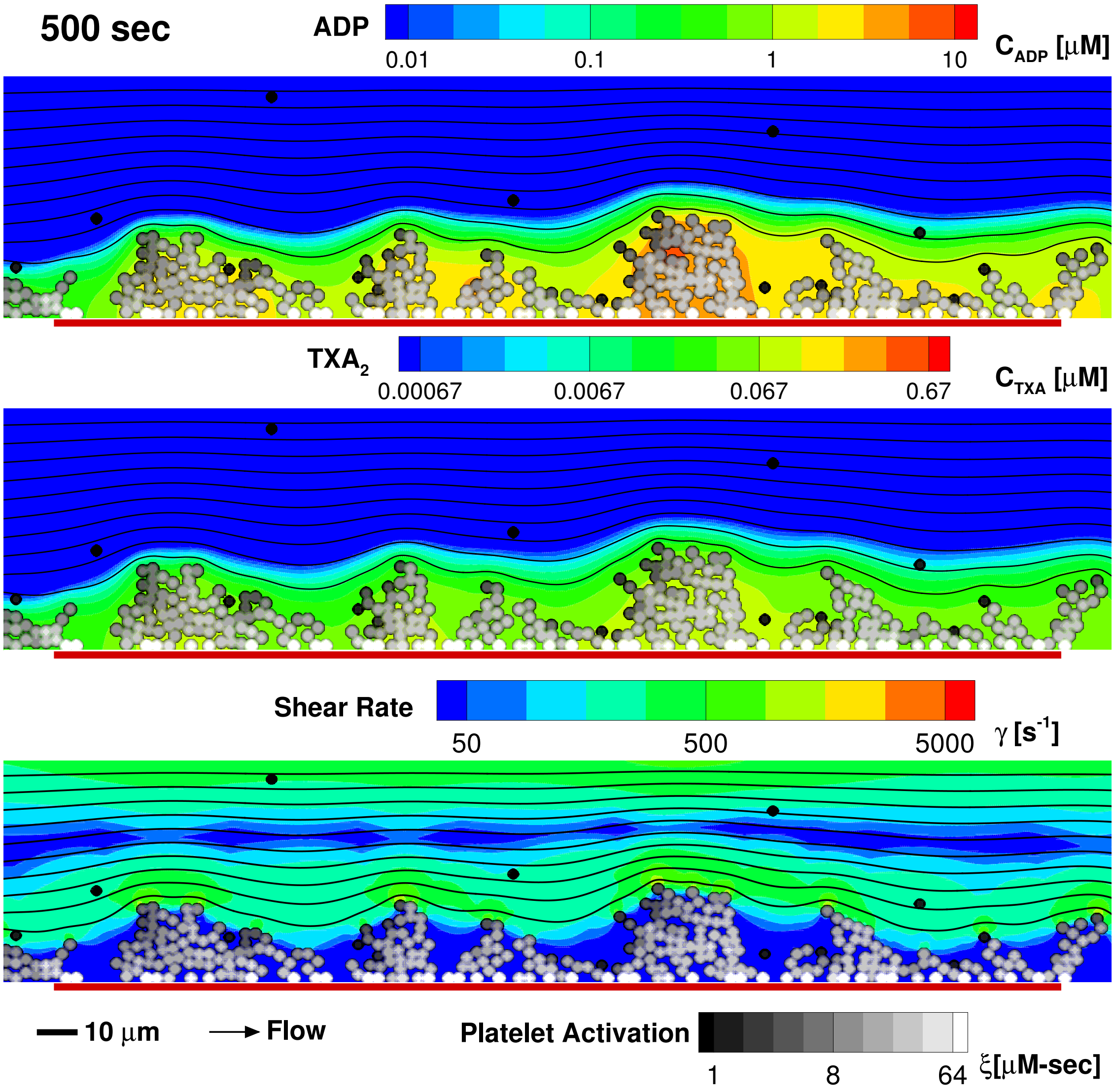

Figure A.6: Multiscale simulation of patient-specific platelet deposition under flow. Platelet activation (black, unactivated; white, activated) and deposition at 500 s (inlet wall shear rate, 200 s^{-1}) for Donor 1 in the presence of ADP (top) and TXA_2 (middle). Flow: left to right (streamlines, black lines); surface collagen (250 μm long): red bar.

Appendix B

Patient-specific predictions

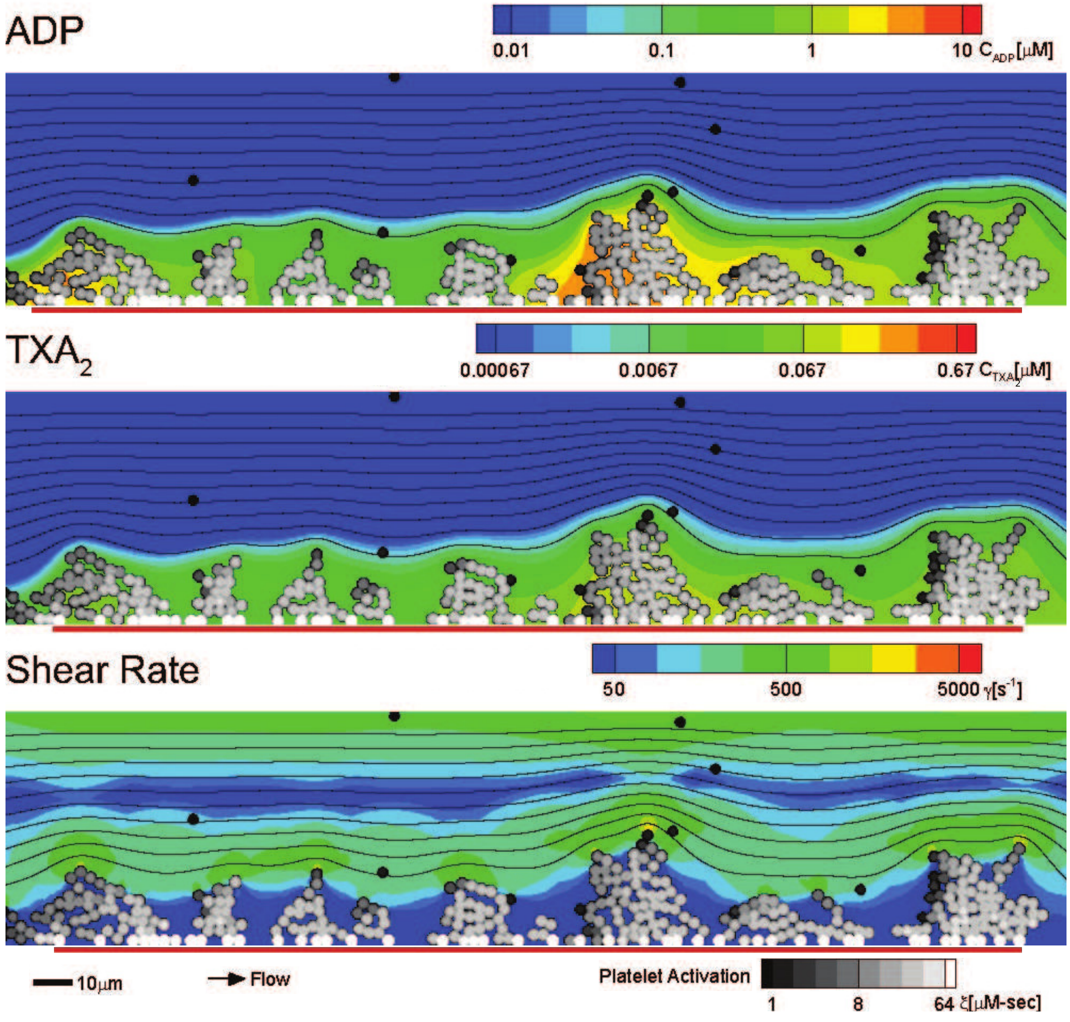

Figure B.1: Donor 1: control (500 s). Platelet activation (black, unactivated; white, activated) and deposition (inlet wall shear rate, $200\,\mathrm{s}^{-1}$) in the presence of ADP (top) and TXA_2 (middle) where local shear rate near the platelet deposit varies markedly from $< 50\,\mathrm{s}^{-1}$ to greater than $1000\,\mathrm{s}^{-1}$ (bottom). Flow: left to right (streamlines, black lines); surface collagen (250 μm long): red bar.

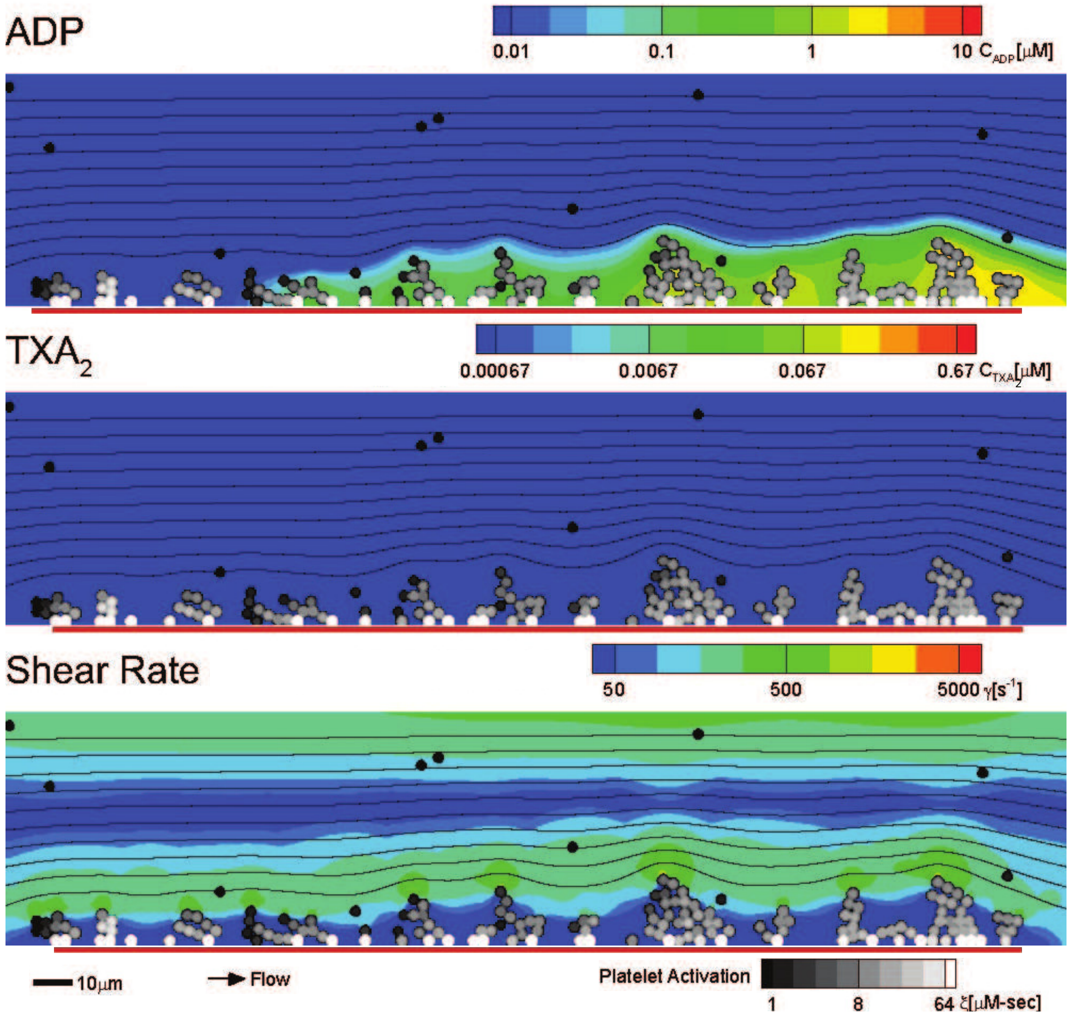

Figure B.2: Donor 1: indomethacin treated (500 s). Platelet activation (black, unactivated; white, activated) and deposition (inlet wall shear rate, $200\,\mathrm{s}^{-1}$) in the presence of ADP (top) and TXA_2 (middle) where local shear rate near the platelet deposit varies markedly from $< 50\,\mathrm{s}^{-1}$ to greater than $1000\,\mathrm{s}^{-1}$ (bottom). Flow: left to right (streamlines, black lines); surface collagen (250 µm long): red bar.

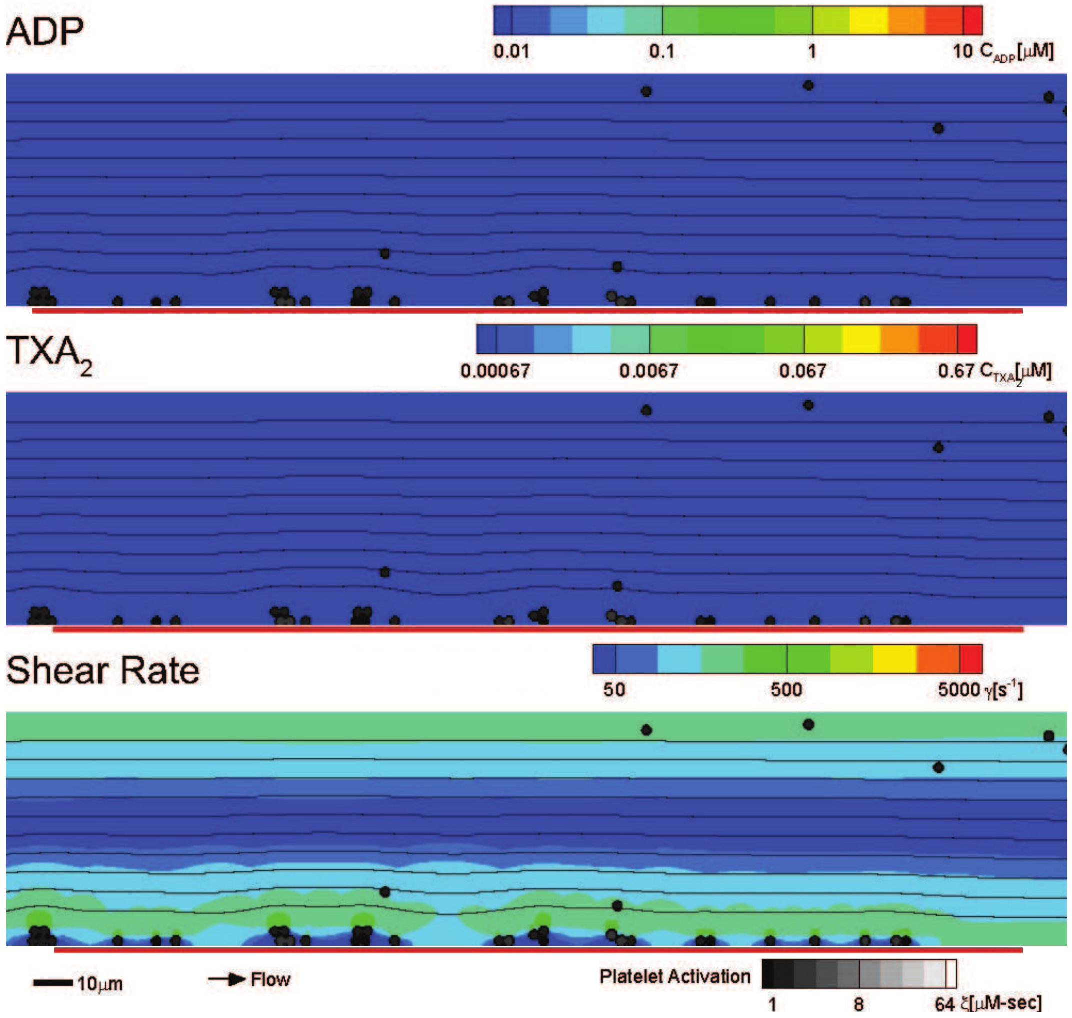

Figure B.3: Donor 1: iloprost treated (500 s). Platelet activation (black, unactivated; white, activated) and deposition (inlet wall shear rate, $200\,s^{-1}$) in the presence of ADP (top) and TXA_2 (middle) where local shear rate near the platelet deposit varies markedly from $< 50\,s^{-1}$ to greater than $1000\,s^{-1}$ (bottom). Flow: left to right (streamlines, black lines); surface collagen (250 µm long): red bar.

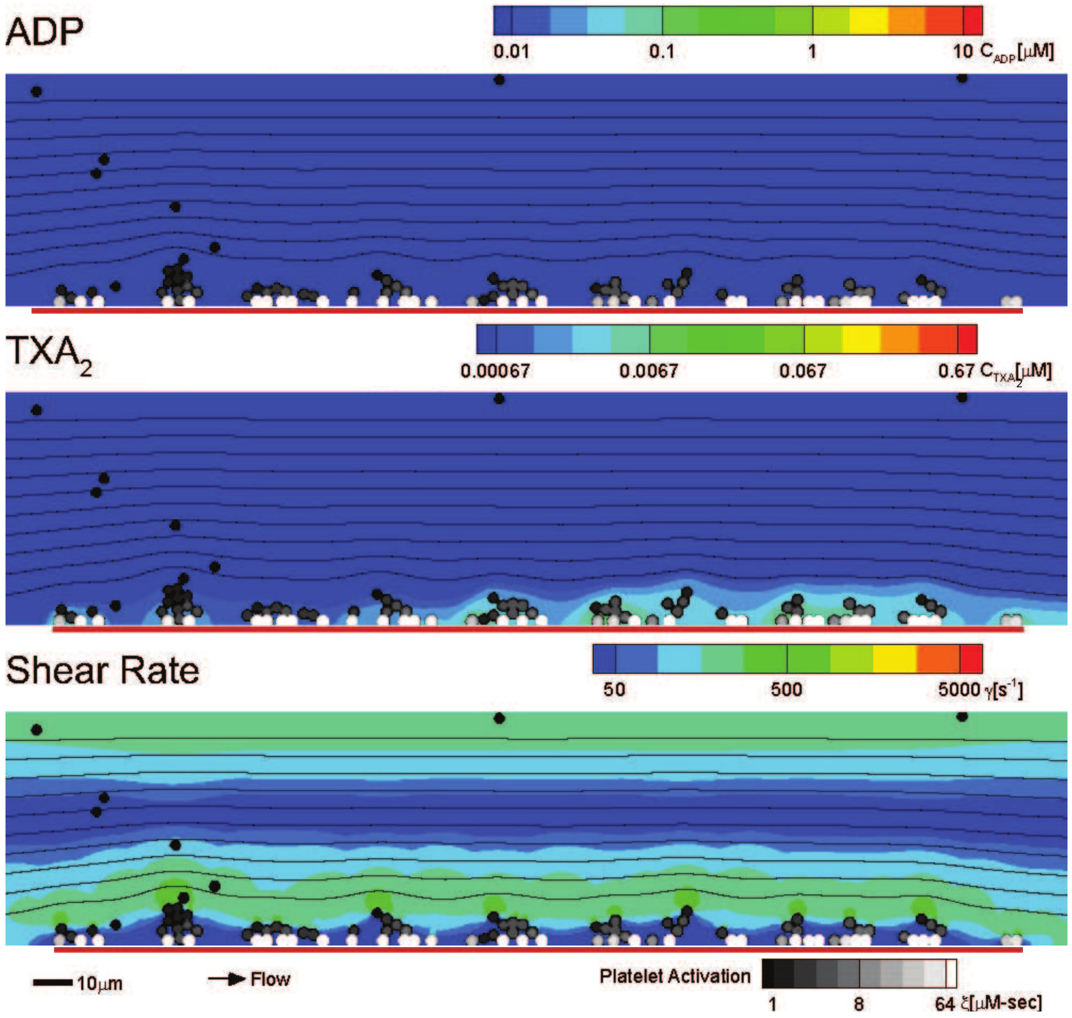

Figure B.4: Donor 1: MRS-2179 treated (500 s). Platelet activation (black, unactivated; white, activated) and deposition (inlet wall shear rate, $200\,\mathrm{s}^{-1}$) in the presence of ADP (top) and TXA_2 (middle) where local shear rate near the platelet deposit varies markedly from $< 50\,\mathrm{s}^{-1}$ to greater than $1000\,\mathrm{s}^{-1}$ (bottom). Flow: left to right (streamlines, black lines); surface collagen (250 μm long): red bar.

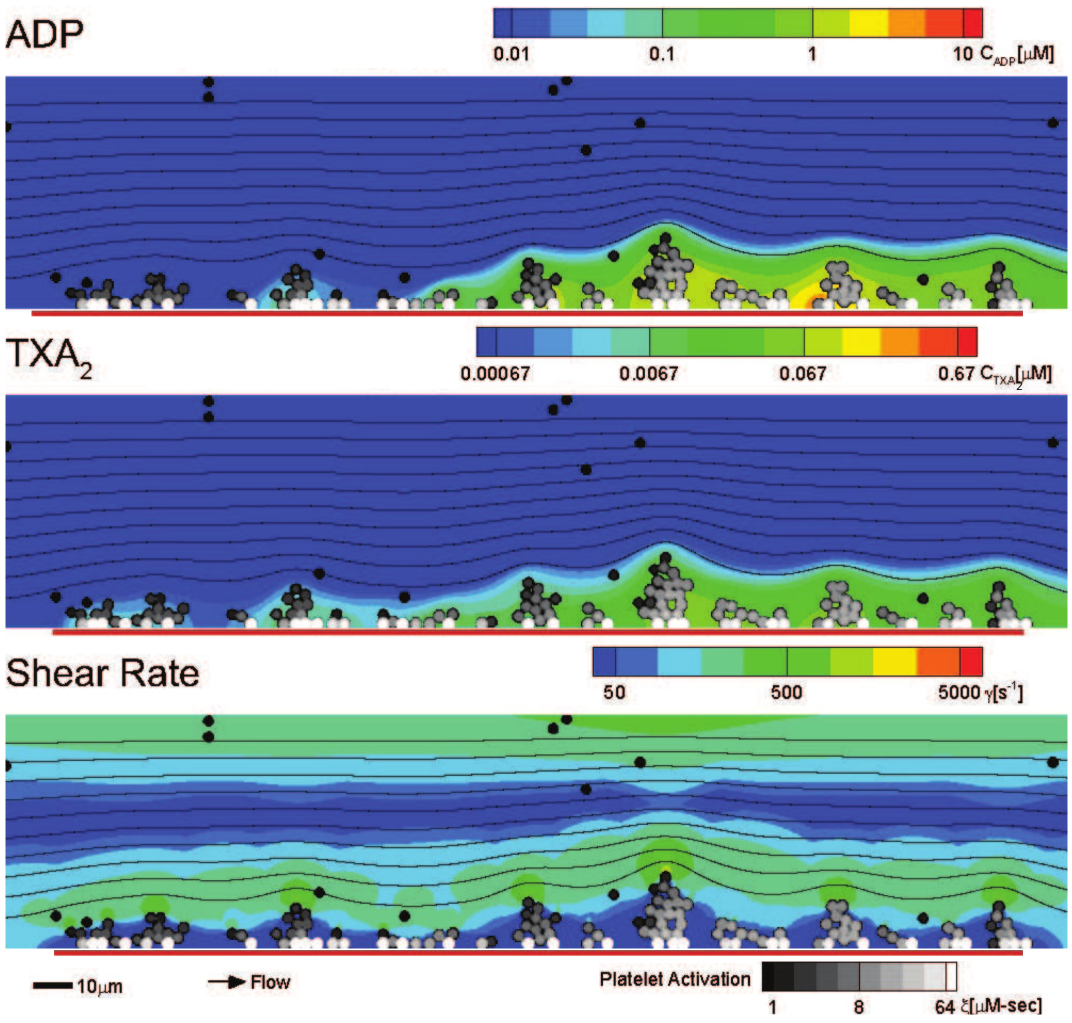

Figure B.5: Donor 2: control (500 s) Platelet activation (black, unactivated; white, activated) and deposition (inlet wall shear rate, 200 s^{-1}) in the presence of ADP (top) and TXA_2 (middle) where local shear rate near the platelet deposit varies markedly from $< 50\,\mathrm{s}^{-1}$ to greater than $1000\,\mathrm{s}^{-1}$ (bottom). Flow: left to right (streamlines, black lines); surface collagen (250 μm long): red bar.

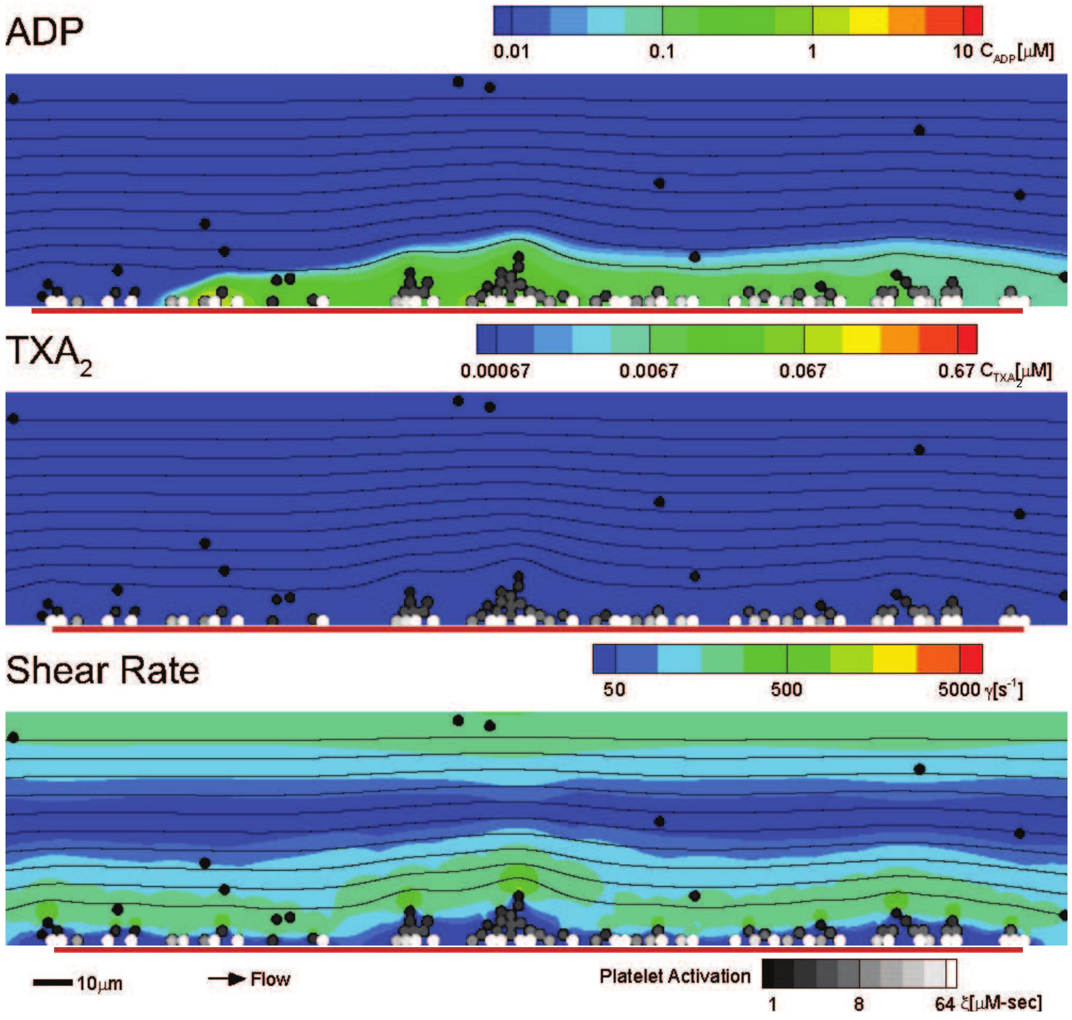

Figure B.6: Donor 2: indomethacin treated (500 s). Platelet activation (black, unactivated; white, activated) and deposition (inlet wall shear rate, 200 s^{-1}) in the presence of ADP (top) and TXA_2 (middle) where local shear rate near the platelet deposit varies markedly from $< 50\,s^{-1}$ to greater than $1000\,s^{-1}$ (bottom). Flow: left to right (streamlines, black lines); surface collagen (250 μm long): red bar.

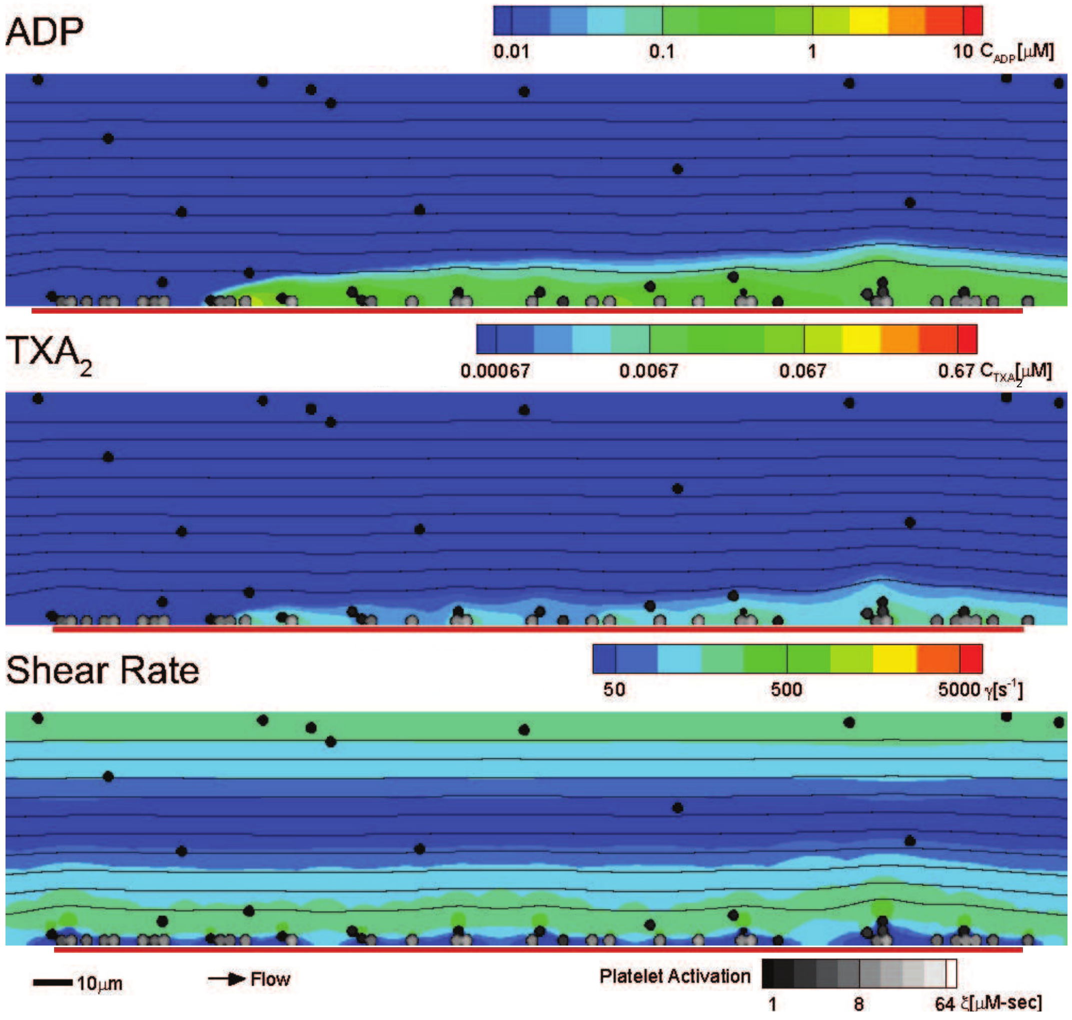

Figure B.7: Donor 2: iloprost treated (500 s). Platelet activation (black, unactivated; white, activated) and deposition (inlet wall shear rate, 200 s^{-1}) in the presence of ADP (top) and TXA_2 (middle) where local shear rate near the platelet deposit varies markedly from $< 50\,s^{-1}$ to greater than $1000\,s^{-1}$ (bottom). Flow: left to right (streamlines, black lines); surface collagen (250 μm long): red bar.

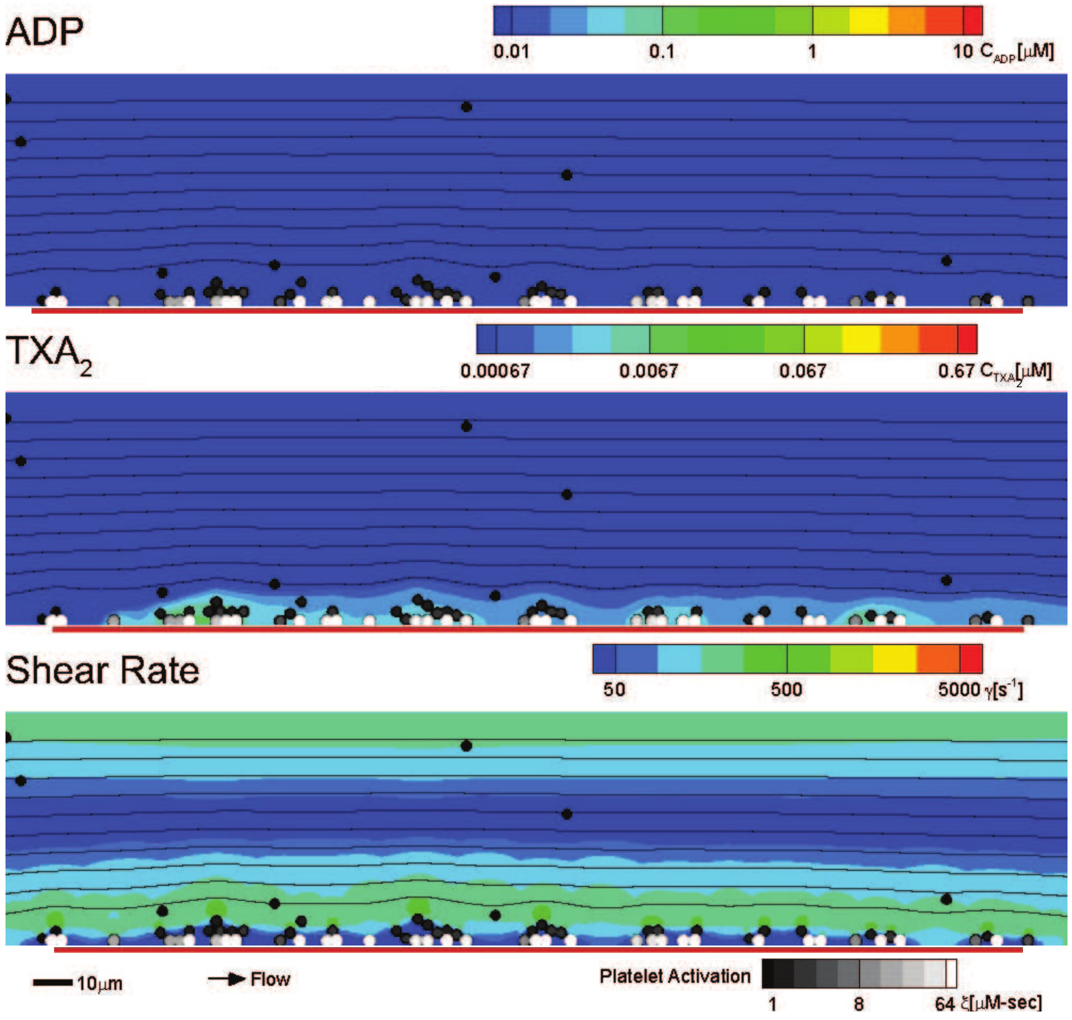

Figure B.8: Donor 2: MRS 2179-treated (500 s). Platelet activation (black, unactivated; white, activated) and deposition (inlet wall shear rate, $200\,s^{-1}$) in the presence of ADP (top) and TXA_2 (middle) where local shear rate near the platelet deposit varies markedly from $< 50\,s^{-1}$ to greater than $1000\,s^{-1}$ (bottom). Flow: left to right (streamlines, black lines); surface collagen (250 µm long): red bar.

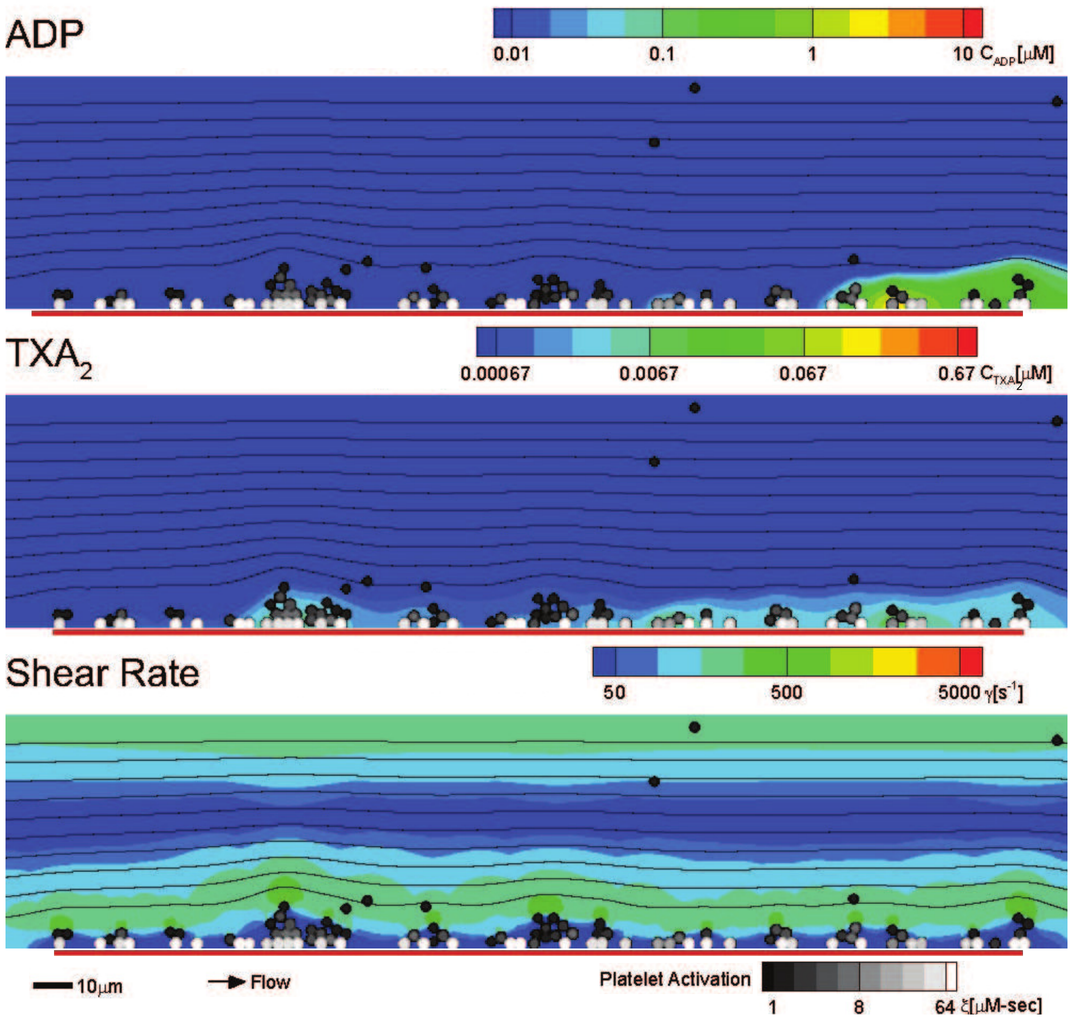

Figure B.9: Donor 3: control (500 s). Platelet activation (black, unactivated; white, activated) and deposition (inlet wall shear rate, $200\,\mathrm{s}^{-1}$) in the presence of ADP (top) and TXA_2 (middle) where local shear rate near the platelet deposit varies markedly from $< 50\,\mathrm{s}^{-1}$ to greater than $1000\,\mathrm{s}^{-1}$ (bottom). Flow: left to right (streamlines, black lines); surface collagen (250 µm long): red bar.

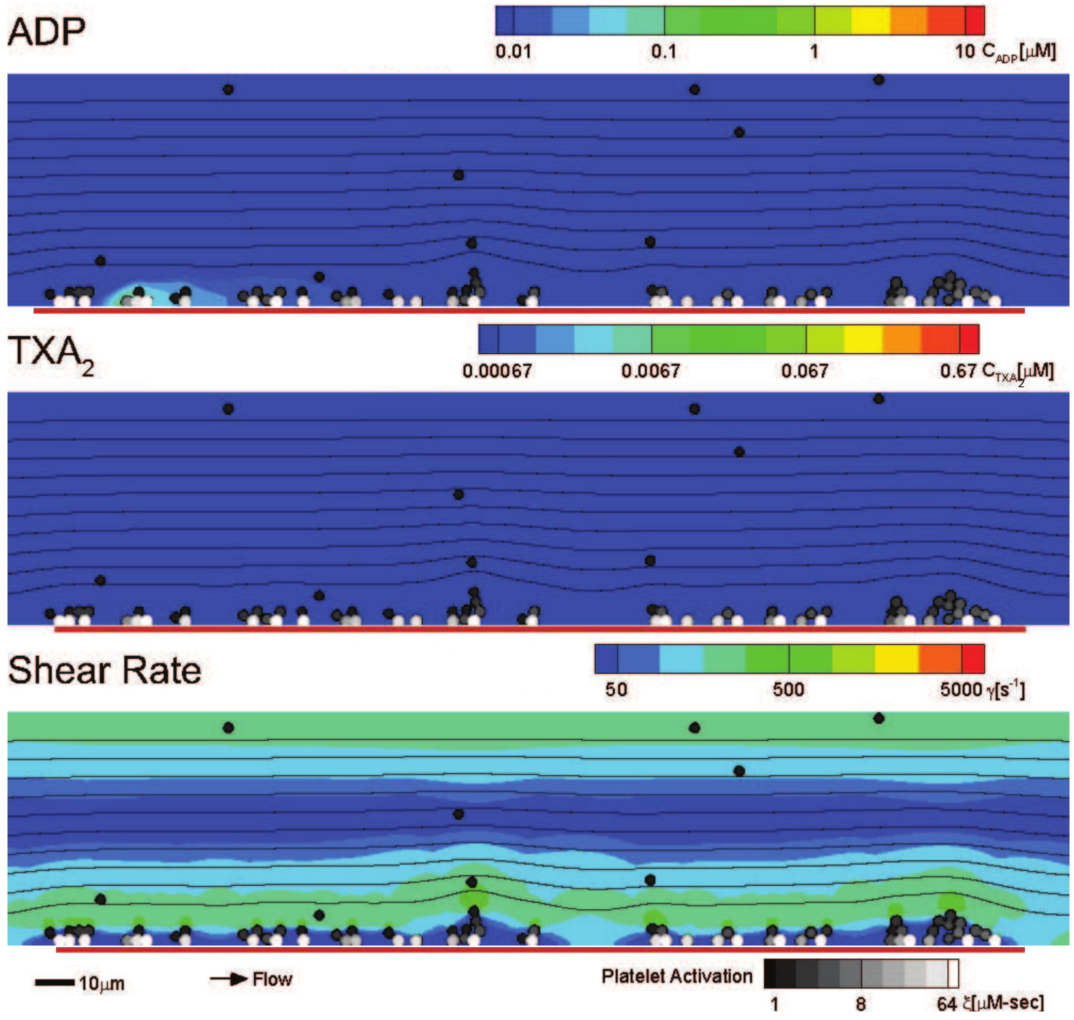

Figure B.10: Donor 3: indomethacin treated (500 s). Platelet activation (black, unactivated; white, activated) and deposition (inlet wall shear rate, $200\,\mathrm{s}^{-1}$) in the presence of ADP (top) and TXA_2 (middle) where local shear rate near the platelet deposit varies markedly from $< 50\,\mathrm{s}^{-1}$ to greater than $1000\,\mathrm{s}^{-1}$ (bottom). Flow: left to right (streamlines, black lines); surface collagen (250 µm long): red bar.

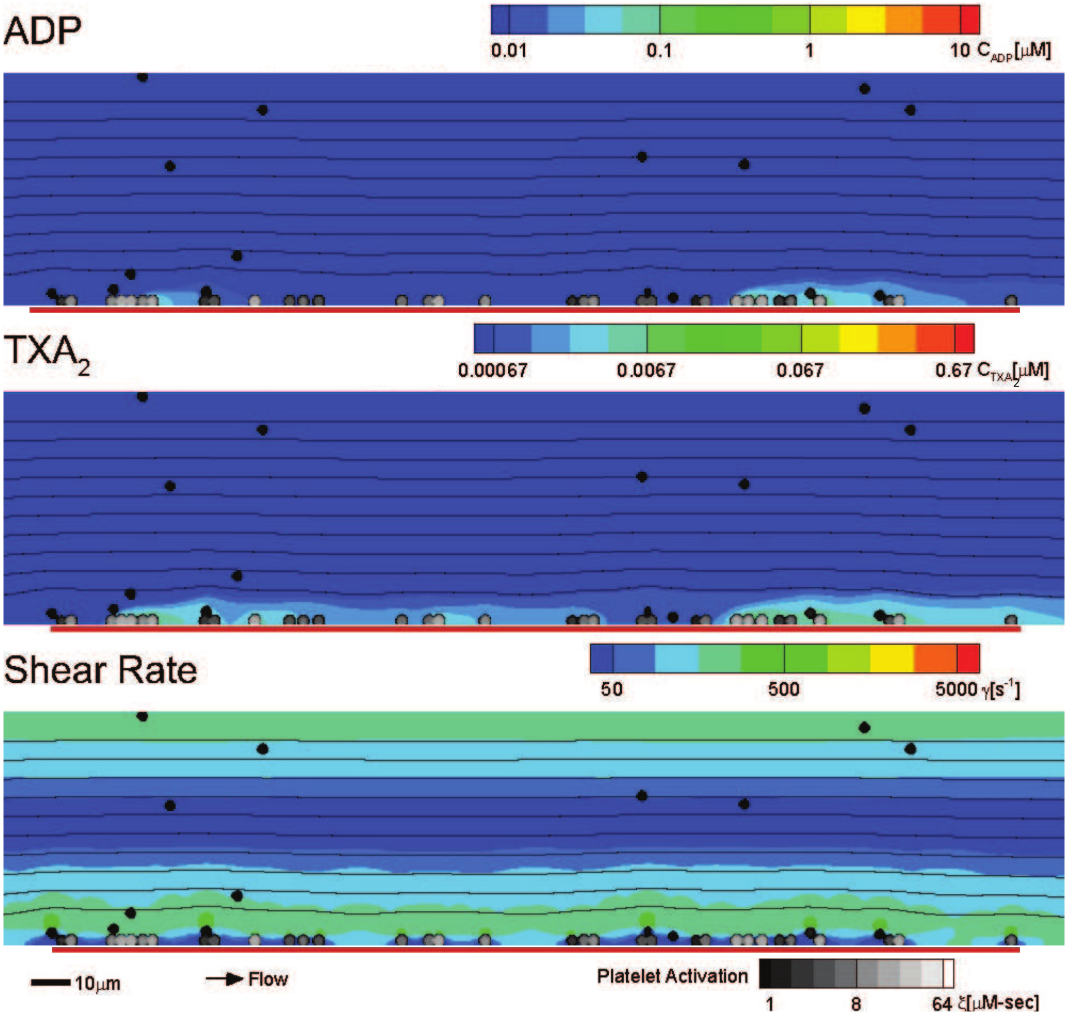

Figure B.11: Donor 3: iloprost treated (500 s). Platelet activation (black, unactivated; white, activated) and deposition (inlet wall shear rate, $200\,\mathrm{s}^{-1}$) in the presence of ADP (top) and TXA_2 (middle) where local shear rate near the platelet deposit varies markedly from $< 50\,\mathrm{s}^{-1}$ to greater than $1000\,\mathrm{s}^{-1}$ (bottom). Flow: left to right (streamlines, black lines); surface collagen (250 µm long): red bar.

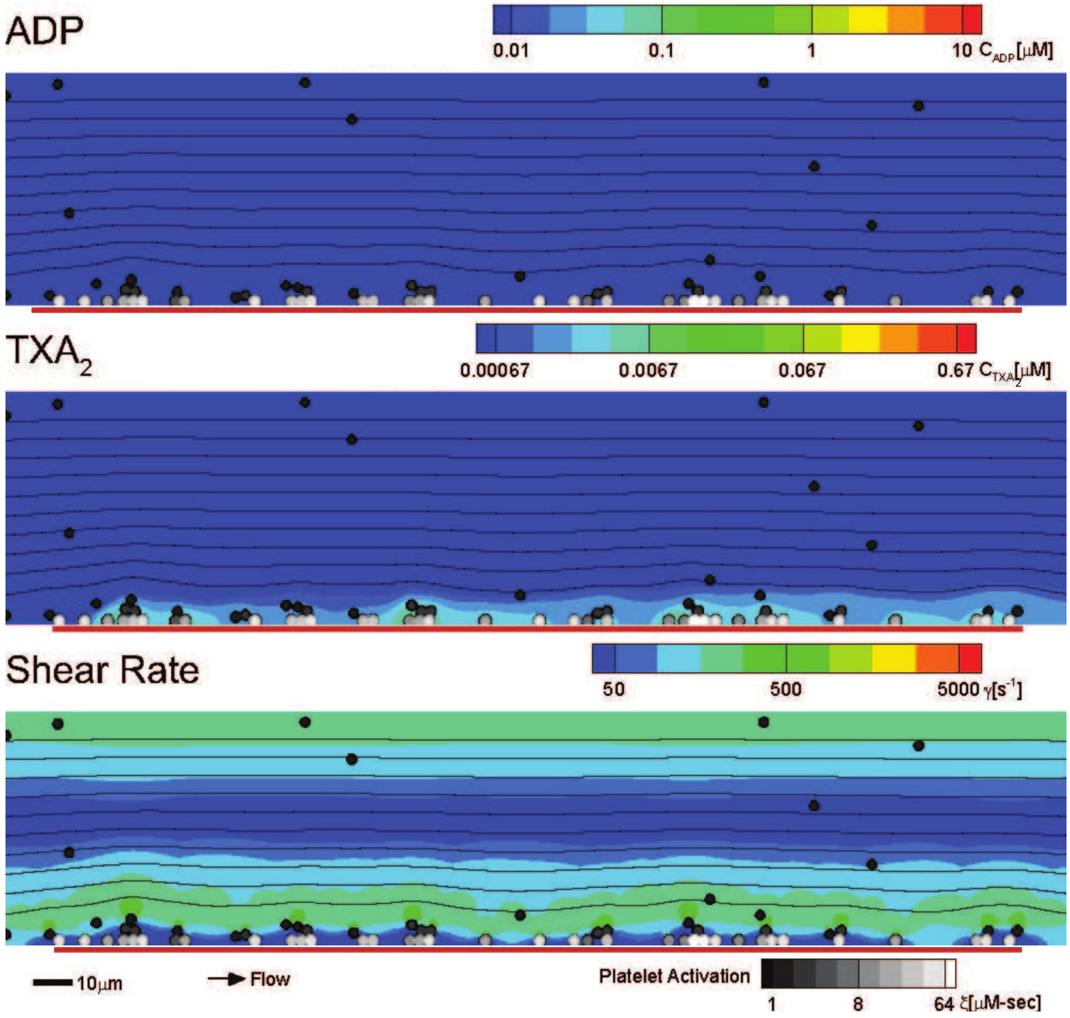

Figure B.12: Donor 3: MRS-2179 treated (500 s). Platelet activation (black, unactivated; white, activated) and deposition (inlet wall shear rate, $200\,\mathrm{s}^{-1}$) in the presence of ADP (top) and TXA_2 (middle) where local shear rate near the platelet deposit varies markedly from $< 50\,\mathrm{s}^{-1}$ to greater than $1000\,\mathrm{s}^{-1}$ (bottom). Flow: left to right (streamlines, black lines); surface collagen (250 μm long): red bar.

Bibliography

[1] Joseph A. DiMasi, Ronald W. Hansen, and Henry G. Grabowski. The price of innovation: New estimates of drug development costs. *Journal of Health Economics*, 22(2):151–185, 2003.

[2] Gitt Panitchayangkoon, Dugan Hayes, Kelly A. Fransted, Justin R. Caram, Elad Harel, Jianzhong Wen, Robert E. Blankenship, and Gregory S. Engel. Long-lived quantum coherence in photosynthetic complexes at physiological temperature. *Proceedings of the National Academy of Sciences*, 107(29):12766–12770, 2010.

[3] David E. Shaw, Ron O. Dror, John K. Salmon, J. P. Grossman, Kenneth M. Mackenzie, Joseph A. Bank, Cliff Young, Martin M. Deneroff, Brannon Batson, Kevin J. Bowers, Edmond Chow, Michael P. Eastwood, Douglas J. Ierardi, John L. Klepeis, Jeffrey S. Kuskin, Richard H. Larson, Kresten Lindorff-Larsen, Paul Maragakis, Mark A. Moraes, Stefano Piana, Yibing Shan, and Brian Towles. Millisecond-scale molecular dynamics simulations on Anton. In *Proceedings of the Conference on High Performance Computing Networking, Storage and Analysis*, pages 39:1–39:11, 2009.

[4] Douglas Young, Jaroslav Stark, and Denise Kirschner. Systems biology of persistent infection: Tuberculosis as a case study. *Nature Reviews Microbiology*, 6(7):520–528, 2008.

[5] Michael K. Gilson and Huan-Xiang Zhou. Calculation of protein-ligand binding affinities. *Annual Review of Biophysics and Biomolecular Structure*, 36(1):21–42, 2007.

[6] Vijay S. Pande and Daniel S. Rokhsar. Molecular dynamics simulations of unfolding and refolding of a beta-hairpin fragment of protein G. *Proceedings of the National Academy of Sciences*, 96(16):9062–9067, 1999.

[7] M. Hucka, A. Finney, H. M. Sauro, H. Bolouri, J. C. Doyle, H. Kitano, and the rest of the SBML Forum, A. P. Arkin, B. J. Bornstein, D. Bray, A. Cornish-Bowden, A. A. Cuellar, S. Dronov, E. D. Gilles, M. Ginkel, V. Gor, I. I. Goryanin, W. J. Hedley, T. C. Hodgman, J.-H. Hofmeyr, P. J. Hunter, N. S. Juty, J. L. Kasberger, A. Kremling, U. Kummer, N. Le Novère, L. M. Loew, D. Lucio, P. Mendes, E. Minch, E. D. Mjolsness, Y. Nakayama, M. R. Nelson, P. F. Nielsen, T. Sakurada, J. C. Schaff, B. E. Shapiro, T. S. Shimizu, H. D. Spence, J. Stelling, K. Takahashi, M. Tomita, J. Wagner, and J. Wang. The systems biology markup language (SBML): A medium for representation and exchange of biochemical network models. *Bioinformatics*, 19(4):524–531, 2003.

[8] W. J. Hedley, M. R. Nelson, D. P. Bellivant, and P. F. Nielsen. A short introduction to CellML. *Philosophical Transactions of the Royal Society of London. Series A: Mathematical, Physical and Engineering Sciences*, 359(1783):1073–1089, 2001.

[9] Hong Li, Yang Cao, Linda R. Petzold, and Daniel T. Gillespie. Algorithms and software for stochastic simulation of biochemical reacting systems. *Biotechnology Progress*, 24(1):56–61, 2008.

[10] Uwe Sauer. Metabolic networks in motion: 13C-based flux analysis. *Molecular Systems Biology*, 2:62, 2006.

[11] Birgit Schoeberl, Claudia Eichler-Jonsson, Ernst D. Gilles, and Gertraud Muller. Computational modeling of the dynamics of the MAP kinase cascade activated by surface and internalized EGF receptors. *Nature Biotechnology*, 20(4):370–375, 2002.

[12] Trey Ideker, Vesteinn Thorsson, Jeffrey A. Ranish, Rowan Christmas, Jeremy Buhler, Jimmy K. Eng, Roger Bumgarner, David R. Goodlett, Ruedi Aebersold, and Leroy Hood. Integrated genomic and proteomic analyses of a systematically perturbed metabolic network. *Science*, 292(5518):929–934, 2001.

[13] J. S. Edwards and B. O. Palsson. The Escherichia coli MG1655 in silico metabolic genotype: Its definition, characteristics, and capabilities. *Proceedings of the National Academy of Sciences*, 97(10):5528–5533, 2000.

[14] S. L. Diamond, S. G. Eskin, and L. V. McIntire. Fluid flow stimulates tissue plasminogen activator secretion by cultured human endothelial cells. *Science*, 243(4897):1483–1485, 1989.

[15] Eleni Tzima, Mohamed Irani-Tehrani, William B. Kiosses, Elizabetta Dejana, David A. Schultz, Britta Engelhardt, Gaoyuan Cao, Horace DeLisser, and Martin Alexander Schwartz. A mechanosensory complex that mediates the endothelial cell response to fluid shear stress. *Nature*, 437(7057):426–431, 2005.

[16] Dennis E. Discher, Paul Janmey, and Yu-li Wang. Tissue cells feel and respond to the stiffness of their substrate. *Science*, 310(5751):1139–1143, 2005.

[17] Tony Yeung, Penelope C. Georges, Lisa A. Flanagan, Beatrice Marg, Miguelina Ortiz, Makoto Funaki, Nastaran Zahir, Wenyu Ming, Valerie Weaver, and Paul A. Janmey. Effects of substrate stiffness on cell morphology, cytoskeletal structure, and adhesion. *Cell Motility and the Cytoskeleton*, 60(1):24–34, 2005.

[18] Janet Rubin, Tamara Murphy, Mark S. Nanes, and Xian Fan. Mechanical strain inhibits expression of osteoclast differentiation factor by murine stromal cells. *American Journal of Physiology—Cell Physiology*, 278(6):C1126–C1132, 2000.

[19] Andrew C. Liu, David K. Welsh, Caroline H. Ko, Hien G. Tran, Eric E. Zhang, Aaron A. Priest, Ethan D. Buhr, Oded Singer, Kirsten Meeker, Inder M. Verma, Francis J. Doyle III, Joseph S. Takahashi, and Steve A. Kay. Intercellular coupling confers robustness against mutations in the SCN circadian clock network. *Cell*, 129(3):605–616, 2007.

[20] Gerda de Vries and Arthur Sherman. Channel sharing in pancreatic beta-cells revisited: Enhancement of emergent bursting by noise. *Journal of Theoretical Biology*, 207(4):513–530, 2000.

[21] Jeffrey A. Hubbell and Larry V. McIntire. Platelet active concentration profiles near growing thrombi. A mathematical consideration. *Biophysical Journal*, 50(5):937–945, 1986.

[22] Jitendra S. Kanodia, Richa Rikhy, Yoosik Kim, Viktor K. Lund, Robert DeLotto, Jennifer Lippincott-Schwartz, and Stanislav Y. Shvartsman. Dynamics of the dorsal morphogen gradient. *Proceedings of the National Academy of Sciences*, 106(51):21707–21712, 2009.

[23] Matthew H. Flamm, Scott L. Diamond, and Talid Sinno. Lattice kinetic Monte Carlo simulations of convective-diffusive systems. *The Journal of Chemical Physics*, 130(9):094904, 2009.

[24] Matthew H. Flamm, Talid Sinno, and Scott L. Diamond. Simulation of aggregating particles in complex flows by the lattice kinetic Monte Carlo method. *The Journal of Chemical Physics*, 134(3):034905, 2011.

[25] Z. Zhang, C. Kleinstreuer, and C. S. Kim. Cyclic micron-size particle inhalation and deposition in a triple bifurcation lung airway model. *Journal of Aerosol Science*, 33(2):257–281, 2002.

[26] Yan Geng, Paul Dalhaimer, Shenshen Cai, Richard Tsai, Manorama Tewari, Tamara Minko, and Dennis E. Discher. Shape effects of filaments versus spherical particles in flow and drug delivery. *Nature Nanotechnology*, 2(4):249–255, 2007.

[27] C. Xiong and S. K. Friedlander. Morphological properties of atmospheric aerosol aggregates. *Proceedings of the National Academy of Sciences*, 98(21):11851–11856, 2001.

[28] I. N. McCave. Size spectra and aggregation of suspended particles in the deep ocean. *Deep Sea Research Part A. Oceanographic Research Papers*, 31(4):329–352, 1984.

[29] E. Brunet, G. Degr, F. Okkels, and P. Tabeling. Aggregation of paramagnetic particles in the presence of a hydrodynamic shear. *Journal of Colloid and Interface Science*, 282(1):58–68, 2005.

[30] A. D. Taylor, S. Neelamegham, J. D. Hellums, C. W. Smith, and S. I. Simon. Molecular dynamics of the transition from L-selectin- to beta 2-integrin-dependent neutrophil adhesion under defined hydrodynamic shear. *Biophysical Journal*, 71(6):3488–3500, 1996.

[31] David N. Bell, Samira Spain, and Harry L. Goldsmith. Adenosine diphosphate-induced aggregation of human platelets in flow through tubes. I. Measurement of concentration and size of single platelets and aggregates. *Biophysical Journal*, 56(5):817–828, 1989.

[32] S. Neelamegham, A. D. Taylor, J. D. Hellums, M. Dembo, C. W. Smith, and S. I. Simon. Modeling the reversible kinetics of neutrophil aggregation under hydrodynamic shear. *Biophysical Journal*, 72(4):1527–1540, 1997.

[33] Sergei E. Esipov. Coupled Burgers equations: A model of polydispersive sedimentation. *Physical Review E*, 52:3711–3718, 1995.

[34] P. J Hoogerbrugge and J. M. V. A Koelman. Simulating microscopic hydrodynamic phenomena with dissipative particle dynamics. *Europhysics Letters*, 19(3):155–160, 1992.

[35] A. J. C. Ladd and R. Verberg. Lattice-Boltzmann simulations of particle-fluid suspensions. *Journal of Statistical Physics*, 104(5):1191–1251, 2001.

[36] Howard H. Hu, N. A. Patankar, and M. Y. Zhu. Direct numerical simulations of fluid-solid systems using the arbitrary LagrangianEulerian technique. *Journal of Computational Physics*, 169(2):427–462, 2001.

[37] Pep Español. Hydrodynamics from dissipative particle dynamics. *Physical Review E*, 52:1734–1742, 1995.

[38] Hudong Chen, Shiyi Chen, and William H. Matthaeus. Recovery of the Navier-Stokes equations using a lattice-gas Boltzmann method. *Physical Review A*, 45(8):R5339–R5342, 1992.

[39] B. Uma, T. N. Swaminathan, R. Radhakrishnan, D. M. Eckmann, and P. S. Ayyaswamy. Nanoparticle Brownian motion and hydrodynamic interactions in the presence of flow fields. *Physics of Fluids*, 23(7):073602, 2011.

[40] J. S. Marshall. Particle aggregation and capture by walls in a particulate aerosol channel flow. *Journal of Aerosol Science*, 38(3):333–351, 2007.

[41] Joe S. Hur, Eric S. G. Shaqfeh, and Ronald G. Larson. Brownian dynamics simulations of single DNA molecules in shear flow. *Journal of Rheology*, 44(4):713–742, 2000.

[42] Zhiliang Xu, Nan Chen, Malgorzata M. Kamocka, Elliot D. Rosen, and Mark Alber. A multiscale model of thrombus development. *Journal of the Royal Society Interface*, 5(24):705–722, 2008.

[43] Sheldon K. Friedlander. *Smoke, Dust, and Haze: Fundamentals of Aerosol Dynamics*. Oxford University Press, New York, 2 edition, 2000.

[44] T. G. M. van De Van and S. G. Mason. The microrheology of colloidal dispersions VII. Orthokinetic doublet formation of spheres. *Colloid and Polymer Science*, 255(5):468–479, 1977.

[45] P. M. Adler. Heterocoagulation in shear flow. *Journal of Colloid and Interface Science*, 83(1):106–115, 1981.

[46] John Gregory. Flocculation in laminar tube flow. *Chemical Engineering Science*, 36(11):1789–1794, 1981.

[47] Robert M. Ziff, E. D. McGrady, and Paul Meakin. On the validity of Smoluchowski's equation for cluster-cluster aggregation kinetics. *The Journal of Chemical Physics*, 82(11):5269–5274, 1985.

[48] Paul Meakin, Tamás Vicsek, and Fereydoon Family. Dynamic cluster-size distribution in cluster-cluster aggregation: Effects of cluster diffusivity. *Physical Review B*, 31(1):564–569, 1985.

[49] Fereydoon Family, Paul Meakin, and Tamás Vicsek. Cluster size distribution in chemically controlled cluster–cluster aggregation. *The Journal of Chemical Physics*, 83(8):4144–4150, 1985.

[50] Martin Frossard, Ingrid Fuchs, Judith M. Leitner, Kety Hsieh, Marianne Vlcek, Heidrun Losert, Hans Domanovits, Wolfgang Schreiber, Anton N. Laggner, and Bernd Jilma.

Platelet function predicts myocardial damage in patients with acute myocardial infarction. *Circulation*, 110(11):1392–1397, 2004.

[51] Graeme J. Hankey and John W. Eikelboom. Aspirin resistance. *The Lancet*, 367(9510):606–617, 2006.

[52] Thuy Anh Nguyen, Jean G. Diodati, and Chantal Pharand. Resistance to clopidogrel: A review of the evidence. *Journal of the American College of Cardiology*, 45(8):1157–1164, 2005.

[53] Shlomi Matetzky, Boris Shenkman, Victor Guetta, Michael Shechter, Roy Bienart, Ilan Goldenberg, Ilya Novikov, Hanna Pres, Naphtali Savion, David Varon, and Hanoch Hod. Clopidogrel resistance is associated with increased risk of recurrent atherothrombotic events in patients with acute myocardial infarction. *Circulation*, 109(25):3171–3175, 2004.

[54] George Krasopoulos, Stephanie J. Brister, W. Scott Beattie, and Michael R. Buchanan. Aspirin resistance and risk of cardiovascular morbidity: Systematic review and meta-analysis. *BMJ*, 336(7637):195–198, 2008.

[55] Y. Ikeda, M. Handa, K. Kawano, T. Kamata, M. Murata, Y. Araki, H. Anbo, Y. Kawai, K. Watanabe, and I. Itagaki. The role of von Willebrand factor and fibrinogen in platelet aggregation under varying shear stress. *The Journal of Clinical Investigation*, 87(4):1234–1240, 1991.

[56] Pål A. Holme, Una Ørvim, Maria J. A. G. Hamers, Nils O. Solum, Frank R. Brosstad, R. Marius Barstad, and Kjell S. Sakariassen. Shear-induced platelet activation and platelet microparticle formation at blood flow conditions as in arteries with a severe stenosis. *Arteriosclerosis, Thrombosis, and Vascular Biology*, 17(4):646–653, 1997.

[57] Loic Boussel, Vitaliy Rayz, Alastair Martin, Gabriel Acevedo-Bolton, Michael T. Lawton, Randall Higashida, Wade S. Smith, William L. Young, and David Saloner. Phase-contrast magnetic resonance imaging measurements in intracranial aneurysms in vivo of flow patterns, velocity fields, and wall shear stress: Comparison with computational fluid dynamics. *Magnetic Resonance in Medicine*, 61(2):409–417, 2009.

[58] Jeffrey A. Hubbell and Larry V. McIntire. Visualization and analysis of mural thrombogenesis on collagen, polyurethane and nylon. *Biomaterials*, 7(5):354–363, 1986.

[59] B. R. Alevriadou, J. L. Moake, N. A. Turner, Z. M. Ruggeri, B. J. Folie, M. D. Phillips, A. B. Schreiber, M. E. Hrinda, and L. V. McIntire. Real-time analysis of shear-dependent thrombus formation and its blockade by inhibitors of von Willebrand factor binding to platelets. *Blood*, 81(5):1263–1276, 1993.

[60] Keith B. Neeves and Scott L. Diamond. A membrane-based microfluidic device for controlling the flux of platelet agonists into flowing blood. *Lab on a Chip*, 8(5):701–709, 2008.

[61] K. B. Neeves, S. F. Maloney, K. P. Fong, A. A. Schmaier, M. L. Kahn, L. F. Brass, and Scott L. Diamond. Microfluidic focal thrombosis model for measuring murine platelet deposition and stability: PAR4 signaling enhances shear-resistance of platelet aggregates. *Journal of Thrombosis and Haemostasis*, 6(12):2193–201, 2008.

[62] T. Colace, E. Falls, X. Zheng, and S. Diamond. Analysis of morphology of platelet aggregates formed on collagen under laminar blood flow. *Annals of Biomedical Engineering*, 39:922–929, 2011.

[63] S. F. Maloney, Lawrence F. Brass, and S. L. Diamond. P2Y12 or P2Y1 inhibitors reduce platelet deposition in a microfluidic model of thrombosis while apyrase lacks efficacy under flow conditions. *Integrative Biology*, 2:183–192, 2010.

[64] Thomas V. Colace, Jannielle Jobson, and Scott L. Diamond. Relipidated tissue factor linked to collagen surfaces potentiates platelet adhesion and fibrin formation in a microfluidic model of vessel injury. *Bioconjugate Chemistry*, 2011.

[65] Jeremy E. Purvis, Manash S. Chatterjee, Lawrence F. Brass, and Scott L. Diamond. A molecular signaling model of platelet phosphoinositide and calcium regulation during homeostasis and P2Y1 activation. *Blood*, 112(10):4069–4079, 2008.

[66] Jeremy E. Purvis, Ravi Radhakrishnan, and Scott L. Diamond. Steady-state kinetic modeling constrains cellular resting states and dynamic behavior. *PLoS Computational Biology*, 5(3):e1000298, 03 2009.

[67] Manash S. Chatterjee, Jeremy E. Purvis, Lawrence F. Brass, and Scott L. Diamond. Pairwise agonist scanning predicts cellular signaling responses to combinatorial stimuli. *Nature Biotechnology*, 28(7):727–732, 2010.

[68] Matthew F. Hockin, Kenneth C. Jones, Stephen J. Everse, and Kenneth G. Mann. A model for the stoichiometric regulation of blood coagulation. *The Journal of Biological Chemistry*, 277(21):18322–18333, 2002.

[69] Ken Lo, William S. Denney, and Scott L. Diamond. Stochastic modeling of blood coagulation initiation. *Pathophysiology of Haemostasis and Thrombosis*, 34(2-3):80–90, 2005.

[70] Andrew L. Kuharsky and Aaron L. Fogelson. Surface-mediated control of blood coagulation: The role of binding site densities and platelet deposition. *Biophysical Journal*, 80(3):1050–1074, 2001.

[71] Manash S. Chatterjee, William S. Denney, Huiyan Jing, and Scott L. Diamond. Systems biology of coagulation initiation: Kinetics of thrombin generation in resting and activated human blood. *PLoS Computational Biology*, 6(9):e1000950, 2010.

[72] Bernard J. Folie and Larry V. McIntire. Mathematical analysis of mural thrombogenesis. Concentration profiles of platelet-activating agents and effects of viscous shear flow. *Biophysical Journal*, 56(6):1121–1141, 1989.

[73] Erik N. Sorensen, Greg W. Burgreen, William R. Wagner, and James F. Antaki. Computational simulation of platelet deposition and activation: I. Model development and properties. *Annals of Biomedical Engineering*, 27(4):436–448, 1999.

[74] Erik N. Sorensen, Greg W. Burgreen, William R. Wagner, and James F. Antaki. Computational simulation of platelet deposition and activation: II. Results for poiseuille flow over collagen. *Annals of Biomedical Engineering*, 27(4):449–458, 1999.

[75] Nipa A. Mody and Michael R. King. Platelet adhesive dynamics. Part I: Characterization of platelet hydrodynamic collisions and wall effects. *Biophysical Journal*, 95(5):2539–2555, 2008.

[76] Nipa A. Mody and Michael R. King. Platelet adhesive dynamics. Part II: High shear-induced transient aggregation via GPIbalpha-vWF-GPIbalpha bridging. *Biophysical Journal*, 95(5):2556–2574, 2008.

[77] Igor V. Pivkin, Peter D. Richardson, and George Karniadakis. Blood flow velocity effects and role of activation delay time on growth and form of platelet thrombi. *Proceedings of the National Academy of Sciences*, 103(46):17164–17169, 2006.

[78] Prosenjit Bagchi. Mesoscale simulation of blood flow in small vessels. *Biophysical Journal*, 92(6):1858–1877, 2007.

[79] Lindsay M. Crowl and Aaron L. Fogelson. Computational model of whole blood exhibiting lateral platelet motion induced by red blood cells. *International Journal for Numerical Methods in Biomedical Engineering*, 26(3-4):471–487, 2010.

[80] Hong Zhao and Eric S. G. Shaqfeh. Shear-induced platelet margination in a microchannel. *Physical Review E*, 83:061924, 2011.

[81] E. W. Merrill and G. A. Pelletier. Viscosity of human blood: Transition from Newtonian to non-Newtonian. *Journal of Applied Physiology*, 23(2):178–182, 1967.

[82] K. Perktold, M. Resch, and H. Florian. Pulsatile non-Newtonian flow characteristics in a three-dimensional human carotid bifurcation model. *Journal of Biomechanical Engineering*, 113(4):464–475, 1991.

[83] Charles Taylor and David Steinman. Image-based modeling of blood flow and vessel wall dynamics: Applications, methods and future directions. *Annals of Biomedical Engineering*, 38:1188–1203, 2010.

[84] Karin Leiderman and Aaron L. Fogelson. Grow with the flow: A spatialtemporal model of platelet deposition and blood coagulation under flow. *Mathematical Medicine and Biology*, 28(1):47–84, 2011.

[85] Zhiliang Xu, Joshua Lioi, Jian Mu, Malgorzata M. Kamocka, Xiaomin Liu, Danny Z. Chen, Elliot D. Rosen, and Mark Alber. A multiscale model of venous thrombus formation with surface-mediated control of blood coagulation cascade. *Biophysical Journal*, 98(9):1723–1732, 2010.

[86] Arthur F. Voter. Classically exact overlayer dynamics: Diffusion of rhodium clusters on Rh(100). *Physical Review B*, 34(10):6819–6829, 1986.

[87] Graeme Henkelman and Hannes Jónsson. Long time scale kinetic Monte Carlo simulations without lattice approximation and predefined event table. *The Journal of Chemical Physics*, 115(21):9657–9666, 2001.

[88] Daniel T. Gillespie. A general method for numerically simulating the stochastic time evolution of coupled chemical reactions. *Journal of Computational Physics*, 22(4):403–434, 1976.

[89] Michael A. Gibson and Jehoshua Bruck. Efficient exact stochastic simulation of chemical systems with many species and many channels. *Journal of Physical Chemistry A*, 104(9):1876–1889, 2000.

[90] P. A. Maksym. Fast Monte Carlo simulation of MBE growth. *Semiconductor Science and Technology*, 3(6):594, 1988.

[91] James L. Blue, Isabel Beichl, and Francis Sullivan. Faster Monte Carlo simulations. *Physical Review E*, 51(2):R867–R868, 1995.

[92] Tim P. Schulze. Efficient kinetic Monte Carlo simulation. *Journal of Computational Physics*, 227(4):2455–2462, 2008.

[93] A. Bortz, M. Kalos, and J. Lebowitz. A new algorithm for Monte Carlo simulation of Ising spin systems. *Journal of Computational Physics*, 17(1):10–18, 1975.

[94] William Pugh. Skip lists: A probabilistic alternative to balanced trees. *Communications of the ACM*, 33(6):668–676, 1990.

[95] Daniel T. Gillespie. Approximate accelerated stochastic simulation of chemically reacting systems. *The Journal of Chemical Physics*, 115(4):1716–1733, 2001.

[96] Daniel T. Gillespie and Linda R. Petzold. Improved leap-size selection for accelerated stochastic simulation. *The Journal of Chemical Physics*, 119(16):8229, 2003.

[97] Jianguo Dai, Warren D. Seider, and Talid Sinno. Coarse-grained lattice kinetic Monte Carlo simulation of systems of strongly interacting particles. *The Journal of Chemical Physics*, 128(19):194705, 2008.

[98] Gianni Comini, Stefano del Giudice, and Carlo Nonino. *Finite Element Analysis in Heat Transfer*. Taylor and Francis, 1994.

[99] J. N. Reddy and D. K. Gartling. *The Finite Element Method in Heat Transfer and Fluid Dynamics*. CRC Press, 2001.

[100] Shuling Hou, Qisu Zou, Shiyi Chen, Gary Doolen, and Allen C. Cogley. Simulation of cavity flow by the lattice Boltzmann method. *Journal of Computational Physics*, 118(2):329–347, 1995.

[101] Y. H. Qian, Pierre Lallemand, and D. D'Humières. Lattice BGK models for Navier-Stokes equation. *Europhysics Letters*, 17(6):479–484, 1992.

[102] Qisu Zou and Xiaoyi He. On pressure and velocity boundary conditions for the lattice Boltzmann BGK model. *Physics of Fluids*, 9(6):1591–1598, 1997.

[103] Adam Arkin, John Ross, and Harley H. McAdams. Stochastic kinetic analysis of developmental pathway bifurcation in phage lambda-infected Escherichia coli cells. *Genetics*, 149(4):1633–48, 1998.

[104] Ian J. Laurenzi and Scott L. Diamond. Monte Carlo simulation of the heterotypic aggregation kinetics of platelets and neutrophils. *Biophysical Journal*, 77:1733–1746, 1999.

[105] Ian J. Laurenzi and Scott L. Diamond. Kinetics of random aggregation-fragmentation processes with multiple components. *Physical Review E*, 67:051103, 2003.

[106] Jianguo Dai, Joshua M. Kanter, Sumeet S. Kapur, Warren D. Seider, and Talid Sinno. On-lattice kinetic Monte Carlo simulations of point defect aggregation in entropically influenced crystalline systems. *Physical Review B*, 72(13):134102, 2005.

[107] Andrea C. Levi and Miroslav Kotrla. Theory and simulation of crystal growth. *Journal of Physics: Condensed Matter*, 9(2):299–344, 1997.

[108] Daniel T. Gillespie. Exact stochastic simulation of coupled chemical reactions. *Journal of Physical Chemistry*, 81(25):2340–2361, 1977.

[109] Michel G. Gauthier and Gary W. Slater. Building reliable lattice Monte Carlo models for real drift and diffusion problems. *Physical Review E*, 70(1):015103R, 2004.

[110] Michel G. Gauthier and Gary W. Slater. A new set of Monte Carlo moves for lattice random-walk models of biased diffusion. *Physica A: Statistical Mechanics and its Applications*, 355(2-4):283–296, 2005.

[111] R. Aris. On the dispersion of a solute in a fluid flowing through a tube. *Proceedings of the Royal Society of London Series A—Mathematical and Physical Sciences*, 235(1200):67–77, 1956.

[112] Babak Sadigh, Thomas J. Lenosky, Silva K. Theiss, Maria-Jose Caturla, Tomas Diaz de la Rubia, and Majeed A. Foad. Mechanism of boron diffusion in silicon: An *ab initio* and kinetic Monte Carlo study. *Physical Review Letters*, 83:4341–4344, 1999.

[113] R. J. Gelten, A. P. J. Jansen, R. A. van Santen, J. J. Lukkien, J. P. L. Segers, and P. A. J. Hilbers. Monte Carlo simulations of a surface reaction model showing spatio-temporal pattern formations and oscillations. *The Journal of Chemical Physics*, 108(14):5921–5934, 1998.

[114] M. Tringides and R. Gomer. A Monte Carlo study of oxygen diffusion on the (110) plane of tungsten. *Surface Science*, 145(1):121–144, 1984.

[115] J. M. Burgers. *The Nonlinear Diffusion Equation: Asymptotic Solutions and Statistical Problems*. D. Reidel, 1973.

[116] Debashish Chowdhury, Ludger Santen, and Andreas Schadschneider. Statistical physics of vehicular traffic and some related systems. *Physics Reports*, 329(4-6):199–329, 2000.

[117] Mehran Kardar, Giorgio Parisi, and Yi-Cheng Zhang. Dynamic scaling of growing interfaces. *Physical Review Letters*, 56(9):889–892, 1986.

[118] Dietrich Stauffer and Ammon Aharony. *Introduction To Percolation Theory.* CRC, 1994.

[119] S. M. Ross. *A First Course in Probability.* Pearson Prentice Hall, 2006.

[120] N. G. van Kampen. *Stochastic Processes in Physics and Chemistry.* North Holland, 1992.

[121] Pushkar Tandon and Scott L. Diamond. Hydrodynamic effects and receptor interactions of platelets and their aggregates in linear shear flow. *Biophysical Journal*, 73(5):2819–2835, 1997.

[122] Pushkar Tandon and Scott L. Diamond. Kinetics of beta2-integrin and L-selectin bonding during neutrophil aggregation in shear flow. *Biophysical Journal*, 75(6):3163–3178, 1998.

[123] D. Ramkrishna and Sanjeev Kumar. On the solution of population balance equations by discretization I. A fixed pivot technique. *Chemical Engineering Science*, 51(8):1311–1332, 1996.

[124] Matthew Smith and Themis Matsoukas. Constant-number Monte Carlo simulation of population balances. *Chemical Engineering Science*, 53(9):1777–1786, 1998.

[125] Rustem I. Litvinov, Henry Shuman, Joel S. Bennett, and John W. Weisel. Binding strength and activation state of single fibrinogen-integrin pairs on living cells. *Proceedings of the National Academy of Sciences*, 99(11):7426–7431, 2002.

[126] J. M. Paulus. Platelet size in man. *Blood*, 46(3):321–336, 1975.

[127] Vincent T. Turitto, Anthony M. Benis, and Edward F. Leonard. Platelet diffusion in flowing blood. *Industrial & Engineering Chemistry Fundamentals*, 11(2):216–223, 1972.

[128] C. Yeh, A. C. Calvez, and Eugene C. Eckstein. An estimated shape function for drift in a platelet-transport model. *Biophysical Journal*, 67(3):1252–1259, 1994.

[129] W. Siess. Molecular mechanisms of platelet activation. *Physiological Reviews*, 69(1):58–178, 1989.

[130] B. Nieswandt, D. Varga-Szabo, and M. Elvers. Integrins in platelet activation. *Journal of Thrombosis and Haemostasis*, 7:206–209, 2009.

[131] George I. Bell. Models for the specific adhesion of cells to cells. *Science*, 200(4342):618–627, 1978.

[132] Edgar E. Nanne, Christian P. Aucoin, and Edward F. Leonard. Shear rate and hematocrit effects on the apparent diffusivity of urea in suspensions of bovine erythrocytes. *American Society for Artificial Internal Organs Journal*, 56(3):151–156, 2010.

[133] Holm Holmsen, Eva Storm, and H. James Day. Determination of ATP and ADP in blood platelets: A modification of the firefly luciferase assay for plasma. *Analytical Biochemistry*, 46(2):489–501, 1972.

[134] Reza Beigi, Eiry Kobatake, Masuo Aizawa, and George R. Dubyak. Detection of local ATP release from activated platelets using cell surface-attached firefly luciferase. *American Journal of Physiology—Cell Physiology*, 276(1):C267–C278, 1999.

[135] R. de Caterina, D. Giannessi, P. Gazzetti, and W. Bernini. Thromboxane-B2 generation during ex-vivo platelet aggregation. *Journal of Nuclear Medicine and Allied Sciences*, 28(3):185–196, 1984.

[136] C. Giles. The platelet count and mean platelet volume. *British Journal of Haematology*, 48(1):31–37, 1981.

[137] Raymond J. Trudnowski and Rodolfo C. Rico. Specific gravity of blood and plasma at 4 and 37 C. *Clinical Chemistry*, 20(5):615–616, 1974.

[138] Roe E. Wells and Edward W. Merrill. Influence of flow properties of blood upon viscosity-hematocrit relationships. *The Journal of Clinical Investigation*, 41(8):1591–1598, 1962.

[139] Sasidhar Guthikonda, Carlos L. Alviar, Muthiah Vaduganathan, Mehmet Arikan, Armando Tellez, Timothy DeLao, Juan F. Granada, Jing-Fei Dong, Neal S. Kleiman, and Eli I. Lev. Role of reticulated platelets and platelet size heterogeneity on platelet activity after dual antiplatelet therapy with aspirin and clopidogrel in patients with stable coronary artery disease. *Journal of the American College of Cardiology*, 52(9):743–749, 2008.

[140] Johan W. M. Heemskerk, Wim M. J. Vuist, Marion A. H. Feijge, Chris P. M. Reutelingsperger, and Theo Lindhout. Collagen but not fibrinogen surfaces induce bleb formation, exposure of phosphatidylserine, and procoagulant activity of adherent platelets: Evidence for regulation by protein tyrosine kinase-dependent Ca2+ responses. *Blood*, 90(7):2615–2625, 1997.

[141] Cristian Picioreanu, Mark C. M. van Loosdrecht, and Joseph J. Heijnen. Two-dimensional model of biofilm detachment caused by internal stress from liquid flow. *Biotechnology and Bioengineering*, 72(2):205–218, 2001.

[142] Nicos S. Martys. Improved approximation of the Brinkman equation using a lattice Boltzmann method. *Physics of Fluids*, 13(6):1807–1810, 2001.